UNIVERSITY OF SOUTHAMPTON

FACULTY OF ENGINEERING AND THE ENVIRONMENT

Fluid Structure Interaction Group

The development of a dissipative potential flow model for wave making resistance prediction

by

Mirjam Fürth

Thesis for the degree of Doctor of Philosophy

June 2014

UNIVERSITY OF SOUTHAMPTON

ABSTRACT

FACULTY OF ENGINEERING AND THE EVIRONMENT

Fluid Structure Interaction Group

Doctor of Philosophy

THE DEVLOPMENT OF A DISSIPATIVE POTENTIAL FLOW MODEL FOR WAVE MAKING RESITANCE PREDICTION

by Mirjam Fürth

Steady ship motion in calm water is a classical problem in ship hydrodynamics. Potential flow modelling is a common method to predict the wave resistance of ships. In its conventional form the flow is assumed to be free from damping due to the inviscid assumption of potential flow. It has been argued by the founding fathers of ship resistance predictions that damping plays an important role in determining the wave resistance. Despite this viscosity is often omitted from present wave resistance prediction methods. It is known that damping plays an important role in the formation of the wave pattern and it is therefore of interest to determine the effect on the resistance prediction by including a damping factor in a previously undampened model.

In this study, the problem is modelled using Kelvin sources with a translating speed. The fluid flow is modelled using a linearised free surface condition but an exact body condition on the hull. Rayleigh damping is introduced in the model to emulate viscous damping. To calculate the source influences, a new dissipative 3D Green function is derived. The image source part of Green function is separated into the near field and far field disturbance to achieve fast convergence of the integrals.

The method is evaluated using thin ship theory to determine the wave pattern behind and the wave profile along a Wigley hull. A panel method is used to determine the wave and residual resistance for submerged ellipsoids and spheres. The results are validated and compared to existing numerical and experimental data from other sources. The results show that it may be possible to capture the residual resistance by including damping in a potential flow model but that more evaluations are needed.

Table of Contents

List of tables

List of figures

DECLARATION OF AUTHORSHIP

I, Mirjam Fürth declare that this thesis and the work presented in it are my own and has been generated by me as the result of my own original research.

The development of a dissipative potential flow model for wave making resistance prediction

I confirm that:

1. This work was done wholly or mainly while in candidature for a research degree at this University;
2. Where any part of this thesis has previously been submitted for a degree or any other qualification at this University or any other institution, this has been clearly stated;
3. Where I have consulted the published work of others, this is always clearly attributed;
4. Where I have quoted from the work of others, the source is always given. With the exception of such quotations, this thesis is entirely my own work;
5. I have acknowledged all main sources of help;
6. Where the thesis is based on work done by myself jointly with others, I have made clear exactly what was done by others and what I have contributed myself;
7. Parts of this work have been published as:
   Fürth, M., Tan, M. & Chen, Z.-M. (2013) Determining Wave Resistance Using a Dissipative Potential Flow Model. *Proceedings of The 23rd International Ocean and Polar Engineering*. Anchorage, United States of America: International Society of Offshore and Polar Engineers

Signed:...

Date

Acknowledgements

This project is sponsored by Lloyds Register Foundation, their support is greatly appreciated.

The continuous support of my supervisors Dr Mingyi Tan and Dr Zhi-Min Chen throughout the study is gratefully acknowledged. Suggestions by the examiner Prof Grant E Hearn also helped to improve the thesis.

I also want to thank my colleagues, friends and family for their help assisting me in climbing this mountain.

Southampton, 17/06/2014

Mirjam Fürth

Nomenclature

A_c	Upstream end of the control volume
$\boldsymbol{a}$	Source point vector
a	Location of source in x-direction, Cartesian spatial coordinate
a_e	Major axis ellipsoid
B	Beam ship
B_c	Downstream end of the control volume
b	Location of source in y-direction, Cartesian spatial coordinate
b_c	Width of the channel
b_e	Minor axis ellipsoid
C^m	Value of the continued fraction
C_e	Potential influence constant
C_i	Inner potential influence constant
C_F	Friction resistance coefficient
C_R	Residual resistance coefficient
C_t	Total resistance coefficient
C_w	Wave resistance coefficient
C_1	Ordinary Differential Equation constant
C_2	Ordinary Differential Equation constant
c	Location of source in z-direction, Cartesian spatial coordinate
c_e	Focal length ellipsoid
c_h	Intersection curve between h and $z = 0$
c_∞	Intersection curve between h_∞ and $z = 0$
D	Draught of ship
D_I	Green function double integral
D_1	Exponential part of the real part of the numerator in the double integral
D_2	Oscillatory part of the real part of the numerator in the double integral
D_s	Diameter of sphere
d_c	Depth channel
d_e	Submersion depth of ellipsoid
d_i	Domain inside the hull
d_s	Submersion depth of sphere
E_1	Exponential integral
F	Surface function
F_A	Pressure force on upstream end of control volume
F_B	Pressure force on downstream end of control volume
F_p	Pressure force

Fn	Froude number
G	Green function
g^*	Gravitational acceleration $g^* = 9.81\ m/s^2$
H	Image source part of Green function
$\widehat{H}$	Fourier transform of H
H_s	Heaviside step function
h	Hull surface
Δh_j	Panel area panel j
h_∞	Exterior surface fluid domain
I	Inner integral of the double integral
I'	Modified inner integral of the double integral
I_{ij}	Influence matrix
$\boldsymbol{i}$	Unit vector (1,0,0)
J_{ij}	Influence matrix
k	Form factor
L^*	Ship length
L_{ref}	Characteristic reference length for C_w
ℓ	Direction of tangent to the hull
m	Summation variable continued fraction
N	Near field disturbance
N_I	Near field disturbance with $\mu_R = 0$ and large T
$\boldsymbol{n}$	Unit normal vector outwards from the body
n	$n = 1$ in continued fraction for evaluation of the exponential integral E_1
n_a	a component of normal $\boldsymbol{n}$
n_b	b component of normal $\boldsymbol{n}$
n_c	c component of normal $\boldsymbol{n}$
n_T	Number of sections of the single integrals to be evaluated separately
n_x	x component of normal $\boldsymbol{n}$
n_y	y component of normal $\boldsymbol{n}$
n_z	z component of normal $\boldsymbol{n}$
n_θ	Number of sections of the outer integral
n_ρ	Number of sections of the inner integral
$\boldsymbol{n}x\boldsymbol{t}$	Unit vector pointing downwards from the hull surface
p	Pressure
p_0	Atmospheric reference pressure
Q	Source strength
$\boldsymbol{q}$	Flow speed vector

R_c	Resistance force from ship onto the control volume
R_F^*	Friction resistance
R_s	Radius of sphere
R_t^*	Total resistance
R_v^*	Viscous resistance
R_{vp}^*	Viscous pressure resistance
R_w^*	Wave resistance
r	Distance between source point and field point
r'	Distance between image source point and field point
S	Doublet strength
S^*	Wetted surface
s	Fluid domain outer surface $s = h + s' + h_\infty$
s'	Finite mean surface
s_i	Surface inside the hull
T	Substitution variable
T_{max}	Finite limit that replaces the infinite limit in the single integrals
t	Non-dimensional time
$\boldsymbol{t}$	Tangent to hull surface
t_a	a component of tangent $\boldsymbol{t}$
t_b	b component of tangent $\boldsymbol{t}$
U^*	Uniform flow speed
u	Flow speed x direction
v	Flow speed y direction
W	Far field/ wave like disturbance
W_I	Far field integrand with $\mu_R = 0$
W_1	Exponential part of W_I
W_2	Oscillatory part of W_I
w	Flow speed z direction
$\boldsymbol{X}$	Distance between field point and image source
$\boldsymbol{x}$	Field point vector
x	Field point, Cartesian spatial coordinate
x_i	Control/Collocation point
$\boldsymbol{x}'$	Normalised distance vector between image source and field point
x'	Normalised distance between image source and field point in x-direction
x_s	The hull shape in the x direction
x_0	The forward edge of each panel (thin-ship)
x_1	The aft edge of each panel (thin-ship)

y	Field point, Cartesian spatial coordinate
y'	Normalised distance between image source and field point in y-direction
y_s	The hull shape in the y direction
z	Field point, Cartesian spatial coordinate
z'	Normalised distance between image source and field point in z-direction
z_s	The hull shape in the z direction
z_0	The panel edge closest to the surface (thin ship)
z_1	The deepest panel edge (thin ship)

α_1	Angle to pole in the complex ρ plane
α_2	Angle to radial line in the complex ρ plane
δ	Dirac function
ε	Radius of sphere around singularity
ζ	Free surface elevation
η	Coordinate in transformed plane
θ	Polar coordinate angle
Λ	Substitution variable
κ_0	Wave number used by Havelock
λ^*	Transverse wave length
μ	Lamb/Havelock dissipation factor
μ_R	Normalised Rayleigh damping parameter $\mu_R = \mu_R' Fn^2$
μ_R'	Non-dimensionalised Rayleigh damping parameter
μ_R^*	Dimensional Rayleigh damping parameter
ν	Polar coordinate, radius transformed plane
ν^*	Kinematic viscosity
ξ	Coordinate in transformed plane
ρ^*	Density
ρ	Polar coordinate normalised radius $\rho = \nu Fn^2$
ρ_i	Imaginary part of ρ
ρ_{max}	Finite limit that replaces the infinite limit in the double integral
ρ_r	Real part of ρ
Σ	Integration surface
σ	Location along the radial line
τ	Integration variable
Φ	Total velocity potential
ϕ	Perturbed velocity potential
ϕ^i	Inner perturbed velocity potential

ϕ_d	Derivative of ϕ in $\boldsymbol{n}x\boldsymbol{t}$ direction
ϕ_ℓ	Derivative of ϕ in $\boldsymbol{t}$ direction
ϕ_n	Derivative of ϕ in $\boldsymbol{n}$ direction
χ	Argument of standard function E_1
$\bar{\chi}$	Complex conjugate of χ
ψ	Polar coordinate angle $\psi = \theta - \pi$
Ω	Fluid domain
*	Indicates dimensional variable
$\frown$	Indicates Fourier transform
∇	Differential operator

1 Introduction

The oldest found boats date back 10 000 years and the history of boats parallel the human adventure (Breunig, 1996) . From the early canoes dug out of tree trunks, humans have tried to improve their sea going structures. Early on this was only based on practical experience or trial and error. With the age of enlightenment and the improvement of scientific methods, experiments started to be used in order to improve ship operation. Even the multitalented Leonardo da Vinci tried to determine ship resistance by model tests (Tursini, 1953). Later on experimental methods were supplemented by theoretical methods.

With globalisation and the associated rising demand on transportation, the volume and size of the merchant fleet will also increase since the majority of goods are transported by sea. Over time, the world's GDP will rise. A GDP rise of 3% will result in a 6% rise in world trade causing a 3% rise in demand for sea transportation and an associated 2% increase in the size of the merchant fleet (Nilsson, 2010).

Such increases in shipping lead to a significant fossil fuel cost both to the ship owners and the environment. A tenth of the global oil consumption is used to power the merchant fleet (Nilsson, 2010). CO_2 emissions from shipping might rise as much as 75% in the next 15 years and currently accounts for 4% of the total global CO_2 emissions (Vidal, 2007). With the rising price of oil and the growing environmental concern, the motivation to reduce oil consumption has never been higher.

1.1 Ship resistance

A ship travelling in the seaway will experience forces trying to keep it from moving; these forces are known as the resistance. It is preferable to keep the resistance at a minimum because a ship's resistance is linked to the power required to propel the ship. The ship designer has to ensure that the ship achieves the desired speed with the minimum amount of power.

The experimental and theoretical investigation of the steady motion of a ship is complicated. Consequently, much effort has gone into developing and improving methods for determining a ship's resistance over the past 100 years. The complexity of determining a ship's resistance stems from the interaction between the water and the air; the free surface. In reality, all parts of the resistance are interconnected but to simplify resistance determination theoretically it can be separated into different components. The resistance depends on viscosity and the gravitational field so that the total resistance,R_t^*, is the sum of the viscous resistance, R_v^*, and the wave resistance, R_w^*. R_v^*, is associated with the generation of boundary layer and wake. R_w^* is connected with the excitation of ship generated wave pattern. The viscous resistance can be divided into the friction resistance, R_F^*, and the viscous pressure resistance, R_{VP}^*, where the friction resistance is the force in tangential direction on the hull and the viscous pressure resistance is associated with the pressure losses due to separation in the wake. The friction resistance depends on the roughness and size of the hull surface. Other types of resistance include aerodynamic drag on the hull and superstructure, spray drag or induced resistance related to the generation of lift. For the current investigation in still water, these are assumed to be negligible. The resistance forces are usually described by a non-dimensionalised coefficient where the force/resistance could be non-dimensionalised as:

$$C_t = \frac{R_t^*}{1/2\rho^* S^* U^{*2}}, \tag{1.1}$$

where U^* is the ship speed, S^* is the ship's wetted surface area and ρ^* the density of water. The non-dimensionalised viscous resistance coefficient, C_v, wave resistance coefficient, C_w, and friction resistance coefficient, C_F, are determined in the same manner.

From dimension analysis it is clear that the resistance depends on the speed, length, the fluid density and viscosity, gravity and some shape parameter (Molland et al, 2011). To describe this dependence the Froude and Reynolds number are often used. The Froude number is the relationship between the ship speed and the speed of the wave pattern. The Reynolds number is the relationship between the inertial and viscous forces in the fluid. The Froude and Reynolds numbers are used to help relate similar flow patterns in different fluid situations. The Froude number, Fn, is defined as

$$Fn = \frac{U^*}{\sqrt{g^* L^*}}, \tag{1.2}$$

and the Reynolds number

$$Rn = \frac{U^* L^*}{\nu^*}, \tag{1.3}$$

where L^* is the ship length, g^* the gravitational acceleration and ν^* the kinematic viscosity of water.

For merchant ships the viscous resistance is the largest component, it is approximately quadratic with ship's speed and increases with the fullness and wetted surface area of the hull. The wave resistance accounts for 10%-60% of the total resistance (Raven, 1996). The wave resistance is more amendable through changes in the hull shape (Eggers et al, 1967). A reduction in the resistance would bring considerable reductions both in operating costs and emissions. Since the viscous resistance cannot be reduced significantly by changes in the hull form optimal ship forms will be those that generate the smallest waves, it is therefore highly desirable to develop a theoretical tool to analyse the relationship between wave resistance and the geometry of the hull (Baar, 1986).

For most ships there will be a main resistance hump when the transverse wave length defined as

$$\lambda^* = \frac{2\pi U^{*2}}{g^* L} \tag{1.4}$$

is roughly equal to half the ship length. Since the bow wave and stern wave will add together to create a higher wave pattern leading to higher resistance. At low speed the viscous resistance is the major component of the total resistance and at very low speed the wave resistance is very small. Then the wave resistance increases with increased speed to become a big component of the total resistance at high speed for displacement ships (Larsson & Eliasson, 2000). There are some high speed craft such as hovercraft and planning vessels, that operates at Fn>1.3. In this case wave resistance is of lower importance. (Tuck et al, 2002).

1.2 Ship design process

All properties of a ship are intertwined, for example an increase in beam will cause an increase in resistance and therefore require an engine with the ability to deliver more power. Hence it is not possible to decide one property of the ship without analysing how it will affect other aspects of the design. A common way of clarifying the design process is through the design spiral; as illustrated in Figure 1 .

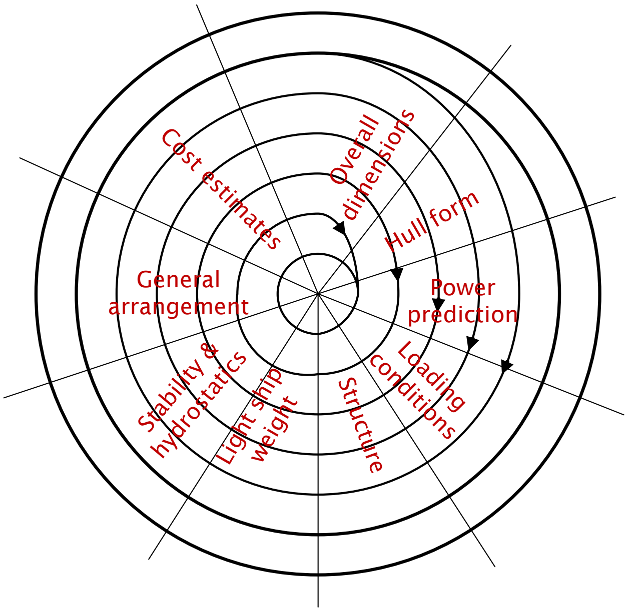

Figure 1 Design spiral used in ship design phase

There are differences in the design process between different shipyards, and it must be said that most shipyards tend to base their design on experience. This means that most designs are modifications of older models. A large part of all new builds are standardised models, especially among bulk carries and tankers (Nilsson, 2010).

Determining the resistance is not an exact science and none of the now available methods of resistance determination are without error. There are currently two main approaches to still water resistance determination; experiments and numerical modelling.

Tank testing is time consuming and expensive. It is often used at the end of the design process to confirm the estimated resistance. It could also be used to make minor changes to the underwater body such as modifying the appendices. On rare occasions tank testing or full scale tests can be used to optimise the hull shape but this mainly applies to competitive sail racing yachts such as in the America’s cup (Letcher et al, 1987).

Numerical simulations are an alternative to tank testing and there are currently several different commercial codes that solves three dimensional non-linear wave resistance problems (Bertram, 2000). However, these methods are highly complex and require long computational time which drives up the cost. Some of them may need a super computer which restricts their use as a practical design tool (Diken et al, 2004). A benefit of numerical modelling compared to experiments, besides the cost, is that it allows for thorough investigations into the impact of very specific changes of the hull geometry. An example of how a hull form can be optimised for different Froude numbers is given by Percival et al. (2001).

There are options to determine the viscous and wave resistance. The first option is to determine the frictional resistance and wave resistance separately. The frictional resistance can be determined using the International Towing Tank conference correlation formula (ITTC 57 line) (Ortigosa et al, 2009). To determine the wave resistance a regression method such as Holtrop-Mennen (Holtrop & Mennen, 1982) or a theory based on potential flow can be used. The viscous pressure resistance is assumed to depend on a form factor, k, and the friction resistance R_F^* (Molland et al, 2011). The other option is to use a Reynolds-Averaged Navier-Stokes (RANS) equations, Large Eddy Simulation (LES) or Detached Eddy Simulation (DES) based solver to solve the full Navier-Stokes equations and estimate the total resistance.

Early on in the design process a speedy determination of the resistance is of great importance. Since all the ship properties are intertwined it is not beneficial to dwell too much on one parameter. Early on in the process simplicity and speed are more important than accuracy to some degree (Noblesse et al, 2010). The combination of potential flow and ITTC correlation line is an example of such a method. One benefit of potential flow is that the problem is reduced to the size of the wetted surface, whereas RANS solvers require the discretisation of the whole fluid domain which is considerably larger. It is this that gives potential flow its speed; a major advantage (Hess, 1975, Kumar & Philominathan, 2011). Potential flow modelling is based on three simplifications of the flow field; that the homogenous fluid is incompressible and inviscid and the flow is irrotational. This means that the method is only suitable to determine the wave resistance and not the friction resistance since, in an inviscid fluid, there will be no boundary layer. Since RANS solvers do not make these simplifications they can be used to determine the total resistance.

The computational time will depend on many factors such as the complexity of the submerged body and accuracy required but generally speaking a potential flow method will yield a result in minutes, and RANS based solver in hours and a LES method in days (Molland et al, 2011).

Later, as the design becomes more finalised a method with fewer simplifications such as advanced software based on RANS equations is often used. RANS based solvers are often used to model breaking waves, resistance determination related to non-linear movement and local flow phenomena. RANS is also favourable when modelling non-linear surface effects.

In the developments of a new ship, a combination of all of the above mentioned methods are usually applied and personal preferences of the shipyard or the naval architects usually plays an important role. Therefore, there is a benefit to developing all of these methods. To some extent there could also be a cost associated with not refining resistance prediction methods, since stagnated methods tend to become less effective. Without updates, software will generally become less efficient and methods without refinement and further development tend to lose users.

To solve the two part problem of determining the viscous and wave resistance there are two approaches; Froude's (Froude, 1868, Froude, 1877, Froude et al, 1955) and Hughes (1954). In Froude's approach

$$C_t = C_F + C_R \tag{1.5}$$

and in Hughes

$$C_t = (1 + k)C_F + C_w, \tag{1.6}$$

where C_R is the residual resistance coefficient. The differences between the methods are illustrated in Figure 2.

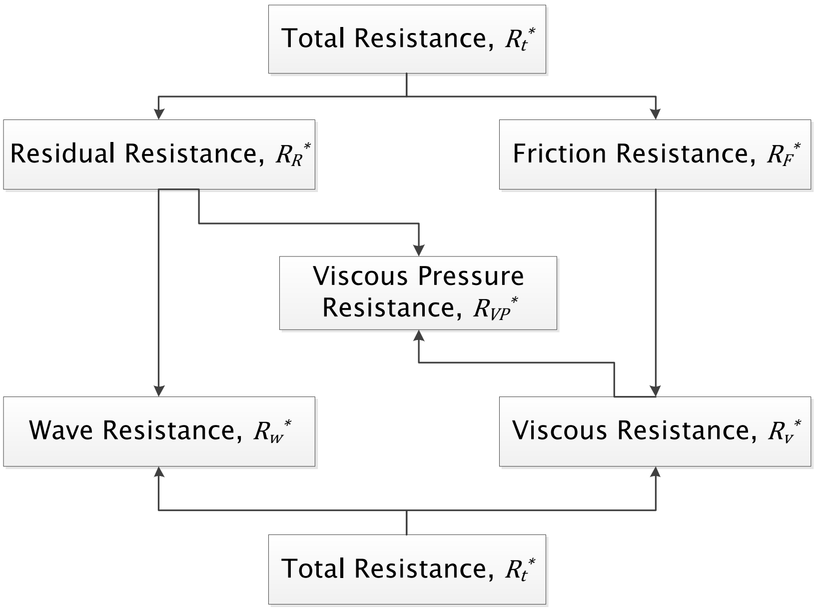

Figure 2 Froude's (top) and Hughes' (bottom) approach to resistance determination

The Hughes method is recommended by the ITTC and is the most adopted, though the form factor approach is not suitable for yachts and some high-speed crafts. Methods of estimating k include experimental, numerical and empirical methods (Molland et al, 2011). The form factor is usually depicted as $(1 + k)$ as seen in (1.6) and typical values lies between 1.05-1.5 (Lauro & Miranda, 1987).

The drawback of Froude's method is that the residual resistance must be determined using model tests. The difficulty with Hughes method is to accurately determine the form factor k.

1.3 Contribution to science

At the dawn of modern naval architecture, scholars thought that damping was important when determining wave resistance. The men that laid the foundations of modern fluid mechanics such as Stokes, Michell, Havelock and Lamb all argued that damping effects are important when determining the wave resistance.

Stokes was a Lucasian Professor with exceptional contribution to the fluid mechanics field. The Navier-Stokes equations, Stokes drift, Stokes' law, Stokes wave and Stokes boundary layer are all named after him. He was made a Baron for his contributions to science. Michell was an Australian mathematician and Royal Society Fellow who published only 23 papers, yet one of them might be the single most important paper regarding ship resistance determination. Havelock was a knighted mathematician and fellow of the Royal Society known for his large productivity and significant contribution to theoretical resistance determination. Lamb was active in the field of applied mathematics and knighted for this work. He published the book Hydrodynamics in 1879 which is still in print and widely used around the world.

When their theories could be implemented on a larger scale using computers it was assumed that the damping could be overlooked, because the computers of yesterday could not handle these far more complex theories. Today's computers are more powerful than ever before and can solve these complex problems. There is therefore a possibility to investigate if the original assumptions and theories regarding the role of damping in resistance determination holds true.

1.4 Aims and objectives

To address this; this thesis aims to develop an efficient numerical method for residual resistance prediction based on an improved potential theory which incorporates certain viscous effects in the model. The underlining methodology will be based on a panel method and a new Green function for the modified governing equations will be derived. Evaluation of the numerical implementation for efficiency and robustness will be undertaken. Validation and evaluation of the approach will be conducted.

The objectives are:

- Using a potential flow theory based model to describe the flow around a steady advancing hull.
- The model should include some damping viscous force to capture the residual resistance.
- Derive a new Green function that includes Rayleigh damping.
- Evaluate and compare the model against existing results to establish some degree of validation.

1.5 Summary of contributions

- A new Green function is derived that is the first in 3D to include a damping parameter.
- A potential flow based model that has the possibility to determine the residual resistance is developed.

1.6 Outline of thesis

This thesis is divided into 7 chapters. Chapter 1 provides the motivation for this study and explains the basics of theoretical resistance prediction. It gives a short account of the application of different methods and their benefits and drawbacks.

Chapter 1 renders the historical aspects of theoretical resistance modelling and why the inclusion of damping in a potential flow based model is pertinent.

Chapter 2 furnishes a general background of the problem with historical remarks. Having commenced with the history of potential flow it next surveys different formulations of Green function. Therefore the differences between potential flow and RANS equations are elucidated and viscosity in potential flow is discussed. Finally resistance determination methods based on potential flow are discussed with comments on existing data.

Chapter 3 explains the basic assumptions and provides a derivation of the governing mathematical model. Starting with the Navier-Stokes equation, the dissipative Bernoulli equation and free surface condition lead to the formulation of the integral identity that governs the relationship between the unknown steady potential and the translating source Green function. Finally a double and single integral representation of the proposed 3D Green function is generated.

In Chapter 4 the numerical implementation of the mathematical model is illustrated together with convergence of the method. Two discretisation methods are explained; thin ship and a panel method. The convergence of the single integrals is established and specific limitations of the double integral are highlighted.

Chapter 5 validates the predicted results with data from other sources. It provides the wave pattern of a single source together with the wave pattern generated by Wigley hull with no Rayleigh damping against existing data. The wave resistance of a submerged ellipsoid and sphere at different depths are compared to existing data from other sources.

In Chapter 6 the proposed method is applied to determine the residual resistance of fully submerged bodies. The possible range of the Rayleigh damping is determined for a fully submerged ellipsoid and sphere at different depths. The wave elevation along a Wigley hull is compared to experimental measurements for different speeds. The wave resistance and residual resistance are compared with experiments for fully submerged ellipsoids at different depths.

Chapter 7 furnishes concluding remarks and thoughts on future work.

2 Literature review

By 1975 over 700 papers had been published on the experimental and/or theoretical study of ship waves and wave resistance (Baar, 1986). It is therefore not possible to give an account of them all, hence a general background and a pertinent historical context is disclosed.

2.1 History of potential flow

Potential flow can be said to have its base in a series of papers by Euler in the 1750's. Euler developed a field theory based on Newton's laws, the Euler-Lagrange differential equations (Euler, 1755a, b, c, 1756, Saad, 2008-2011). This field theory included velocity and pressure unlike prior field theories. In 1821 Navier gave what is today known as the Navier-Stokes equations for incompressible fluids and in 1822 for viscous fluids, he was the first to introduce a non-ideal fluid (Anderson, 1997). Even though the equations were first presented by Navier, it was first correctly derived by Saint-Venant (Anderson, 1997).

The field variable, developed by Euler and improved by Lagrange (1781) and Laplace was ideal to solve the Navier-Stokes equations in the entire fluid domain (Ball, 1960). Lagrange developed Euler's field variable to be applied to potential flow. This potential could also describe the fluid flow if it was assumed to be irrotational. Lagrange described what is today know as streamlines, the orthogonal lines in the flow with makes it possible to use Bernoulli's equation to determine the pressure in the fluid. Laplace proved that the field variable must satisfy a differential equation that today is known as the Laplace equation (Ball, 1960).

The wave profile for a surface wave was described by Green (1828) and Airy (1841). The potential under a surface wave over the seabed was proposed by Stokes (1847).

Modern analytical resistance predictions are said to have been founded by Michell at the turn of the last century (Michell, 1898). For a long time the Michell thin ship theory, which only applies to slender ships was the only available theoretical evaluation of wave resistance. Michell touched upon the important subject of damping. Quoting from Michell's paper "… similar work to that of the present paper gives a theory of the damping of the oscillation of ships due to wave-making. This I hope to give in a subsequent paper". But he did not, he did not publish any paper after 1902 and this problem was not solved until years later by Havelock and Newman (Tuck, 1989).

Rayleigh damping was first introduced by Lord Rayleigh (1877) it is a viscous damping that uses a dissipative function to describe a damping that is proportional to the flow speed.

2.2 Different formulations of Green function

Most mathematical functions are adjectival in English, unlike most other European languages. Green function is the sole exception and can be called both Green and Green's function. Throughout the last century the fashion has shifted back and forward regarding the possessive use of Green function (Wright, 2006). Here Green function is used.

Green function can be expressed either as a fundamental Rankine source or as the potential of a translating submerged source which satisfies the free surface condition and the infinity condition, where the last option is referred to as the Kelvin wave source potential (Baar & Price, 1988a, Kelvin (Thomson), 1887). The Rankine source is considerably easier mathematically but the Kelvin source has the numerical advantage since it does not require sources to be placed on the free surface (Ponizy et al, 1998). However, the Kelvin source is still cumbersome to evaluate and methods such as eigen-function expansion, power-series expansions, asymptotic expansions, continued fraction or multidimensional polynomial approximations may be needed (Newman, 1985).

There are two major approaches that can be considered to solve the Kelvin wave source potential problem other than Michell (Baar, 1986). The first is introduced by Havelock (1928) and expanded in (1932), inspired by the work of Lamb (1926). It is interesting to note that Havelock inserted a small friction force into the equation of motion. The Havelock expression was later modified by, among others, Lunde (1951) and is considered the most popular expression. Wigley (1934) has compared both Havelock's and Michell's theories against experimental results but using an inviscid version of Havelock method. Thorough evaluation of analytical methods compared to experimental results has been undertaken by Eggers focusing on the method by Havelock (Eggers et al, 1967). Besides the methods by Havelock and Michell there is a third method by Peters (1949). However he considered the dissipation factor μ, used by Lamb (1945) as unnecessary. According to Baar (1986) there are two more methods, one originally by Bessho (1964) and one by Demanche (1981), however Baar considers that they do not have “any practical advantages”. Bessho formulation is sparsely quoted in the literature perhaps because he published it in a Japanese journal not widely available or because his mathematical argument was given in outline rather than in detail (Ursell, 1984). The details of the derivation were not fully explained until the 1980s, when Ursell (1984) proved that the order of integration could in fact be changed, which had previously been disputed in the Bessho formulation. Therefore; the formulations by Michell, Havelock and Peters are considered to be the main solutions. The main difference between them is that they use different mathematical approaches, such as the integration path for the double integral. All representations has the same asymptotic behaviour to ensure that the free waves trail aft of the disturbance (Eggers et al, 1967).

The difficulties with these formulations depend on the mathematical complexity of Green function. The Michell, Havelock and Peter formulations include a single integral for the near field disturbance. Havelock and Peters formulations also has a single integral for the wavelike disturbance (Michell has the wavelike disturbance as a double integral).

Noblesse (1981) has derived the three single integral formulations in a uniformed manner which is both easy and straight forward to follow. He used a double Fourier transform in order to derive the Green function. The near field disturbance becomes a single integral with an exponential as the integrand. The exponential integral can be expressed as a standard function $E_1(\chi)$ and is numerically regarded as a standard function (Abramowitz & Stegun, 1964). The formulations by Noblesse are difficult to integrate numerically since they include highly oscillatory integrands (Baar & Price, 1988a). The far field or wave like disturbance is generally the more cumbersome integral to evaluate due to its highly oscillatory behaviour (Ponizy et al, 1998). Monacella (1966) simplified the problem by only evaluating the far field integral and thus obtaining a solution which is only valid for large distances, r, between the source and field point. Therefore, the solution cannot be used to calculate the pressure on the body, Monacella uses it to determine the pressure on the seabed, and the method could be changed fairly easily to calculate the wave pattern far downstream.

2.2.1 Surface piercing bodies

A major difficulty to overcome is to determine the derivatives of the unknown distributions of Kelvin sources in the water line integral where the hull meets the free surface (Ponizy et al, 1998). It can be shown that a line singularity distribution should accompany the distribution over the hull (Brard, 1972). The methods by Baar (1986), Baar and Price (1988a, b) and Doctors and Beck (1987a, 1987b) were compared and evaluated by Marr and Jackson (1999). Marr and Jackson were unable to reproduce the results of Baar and Price (1988a, b) for the Wigley hull with a water line integral. They found a very good agreement for submerged thin bodies. However, for these bodies the water line integral is not important. Marr and Jackson drew the conclusion that at least one of the pairs of authors (Baar and Price, Doctors and Beck, Marr and Jackson) have calculated the water line integral incorrectly or the water line integrals exhibit some behaviour which is not yet understood. They state that “the Neumann-Kelvin theory as it is currently understood does not give satisfactory wave resistance results for idealized ship hull forms”. Belibassakis et al. (2013) handles the problems associated with the water line integral by downshifting the whole hull by a small parameter.

2.3 Potential flow versus RANS

Today the most common methods to determine the wave resistance are either using a potential flow solver or a program that solves the full Navier-Stokes equation, such as RANS solver. Using RANS solver, the fluid is considered to be viscous and rotational, unlike potential flow. Many argue that RANS often gives a more accurate result, but the potential flow methods are faster (Bal, 2008). Since RANS solves the full Navier-Stokes equation the method can cope with a variety of non-linear flow phenomena such as turbulence, shock waves and breaking waves (Miyata, 1996).

It is reasonable that a method that includes more of the physics would yield better results (however it is not always the case). Because water is a viscous fluid; a model that includes more viscous effects could improve the results. When looking at propagating waves from a ship it is evident that the physical phenomenon of damping affects the wave decay. A full RANS based CFD solver usually requires more of the user in terms of data input and the ability to interpret information to make sure that everything is physically correct; an example is ‘meshing’. To generate an appropriate discretisation of the entire fluid domain can be very time consuming, taking up both computational time and man-hours. Mesh generation has become so complex it has developed into a research field of its own (Argyris & Patton, 1966, Monaghan, 1988). A potential based program requires less input data from the user making the procedure less dependent on the user.

Havelock did not evaluate all his theories; some of them were computed (by hand) by Wigley. With the dawn of modern computers his ideas could be implemented on a larger scale. Havelock (1928, 1932) originally wanted a damping parameter to be included in the resistance expression. However some simplifications had to be made to simplify his resistance expression so the damping was assumed to be negligible. Quoting Newman (1970) “To make analytical progress we must ignore viscous effects, which are known to be significant in the steady-state resistance problem”. However computers have increased the speed rapidly over the last decades, until now Moore’s law that states that the number of transistors on integrated circuits doubled every two years has held true (Moore, 1965). The number of transistors strongly influences processing speed and memory capacity. This makes it possible to implement theories previously thought to be too complex. However it is likely that the doubling of computational speed associated with Moore’s law has come to a halt (Schenkman, 2009). So a good numerical implementation scheme is still crucial for the evaluation of Green function.

2.4 Viscosity in potential flow

Viscous potential flow is not a common idea and to some it is even an oxymoron. Stokes (1851) first suggested inclusion of some viscosity in potential flow to better model dissipation of energy. Lamb discussed the importance of viscosity on gravity waves in deep water, his solution was to have an irrotational but still dissipative fluid (art 348, 349 Lamb, 1945). He also studied the viscous decay of small oscillations of a mass of liquid about a spherical form (art 355) (Lamb, 1945). Havelock on the other hand treated the dissipative viscosity as something so natural that it need no extra comments (Havelock, 1928, 1932). He wrote “It seems fairly certain that one of the main causes of differences between theoretical and experimental results is the neglect of fluid friction in the calculation of ship waves”. He introduced a reducing factor to represent the effect of friction. Even though his results were not comprehensive, he stated that the success of such a factor depends on its independence of speed and hull shape (Havelock, 1935).

A newer contribution to viscous potential flow is the case argued by Joseph (2006) who strongly believes that viscosity should be incorporated into potential flow to enhance its results. The difference between his method, Viscous Potential Flow, (VPF), and conventional potential flow is that the viscous component for the normal stress at the free surface is included in the normal stress balance.

However, most of his applications concern gas bubbles. He also states that viscosity may act strongly in regions in which the vorticity is effectively zero, in cases involving gas bubbles or rotating cylinders (Joseph et al, 1993).

2.5 Methods of determining wave resistance

Methods to theoretically calculate wave resistance can be divided into two main methods (Harvald, 1983):

A. The flow around the hull is determined to provide the pressure on the hull. The pressure is then integrated over the hull surface to get the resistance.
B. The wave pattern generated by the ship is calculated. The resistance is then determined from the flow of energy necessary to maintain the wave system.

2.5.1 Panel method

Computing wave resistance by integrating the pressure over the hull is a very common method. However, it is very sensitive to the hull panelling, in particular, at low Froude numbers (Raven, 1991). Because the integrals describing the flow within the whole domain are transformed to integrals associated with a set of boundaries this method is sometimes referred to as Boundary Element Method (BEM). Sometimes the approach is designated as a ‘panel method’ because the boundary is discretised into panels (Denayer, 1978, Wördenweber, 1980). Panel methods were developed and proven firstly in 2D (Smith & Pierce, 1958) and have been available in 3D since the 1960s (Hess & Smith, 1964). The predictions using panel methods have been found to agree well with experimental results. In cases where the agreement has been poor they continue to be useful in the design process, because they can predict the incremental effect of a design change (Hess, 1990).

2.5.2 Egger series transverse cut technique

The concept of determining wave resistance from the wave pattern, without reference to the ship, was originally proposed by Havelock (1934a, b). Janson and Spinney (2004) and Raven and Prins (1998) argued that a method based on the predicted wave pattern is much less sensitive to the particular hull discretisation than resistance estimation via pressure integration. However, panel methods are more widely used. Eggers (1962) showed that using linear theory, the wave pattern behind a ship can be expressed as a summation of series of discrete wave modes. Each mode is described as a sinusoidal wave train with a particular amplitude, phase, wave number and direction. Measurements of the real wave pattern are used to recreate the theoretical wave pattern and from this the corresponding resistance can subsequently be obtained (Eggers, 1962, Hogben, 1972). There are three main approaches, either a transverse cut, a longitudinal cut and a combination of a transverse or longitudinal cut method known as the “X-Y” method. The last approach is also described as a longitudinal cut method with a truncation term (Eggers et al, 1967). For numerical methods the transverse cut is superior partly due to the fact that the wave profile is clearly finite (Nakos, 1991, Nakos & Sclavounos, 1994, Raven & Prins, 1998). The transverse cut also benefits from the limited extent of the discretisation that is needed downstream of the ship (Nakos & Sclavounos, 1994).

A minimum of two cuts are needed to determine the two unknown wave parameters but it has been shown that a larger number of cuts are needed to provide redundancy and increase accuracy of the predicted wave resistance (Janson & Spinney, 2004, Raven & Prins, 1998). The transverse cuts must be far enough aft of the ship, they must extend outside of the Kelvin wedge and the resolution must be high enough to show all components of interest (Raven & Prins, 1998). The Kevin angle or wedge is illustrated in Figure 3.

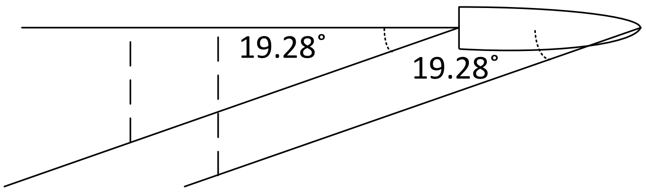

Figure 3 Kelvin angle

According to Raven and Prins (1998) the wave resistance is supposed to be independent of the location of the cuts, however both their results and the results by Janson and Spinney showed that this is not the case. The first cut must be $0.5L^*$ aft of the stern to avoid the near-field disturbance which causes sharp variations in the resistance due to the location of the cut. (Nakos, 1991, Nakos & Sclavounos, 1994, Raven & Prins, 1998).

Raven and Prins (1998) and Janson and Spinney (2004) found that the resistance varies around a mean line and decreases with increasing distance of the cuts behind the ship, if the cuts are further downstream the resistance will be lower, due to numerical damping. They also found that all values of the wave pattern resistance were lower than the resistance due to pressure integration on the hull. Raven and Prins (1998) found that the waviness in the resistance had a length close to the fundamental wave length of equation (1.4) . Fluctuation in the resistance could be avoided if the eight cuts that they used were distributed over an area of one wave length because the variations will cancel and much more constant result can be obtained. As stated before, two cuts is the minimum number of cuts, but a higher number of cuts are needed to increase accuracy. Janson and Spinney (2004) used 10 cuts, Raven and Prins (1998) used 8 cuts and Sharma (1963, 1966) concluded that at least 5 cuts are required to ensure the error does not exceed 5 %. Janson and Spinney (2004) also mentioned that "certain numerical problems" can be avoided by using non-equidistant spacing between the cuts. 10 cuts with a non-equidistant spacing with a multiplication factor of 1.1 according to Janson and Spinney (2004) and Fürth et al. (2013) (see Appendix A) are illustrated in Figure 4.

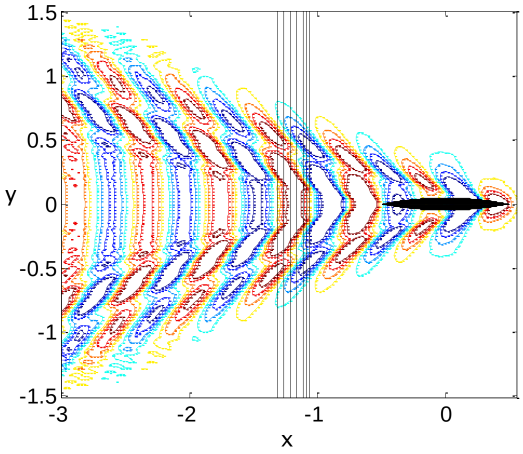

Figure 4 Location of the 10 cuts behind a Wigley hull at $Fn = 0.3$

Nakos (1991) also states the importance of the location of the transverse cuts and that the method needs to be free from numerical damping if cuts at large distances aft of the ship are allowed. However, the dependence on the longitudinal location of the cuts is eliminated only at an infinite distance from the hull due to the discretisation of the surface (Nakos & Sclavounos, 1990). Nakos (1991) concluded that it is hard to get convergence at the downstream end of the computational domain due to the abrupt truncation of the free surface. It has been shown that the wave pattern resistance is only equivalent to the wave resistance via integrated pressure if the body is submerged, which is an inconsistency referred to as Gadd's paradox (Nakos, 1991, Nakos & Sclavounos, 1994).

A conventional form of the transverse cut technique will give a lower wave resistance estimation for higher Rayleigh damping, since higher damping generates lower wave profiles. Where higher damping should imply higher resistance since the modelled water would be more viscous. Fürth et al. (2013) (see Appendix A) derived a modified and new form of the Eggers series transverse wave cut technique that determined the wave resistance of a dissipative wave pattern. This method retains many aspects of the conventional transverse wave cut and still has its main benefit; the whole wave pattern does not need to be known, only the profile in the cuts. The details of the method are given in Appendix A, the main aspects of the method are reiterated here together with the main limitations.

The wave resistance for a dissipative flow can be determined using a control volume analysis around the hull as illustrated in Figure 5.

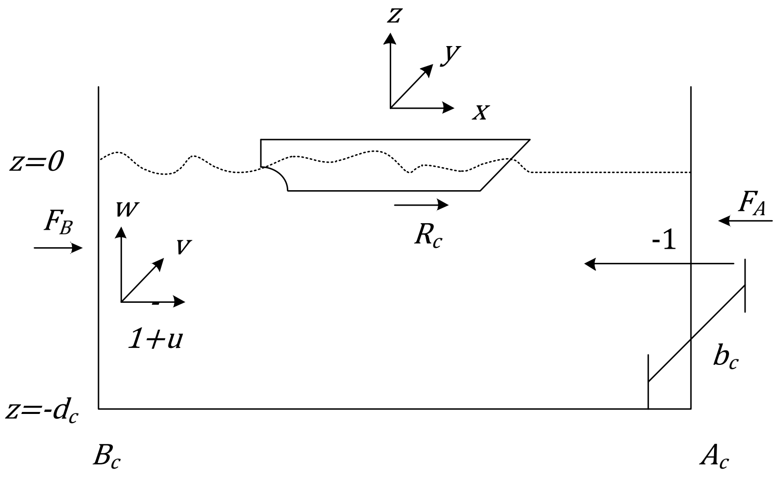

Figure 5 Control volume enclosing advancing ship

Here R_c is the resistance force experienced by the fluid within the control volume. F_A is the pressure force acting on surface A_c from outside the control volume and F_B the corresponding force acting on the surface B_c. The non-dimensionalised free stream is designated -1 whereas (u, v, w) specify the speed components of the water in the (x, y, z) directions due the disturbance created by the advancing ship. The sea bed is located at $-d_c$ and the width of the control volume is b_c.

The wall reflection condition for a ship in a tank of limited width, b_c, is introduced to simplify the resistance expression. This simplified form is found to be so convenient that it is recommended, even if the tank happens to be so large that is practically of infinite width (Eggers et al, 1967).

The ship is fixed so that

- The wave pattern is symmetrical and stationary
- The wave pattern moves with the model
- The wave pattern reflects that there is no flow through the tank walls

The dissipative Egger series includes some simplifications that differ from the conventional form. These simplifications are made in order to limit the cumbersomeness of the resistance expression. There is however a risk that the simplifications are more mathematically than physically justified.

The potential for a freely moving wave is assumed to be a separable equation that must satisfy the free surface conditions together with a Neumann condition on the seabed. Usually the dispersion relationship is given by inserting the potential for a freely moving wave into the combined free surface condition. However the dissipative potential for a freely moving wave perfectly satisfies the free surface condition so the relationship between the wave number and speed of the wave has to be set. The wave pattern is port-starboard symmetric and therefore the potential must be symmetric with respect to y. The exponential decay dependant on μ_R' in the potential must be approximated as the decay along the x axis only and not along the travel direction of the wave.

These simplifications are not sufficient to determine the resistance. All damping terms must be removed from the velocities and wave profile in order to get a resistance expression that is independent of the downstream end of the control volume.

This leaves a damping term only in the expression for the Fourier coefficient used to determine the unknown wave parameters. This is enough to create an Egger series that takes a dissipative wave pattern into consideration.

Because of the tenuous justifications for some of the mentioned simplifications, the modified Egger series transverse cut technique is not considered suitable for further evaluation as part of the current project.

The method has some limitations at large Froude numbers (see Appendix A) but it is currently unclear if this depends on the modified Egger series or the use of the double integral (as opposed to the single integrals) in evaluating Green function or some other limiting factor.

2.6 Data from other sources for an ellipsoid

Validation is very important when developing a novel computational method. Here a short survey of existing data and the methods used to obtain the data are shown. Both theoretical and experimental data from other sources for the Wigley hull are abundant, see for example Chen and Noblesse (1983), Noblesse et al. (1989) and Huan and Huang (2007). When investigating the effect on the surface elevation by a submerged object, the object may in most cases be approximated to an ellipsoid shape (Dong et al, 2013). However experimental data for an submerged ellipsoid are scarce to the author's knowledge and consist only of that provided by Weinblum et al. (1950) and Farell and Güven (1973).

The velocity potential due to an ellipsoid moving in an infinite fluid is given by Lamb (1945) for an inviscid fluid (art 114) and a viscous fluid (art 339) and by Milne-Thomson (Chapter 16.52 1962). The potential wave resistance coefficient for a submerged ellipsoid is given by Inui (1954).

Farell (1973) semi-analytical method to determine the wave resistance has become somewhat of a benchmark and a very popular solution to validate new methods against.

A comparison for the free surface elevation for a submerged ellipsoid is given by Tuck and Scullen (2002) and Tuck et al. (1999b, Tuck et al, 1999a). They compare the elevation from a "Neumann-Stokes" (exact body and surface condition) mode, "Neumann-Kelvin" (exact body condition and linearised free surface condition) and thin ship theory. They found an average error of 5% for the Neumann-Kelvin solution and thin ship theory compared to the Neumann-Stokes, but in some locations of the wave profile for shallow submersion the error was as much as 50% when comparing thin ship theory to the Neumann-Stokes solution.

C_w is given for a submerged prolate spheroid using a Newman-Kelvin formulation by Doctors and Beck (1987a), Andrew et al. (1988) and Price et al. (1989) and Ponizy (1998). Price et al. also determine the wavemaking resistance for an ellipsoid in water with different layered density. The wave resistance and surface elevation due to a prolate spheroid is given by Lalli et al. (1999) applying a desingularised boundary integral method and a longitudinal cut technique and by Lalli et al. (1992) using a fully non-linear Dawson method.

Belibassakis et al.(2010, 2013) used a submerged ellipsoid travelling close to the free surface to validate their isogeometric higher order panel method.

The wave-making resistance of a submerged ellipsoid in shallow water was investigate by Kinoshita and Inui (1953). Eng and Hu (1963) tried to give an optimum ellipsoid shape for different Froude numbers and depths based on an analytical resistance expression of the shape of the ellipsoid. Effects on the surface elevation from speed and submersion of the ellipsoid is also investigated by Uslu and Bal (2008) using a Dawson (Rankine source) method. Dong et al. (2013) states that the free surface was not affected by the submerged ellipsoid if the submersion depth was three times larger than the ellipsoid diameter. They also concluded that at this depth the free surface did not affect the drag using an incompressible RANS based method.

3 Mathematical model

In this study the fluid is assumed to be inviscid and incompressible and the fluid flow is irrotational, but it includes some damping. The flow is to be considered around a single ship or submerged body which moves in a straight line in an otherwise undisturbed fluid. The computational domain is considered infinitely deep and extends infinitely in the horizontal directions. The coordinate system is body-fixed amidships as shown in Figure 6. The variables are non-dimensionalised using Table 1.

The problem is modelled using a Neumann-Kelvin formulation, which simplifies the free-surface condition by linearisation, allowing the use of a fundamental solution (Kelvin source) as a building block. From this, the flow around a hull is produced. Several solutions to this problem were modelled in the 1980's by Baar (1986) , Baar and Price (1988a, b), Newman (1987a, 1987b) and Doctors and Beck (1987a, 1987b). Marr (1992) aimed to improve the speed and accuracy of the model developed by Baar and Price (1988a, b) by inclusion of what he called "the missing term" originally derived by Ursell (1988).

To model the problem a right-handed Cartesian coordinate system $Oxyz$ is used. It moves steadily with the ship in the direction of Ox. Here Oxy is the undisturbed water surface, and the midship section of the ship is on the Oyz plane. Oz denotes the direction opposite to the gravitational acceleration g.

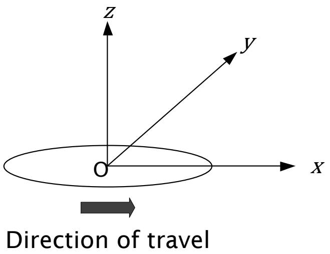

Figure 6 Coordinate system, origin is amidships

The physics of the fluid flow is described mathematically by governing equations. The rate of change of momentum within a control volume is equal to the net rate at which momentum enters and leaves the control volume plus the force that acts on the body (viscous-, pressure- and body forces). The set of equations obtained is known as the Navier-Stokes equations.

Dimensional variables are non-dimensionalised in terms of $\rho^* L^{3^*}$ for mass, L^* for length and L^*/U^* for time, where ρ^* is the density of water, L^* is the length of the submerged shape and U^* is the speed of the submerged shape/ship. The non-dimensionalised variables are shown in Table 1.

Table 1 Definition of non-dimensional flow variables

Variable	Dimensional	Non-dimensional
Density of water	ρ^*	$1 = \rho^*/\rho^*$
Length of ship	L^*	$1 = L^*/L^*$
Free stream velocity	U^*	$1 = U^*/U^*$
Acceleration of gravity	g^*	$g^* L^*/U^{2^*} = 1/Fn^2$
Coordinates	x^*, y^*, z^*	$x, y, z = (x^*, y^*, z^*)/L^*$
Speed of ship	$\boldsymbol{q}^* = (u^*, v^*, w^*)$	$\boldsymbol{q} = (u, v, w) = \boldsymbol{q}^*/U^*$
Gradient operator	∇^*	$\nabla = \nabla^* L^*$
Rayleigh damping parameter	μ_R^*	$\mu_R' = \mu_R^* L^*/(\rho^* U^*)$
Pressure	p^*	$p = p^*/(\rho^* U^{*2})$
Time	t^*	$t = t^* U^*/L^*$
Potential	Φ^*	$\Phi = \Phi^*/(U^* L^*)$

3.1 Potential flow

In the potential theory, fluid is modelled using field functions and the fluid velocity is the gradient of the velocity potential Φ. The fundamental approach when modelling the problem in a potential flow theory is that bodies submerged in the fluid (or boundaries such as channel walls or the sea bed) are modelled using fluid singularities such as: sources, sinks, vortices and doublets. A source is like a mathematical geyser pushing fluid out in all directions, a sink similarly sucks in fluid, a doublet is a source and a sink at the same location and a vortex is a point around which the flow rotates. The contribution from each source/sink, doublet and vortex can be linearly added together to build the flow field by appealing to the superposition principle. For example; instead of a wall which will reflect the incoming flow, a distribution of sources is used. This will have the same effect on the flow as a reflecting wall. A schematic picture of a source, doublet and vortex are shown in Figure 7.

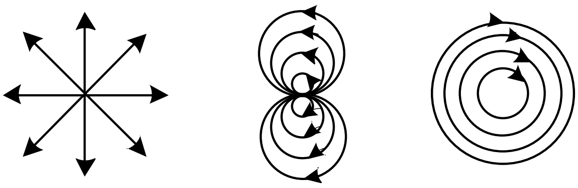

Figure 7 Streamlines of a source, a doublet and a vortex

To model a body in the fluid, sources are distributed over the corresponding wetted surface of the body of interest. Ideally the sources would be distributed continuously over the body; however that is numerically more demanding. For that reason a panel method is used. The corresponding surface of the submerged object is divided into small panels. The panels may be of different size, but size and panel distribution should represent both the geometric shape and an appropriate distribution of wetted surface boundary conditions. On each panel a source is placed at the centroid and is assumed to have constant strength over the panel. The strength of the sources ultimately depends on body geometry, location of structure relative to the free surface and the form of the fluid structure interaction being experienced by the structure. The role of the source is to ensure that the boundary condition on the body is satisfied. For the particular subject of this dissertation the wetted surface boundary condition is of the Neumann form; there can be no flow through the submerged body as defined in:

$$\frac{\partial \Phi}{\partial \boldsymbol{n}} = 0 \; on \; the \; body \; surface. \tag{3.1}$$

Here and throughout $\boldsymbol{n}$ is the normal to the surface pointing into the fluid.

3.1.1 Laplace equation

For the purpose of ship analysis, water can be viewed as incompressible. The density within the fluid must thus be constant, and the continuity equation then becomes

$$\nabla \cdot \boldsymbol{q} = 0. \tag{3.2}$$

The curl of the velocity field is called vorticity and is a measure of how much a fluid element rotates. The vorticity vector is twice the rate of rotation (angular velocity) of the fluid element. It is assumed that the vorticity of the fluid is low so that the fluid can be assumed to be irrotational. For an irrotational fluid the vorticity is zero, that is

$$\nabla \times \boldsymbol{q} = 0. \tag{3.3}$$

Inside and close to the boundary layer viscosity is of greater importance. However, outside of the boundary layer and the wake the fluid can be assumed inviscid. Here the fluid flow outside of the boundary layer is of interest so the flow is assumed to be inviscid.

The damping force to be introduced is the product of the constant, μ_R', and the associated disturbed velocity in the body fixed coordinate system. The damping coefficient is generally referred to as Rayleigh damping. This will give the same dynamic free surface condition as obtained by Havelock (1928, 1932), viz

$$\frac{\partial^2 \phi}{\partial x^2} + \kappa_0 \frac{\partial \phi}{\partial z} - \mu \frac{\partial \phi}{\partial x} = 0, \tag{3.4}$$

where $\kappa_0 = g^*/U^{*2}$ and μ Havelock's damping parameter. The non-dimensional Navier-Stokes equations with Rayleigh damping for an inviscid, incompressible and irrotational fluid can be expressed using the single vector equation

$$\frac{D\boldsymbol{q}}{Dt} = -\nabla p + \frac{1}{Fn^2}\begin{pmatrix}0\\0\\1\end{pmatrix} - \mu_R'\left(\boldsymbol{q} + \begin{pmatrix}1\\0\\0\end{pmatrix}\right). \tag{3.5}$$

The potential field Φ is defined such that

$$u = \frac{\partial \Phi}{\partial x}, \quad v = \frac{\partial \Phi}{\partial y}, \quad w = \frac{\partial \Phi}{\partial z} \tag{3.6}$$

it follows that

$$\boldsymbol{q} = \nabla \Phi. \tag{3.7}$$

Substituting (3.7) into the incompressible continuity equation (3.2) gives the Laplace equation

$$\nabla^2 \Phi = 0. \tag{3.8}$$

3.1.2 Bernoulli pressure equation

Expanding the left hand side of the modified Navier- Stokes equation (3.5) gives the following:

$$\frac{D\boldsymbol{q}}{Dt} = \frac{\partial \boldsymbol{q}}{\partial t} + \frac{1}{2}\boldsymbol{\nabla q}^2 = -\nabla p - \frac{1}{Fn^2}\begin{pmatrix}0\\0\\1\end{pmatrix} - \mu_R'\left(\boldsymbol{q} + \begin{pmatrix}1\\0\\0\end{pmatrix}\right). \tag{3.9}$$

Where Fn is the Froude number, μ_R' is the Rayleigh damping parameter and ∇p is the pressure gradient. It will be shown that this Rayleigh damping is consistent with the damping coefficient introduced by Havelock (1928, 1932). Inserting the velocity potential into equation (3.9) gives

$$\nabla\left(\frac{\partial \Phi}{\partial t} + \frac{1}{2}|\nabla\Phi|^2 + p + \frac{1}{Fn^2}z + \mu_R'(\Phi + x)\right) = \mathbf{0}. \tag{3.10}$$

The unsteady non-dimensional Bernoulli equation with added Rayleigh damping is

$$\frac{\partial \Phi}{\partial t} + \frac{1}{2}|\nabla\Phi|^2 + p + \frac{1}{Fn^2}z + \mu_R'(\Phi + x) = F(t). \tag{3.11}$$

For the steady case this becomes

$$\frac{1}{2}|\nabla\Phi|^2 + p + \frac{1}{Fn^2}z + \mu_R'(\Phi + x) = const. \tag{3.12}$$

3.1.3 Free surface condition

Assuming that the fluid is of infinite extent in all directions, seabed and upstream/downstream boundaries can be considered far away from free surface and ship respectively.

The mathematical model must limit the water to the domain below the free surface. This is done by imposing two physical conditions; the kinematic free surface condition and the dynamic free surface condition.

The kinematic free surface condition states that a particle on the free surface must remain on the free surface, because if the particle moves, the surface (the intersection between the water and the air) must move as well. The dynamic free surface condition states that the pressure must be equal on either side of the free surface. The mathematical expression of each physical free surface condition is considered next.

3.1.3.1 Kinematic free surface condition

Let $\zeta(x, y)$ measure the variation of the free surface elevation above its mean datum. Introducing a function, F, this variation satisfies

$$F = \zeta(x, y) - z = 0. \tag{3.13}$$

The total derivative of (3.13) is

$$\frac{DF}{Dt} = \frac{D}{Dt}(\zeta - z) = 0 \tag{3.14}$$

and in expanded form is expressed as

$$\frac{\partial \zeta}{\partial t} + \frac{\partial \Phi}{\partial x} \cdot \frac{\partial \zeta}{\partial x} + \frac{\partial \Phi}{\partial y} \cdot \frac{\partial \zeta}{\partial y} + \frac{\partial \Phi}{\partial z} \cdot \frac{\partial \zeta}{\partial z} - \frac{\partial \Phi}{\partial z} = 0, \tag{3.15}$$

given that ζ is not a function of z, and z and t are independent variables. Introducing the perturbed velocity potential ϕ and moving the coordinate system from a global to a local ship fixed coordinate system which is time independent.

$$\Phi = -x + \phi \tag{3.16}$$

lead to

$$\frac{\partial \zeta}{\partial t} - \frac{\partial \zeta}{\partial x} + \frac{\partial \phi}{\partial x} \cdot \frac{\partial \zeta}{\partial x} + \frac{\partial \phi}{\partial y} \cdot \frac{\partial \zeta}{\partial y} + \frac{\partial \phi}{\partial z} \cdot \frac{\partial \zeta}{\partial z} - \frac{\partial \phi}{\partial z} = 0. \tag{3.17}$$

This is the non-linear kinematic free surface condition.

The steady state kinematic surface condition (3.17) can be linearised, assuming that products of $\partial\zeta/\partial x, \partial\zeta/\partial y, \partial\phi/\partial x, \partial\phi/\partial y$ are small and can be ignored.

3.1.3.2 Dynamic free surface condition

Rewriting the steady state Bernoulli equation (3.11) and assuming the pressure on the free surface ($z = \zeta(x, y)$) is the atmospheric pressure. The pressure can be set to any reference value and so is set to zero. When $x \to \infty$ and $\phi \to 0$ it can then be seen that the constant in Bernoulli equation (3.12) is ½, since

$$\frac{1}{2}|\nabla\Phi|^2 \equiv \frac{1}{2}\left(1 - 2\frac{\partial \phi}{\partial x} + |\nabla\phi|^2\right) = \frac{1}{2} \tag{3.18}$$

and thus (3.12) may be expressed as:

$$\frac{1}{2}|\nabla\Phi|^2 + \frac{1}{Fn^2}\zeta + \mu_R'(\Phi + x) = \frac{1}{2}. \tag{3.19}$$

Rearranging the last equation the surface profile is then expressible as:

$$\zeta = -Fn^2\left(\frac{1}{2}|\nabla\Phi|^2 + \mu_R'(\Phi + x) - \frac{1}{2}\right) \tag{3.20}$$

and upon appealing to the definition of the perturbed in potential (3.16), the surface profile becomes

$$\zeta = -Fn^2\left(\frac{1}{2}|\nabla(-x+\phi)|^2 + \mu_R'(-x+\phi+x) - \frac{1}{2}\right). \tag{3.21}$$

By linearisation with respect to small velocities it is assumed that $|\nabla\phi|^2$ is negligible and so the wave profile

$$\zeta = -Fn^2\left(\frac{1}{2}\left(1-2\frac{\partial\phi}{\partial x}\right) + \mu_R'\phi - \frac{1}{2}\right) \tag{3.22}$$

reduces to

$$\zeta = Fn^2\left(\frac{\partial\phi}{\partial x} - \mu_R'\phi\right). \tag{3.23}$$

3.1.3.3 Combined linearised free surface condition

To eliminate the unknown ζ and to obtain a condition only involving the perturbed velocity potential the kinematic and dynamic free surface conditions are combined. The time independent linearised free surface condition is

$$\frac{\partial\zeta}{\partial x} + \frac{\partial\phi}{\partial z} = 0. \tag{3.24}$$

To derive the combined free surface condition the expression for ζ in (3.23) is differentiated with respect to x and then inserted into the linearised kinematic free surface condition (3.24). Differentiating the linearised dynamic free surface condition (3.23), with respect to x gives

$$\frac{\partial\zeta}{\partial x} = F_n^2\left(\frac{\partial^2\phi}{\partial x^2} - \mu_R'\frac{\partial\phi}{\partial x}\right). \tag{3.25}$$

This is substituted into the linearised kinematic free surface condition (3.24) and gives the combined free surface condition

$$\frac{\partial^2\phi}{\partial x^2} - \mu_R'\frac{\partial\phi}{\partial x} + \frac{1}{Fn^2}\frac{\partial\phi}{\partial z} = 0 \tag{3.26}$$

which is consistent with the expression by Havelock (1928, 1932) stated in (3.4).

3.2 Integral identity

The concept of Green functions was developed in the 1820s by the English mathematician George Green (1828). In physics, it is used to solve various field problems. A Green function is a function that can be used to solve an inhomogeneous differential equation with boundary conditions.

Green functions are equally useful in solving partial differential equations with satisfaction of their associated boundary conditions. To facilitate this advantage in this case an identity known as Green's second identity will be established from first principles, so that an equivalent integral formulation may be subsequently developed to reflect the influence of the introduced Rayleigh damping.

3.2.1 Integral equation for the velocity potential

The integral identities to be derived describe the relationship between the unknown perturbation potential ϕ and the Green function, G, and can be obtained by appealing to Green's second identity. In the process of deriving the integral identity a set of conditions are identified as being a sensible constraint to impose on the sought Green function. These conditions are then used explicitly to derive the Rayleigh damping sensitive Green function from first principles.

The finite domain Ω is bounded by the hull surface h, the finite mean free surface s' and an exterior surface h_∞ surrounding the hull surface $h. c_h$ and c_∞ are the intersection curves of h and h_∞ with the plane $z = 0$ respectively, d_i is the inner domain bounded by the hull surface h and the inner free mean surface s_i and $\boldsymbol{n}$ is the outward normal from the body as illustrated in Figure 8.

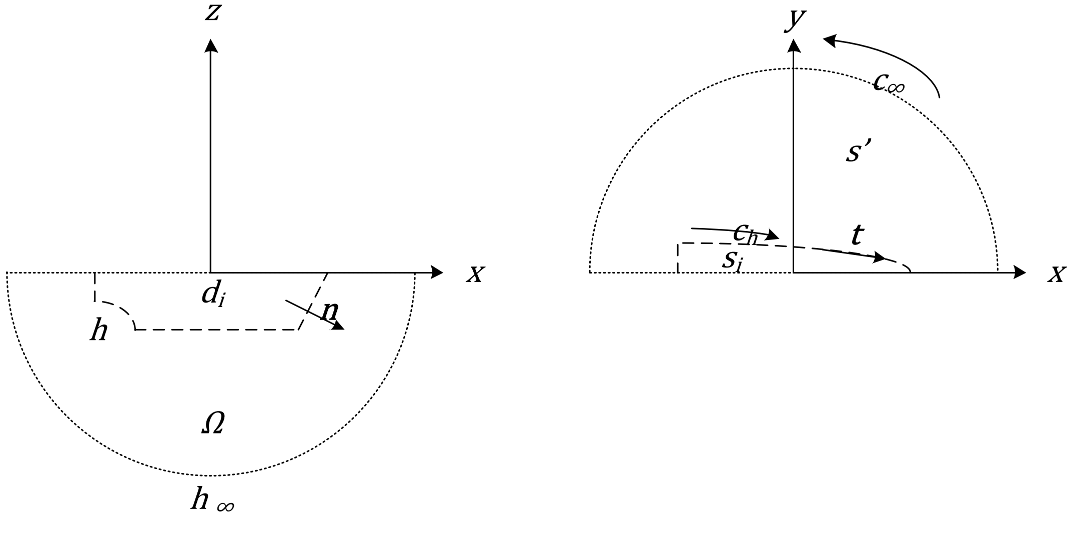

Figure 8 Boundaries of the fluid domain, in the xy-plane only the port side is shown

The perturbed velocity potential ϕ has the following properties:

- $\phi(\boldsymbol{x})$ and all its derivatives exist and are continuous in the fluid domain
- The integral $\iiint_{\Omega} |\phi(\boldsymbol{x})|$ is finite

The potential must satisfy

$$\iiint_{\Omega} \delta(\boldsymbol{a}-\boldsymbol{x})\phi(\boldsymbol{a})\, d\boldsymbol{a} = \phi(\boldsymbol{x}), \tag{3.27}$$

where $\boldsymbol{x} = (x, y, z)$ is the location of the field point and $\boldsymbol{a} = (a, b, c)$ is the location of a source point, where c is strictly negative. The distance between the field point and the source point is described by $(x\text{-}a,\ y\text{-}b,\ z\text{-}c)$.

Requiring Green function, $G(\boldsymbol{x}, \boldsymbol{a})$, to satisfy

$$\nabla^2 G(\boldsymbol{x}, \boldsymbol{a}) = \delta(a-x)\delta(b-y)\delta(c-z) \tag{3.28}$$

gives

$$\iiint_{\Omega} \phi(\boldsymbol{a})\nabla^2 G(\boldsymbol{x}, \boldsymbol{a})\ d\Omega = \iiint_{\Omega} \delta(\boldsymbol{a}-\boldsymbol{x})\ \phi(\boldsymbol{a}) d\Omega = \phi(\boldsymbol{x}). \tag{3.29}$$

Using the relationship

$$\phi\nabla^2 G = \nabla \cdot (\phi\nabla G) - \nabla G \cdot \nabla\phi \tag{3.30}$$

in (3.29) gives

$$\phi(\boldsymbol{x}) = \iiint_{\Omega} (\nabla \cdot (\phi\nabla G) - \nabla G \cdot \nabla\phi)\ d\Omega. \tag{3.31}$$

Applying the divergence theorem (p. 459 Kreyszig, 2006) leads to:

$$\iiint_{\Omega} \nabla \cdot \boldsymbol{F} d\Omega = \iint_{\Sigma} \boldsymbol{F} \cdot \boldsymbol{n} d\Sigma, \tag{3.32}$$

where Σ is the surface boundary enclosing the volume Ω, to the first part of the integral in (3.31) gives

$$\phi(\boldsymbol{x}) = \iint_{\Sigma} \phi\nabla G \cdot \boldsymbol{n} d\Sigma - \iiint_{\Omega} \nabla G \cdot \nabla\phi\ d\Omega \tag{3.33}$$

and

$$\phi(\boldsymbol{x}) = \iint\limits_{\Sigma} \phi \frac{\partial G}{\partial \boldsymbol{n}} d\Sigma - \iiint\limits_{\Omega} \nabla G \cdot \nabla\phi \; d\Omega. \tag{3.34}$$

The following property

$$\nabla G \cdot \nabla\phi = \nabla \cdot (G\nabla\phi) - G\nabla^2\phi, \tag{3.35}$$

is then used in the triple integral and noticing the last term is zero (according to the Laplace equation), (3.33) reduces to

$$\phi(\boldsymbol{x}) = \iint\limits_{\Sigma} \phi \frac{\partial G}{\partial \boldsymbol{n}} d\Sigma - \iiint\limits_{\Omega} \nabla \cdot (G\nabla\phi) \; d\Omega. \tag{3.36}$$

Applying the divergence theorem to the last integral gives

$$\phi(\boldsymbol{x}) = \iint\limits_{\Sigma} \phi \frac{\partial G}{\partial \boldsymbol{n}} d\Sigma - \iint\limits_{\Sigma} G\nabla\phi \cdot \boldsymbol{n} d\Sigma \Rightarrow \phi(\boldsymbol{x}) = \iint\limits_{\Sigma} \left(\phi \frac{\partial G}{\partial \boldsymbol{n}} - G\frac{\partial \phi}{\partial \boldsymbol{n}}\right) d\Sigma. \tag{3.37}$$

The surface Σ can then be partitioned into the hull surface h, the free surface s' and the exterior surface h_∞ according to Figure 9.

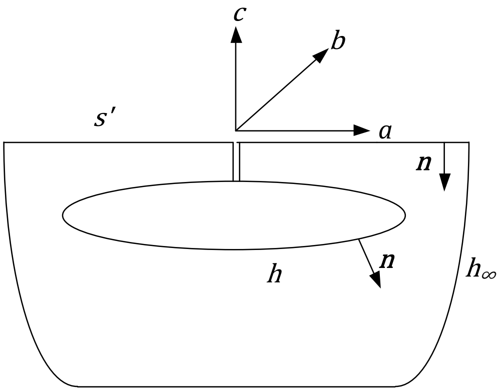

Figure 9 Fluid domain

This yield:

$$\phi(\boldsymbol{x}) = \iint\limits_{h} \left(\phi \frac{\partial G}{\partial \boldsymbol{n}} - G\frac{\partial \phi}{\partial \boldsymbol{n}}\right) d\Sigma + \iint\limits_{s'} \left(\phi \frac{\partial G}{\partial \boldsymbol{n}} - G\frac{\partial \phi}{\partial \boldsymbol{n}}\right) d\Sigma + \iint\limits_{h_\infty} \left(\phi \frac{\partial G}{\partial \boldsymbol{n}} - G\frac{\partial \phi}{\partial \boldsymbol{n}}\right) d\Sigma \tag{3.38}$$

Assuming that the following infinity condition is satisfied, namely:

$$\lim_{R\to\infty}\iint\limits_{\Sigma}\left(\phi\frac{\partial G}{\partial \boldsymbol{n}}-G\frac{\partial \phi}{\partial \boldsymbol{n}}\right)=0, \tag{3.39}$$

(3.38) leads to

$$\phi(\boldsymbol{x})=\iint\limits_{h}\left(\phi\frac{\partial G}{\partial \boldsymbol{n}}-G\frac{\partial \phi}{\partial \boldsymbol{n}}\right)d\Sigma+\iint\limits_{s'}\left(\phi\frac{\partial G}{\partial \boldsymbol{n}}-G\frac{\partial \phi}{\partial \boldsymbol{n}}\right)d\Sigma. \tag{3.40}$$

On the free surface $d\Sigma\equiv dadb$ and $\frac{\partial}{\partial \boldsymbol{n}}=-\frac{\partial}{\partial c}$, since the coordinate direction c is vertical and out of the fluid, whereas the normal $\boldsymbol{n}$ is positive when directed into the fluid, as illustrated by Figure 9, which means that

$$\phi(\boldsymbol{x})=\iint\limits_{h}\left(\phi\frac{\partial G}{\partial \boldsymbol{n}}-G\frac{\partial \phi}{\partial \boldsymbol{n}}\right)d\Sigma-\iint\limits_{s'}\left(\phi\frac{\partial G}{\partial c}-G\frac{\partial \phi}{\partial c}\right)dadb. \tag{3.41}$$

The potential must satisfy the free surface condition (3.26). However the right hand side of (3.41) is integrated with respect to a and b so the surface condition is applied with respect to the source point is

$$\left[\frac{\partial^2}{\partial a^2}-\mu_R'\frac{\partial}{\partial a}+\frac{1}{Fn^2}\frac{\partial}{\partial c}\right]\phi=0. \tag{3.42}$$

Applying Green’s theorem in the plane transforms the surface integral into a contour integral. This can be done either by integration by parts, or, by rewriting the integrand of the second integral as a mathematically equivalent expression by adding a zero (a common mathematical device). In this particular case the equivalent expression will also have a compound term satisfying the composite free-surface boundary condition and a derivative with respect to a. This technique is well understood in hydrodynamic circles, but lacks any definitive reference that recognises the originator of the particular form now introduced.

Choosing the latter approach the expression is rewritten as

$$\begin{aligned}\phi G_c-G\phi_c=\phi\overbrace{(Fn^2G_{aa}+Fn^2\mu_R'G_a+G_c)}^{condition\ on\ G}-G\overbrace{(Fn^2\phi_{aa}-Fn^2\mu_R'\phi_a+\phi_c)}^{free\ surface\ condition}\\+Fn^2(G\phi_a-\phi G_a-\mu_R'\phi G)_a.\end{aligned} \tag{3.43}$$

Expansion of the right hand side of (3.43) will readily establish the equivalence stated.

The steps taken so far are consistent with a conventional approach to the derivation of a required Green function. However, conditions on G have so far been limited to (3.28) and (3.39). (3.43) suggests that it is beneficial if G satisfies:

$$Fn^2 G_{aa} + Fn^2 \mu_R' G_a + G_a = 0. \tag{3.44}$$

Inserting (3.26) and (3.44) into (3.43) gives

$$\phi G_c - G\phi_c = Fn^2 (G\phi_a - \phi G_a - \mu_R \phi G)_a. \tag{3.45}$$

Hence the last integral in (3.41) over the surface becomes

$$\iint\limits_{S'} \left(\phi \frac{\partial G}{\partial c} - G\frac{\partial \phi}{\partial c}\right) dadb = Fn^2 \iint\limits_{S'} \frac{\partial (G\phi_a - \phi G_a - \mu_R' \phi G)}{\partial a} dadb. \tag{3.46}$$

Substituting (3.46) into (3.41) and applying Green's theorem in the plane (p. 439 Kreyszig, 2006)

$$\iint_\Sigma \left(\frac{\partial F_2}{\partial x} - \frac{\partial F_1}{\partial y}\right) dxdy = \oint_C (F_1 dx + F_2 dy) \tag{3.47}$$

leads to:

$$\begin{aligned}\phi(\boldsymbol{x}) = \iint\limits_{h} \left(\phi \frac{\partial G}{\partial \boldsymbol{n}} - G\frac{\partial \phi}{\partial \boldsymbol{n}}\right) d\Sigma - Fn^2 \oint\limits_{c_h} (G\phi_a - \phi G_a - \mu_R' \phi G)\, db \\ - Fn^2 \oint\limits_{c_\infty} (G\phi_a - \phi G_a - \mu_R' \phi G)\, db.\end{aligned} \tag{3.48}$$

The last integral is zero due to the infinity condition of (3.39) and the fact that $\phi \to 0$ as $\boldsymbol{a} \to \infty$. The integral identity in (3.48) describes the relationship between the potential at the field point and source point if the field point is within the fluid domain. A similar relationship can be derived for the case where the field point is on the boundary of the domain, the hull or outside of the domain. The integration over fluid domain in (3.27) is obtained when the field point is in the fluid domain, as the integration domain in (3.27) can be shrunk to a small sphere around the field point see Figure 10. If the field point is on the hull, the enclosing volume around the fluid singularity becomes a hemisphere, as illustrated by Figure 10. If the field point is outside of the fluid domain the Dirac function is identical to zero and thus (3.27) is equal to zero

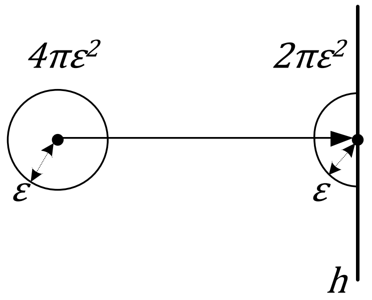

Figure 10 Spherical boundary around the singularity

To combine these three cases the constant C_e is introduced so that (3.48) becomes

$$C_e\phi(\boldsymbol{x}) = \iint\limits_h \left(\phi\frac{\partial G}{\partial \boldsymbol{n}} - G\frac{\partial \phi}{\partial \boldsymbol{n}}\right) d\Sigma - Fn^2 \oint\limits_{c_h} (G\phi_a - \phi G_a - \mu_R'\phi G)\, db \tag{3.49}$$

where

$$C_e = \begin{cases} 1 & & \textit{in the fluid} \\ 1/2 & \textit{if } \boldsymbol{a} \textit{ is} & \textit{on the body} \\ 0 & & \textit{inside the body} \end{cases} \tag{3.50}$$

The most common way to eliminate this discontinuity in the value of C_e is to introduce an inner potential ϕ^i that can be derived in a similar manner, which gives

$$C_i\phi^i(\boldsymbol{x}) = -\iint\limits_h \left(\phi^i\frac{\partial G}{\partial \boldsymbol{n}} - G\frac{\partial \phi^i}{\partial \boldsymbol{n}}\right) d\Sigma + Fn^2 \oint\limits_{c_h} (G\phi_a^i - \phi^i G_a - \mu_R'\phi^i G)\, db \tag{3.51}$$

where

$$C_i = \begin{cases} 0 & & \textit{in the fluid} \\ 1/2 & \textit{if } \boldsymbol{a} \textit{ is} & \textit{on the body} \\ 1 & & \textit{inside the body} \end{cases} \tag{3.52}$$

Adding Equations (3.49) and (3.51) gives

$$\phi(\boldsymbol{x}) = \iint\limits_h (G(\phi_n - \phi_n^i) - (\phi - \phi^i)G_n)\, d\Sigma \tag{3.53}$$

$$-Fn^2 \oint_{c_h} (G(\phi_a - \phi_a^i) - (\phi - \phi^i)G_a - \mu_R'(\phi - \phi^i)G)db$$

where $\phi(\boldsymbol{a})$ corresponds to $\phi(\boldsymbol{a})$ or $\phi^i(\boldsymbol{a})$ for point $\boldsymbol{a}$ outside or inside the hull surface respectively. It is convenient to modify the water line integral (the last integral in equation (3.53)). This is done through a coordinate transformation to a coordinate system based on the unit normal to the hull surface pointing outward into the fluid $\boldsymbol{n} = (n_a, n_b, n_c)$ and a tangent $\boldsymbol{t} = (t_a, t_b, 0)$ (which is the tangent unit vector to the water line c_h). As illustrated in Figure 8. $\boldsymbol{i} = (1,0,0)$ is the unit vector along the x-axis. This gives the following relationship

$$\phi_a = \nabla\phi \cdot \boldsymbol{i} = (\boldsymbol{n}\phi_n + \boldsymbol{t}\phi_\ell + \boldsymbol{n}x\boldsymbol{t}\,\phi_d) \cdot \boldsymbol{i} = n_a\phi_n + t_a\phi_\ell - n_c t_b \phi_d. \tag{3.54}$$

where ϕ_ℓ is the derivative of ϕ in the $\boldsymbol{t}$ direction and ϕ_d is the derivative of ϕ in $\boldsymbol{n}x\boldsymbol{t}$ direction. $\boldsymbol{n}x\boldsymbol{t}$ is a tangential unit vector to the hull pointing downwards. Since $db = t_b d\ell$ in (3.53) can be rewritten as

$$\begin{aligned}\phi(\boldsymbol{x}) = & \iint_h (G(\phi_n - \phi_n^i) - (\phi - \phi^i)G_n)d\Sigma \\ & -Fn^2 \oint_{c_h} \Big(G\left(n_a(\phi_n - \phi_n^i) + t_a(\phi_\ell - \phi_\ell^i) - n_c t_b(\phi_d - \phi_d^i)\right) \\ & - (\phi - \phi^i)G_a - \mu_R'(\phi - \phi^i)G\Big)\, t_b d\ell \end{aligned} \tag{3.55}$$

Defining

$$\textit{Source strength } Q(\boldsymbol{a}) \textit{ as } \phi_n - \phi_n^i \tag{3.56}$$

and

$$\textit{Doublet strength } S(\boldsymbol{a}) \textit{ as } \phi^i - \phi \tag{3.57}$$

yields

$$\phi(\boldsymbol{x}) = \iint_h (GQ + SG_n)\, d\Sigma - Fn^2 \oint_{c_h} (G(n_a - t_a S_\ell + n_c t_b S_d) + SG_a + \mu_R' SG)t_b d\ell \tag{3.58}$$

This is consistent with the expression of Baar (1986). The inner potential can be chosen as $\phi_i = \phi/h$ so that the doublet strength, S, is always zero on h. Then the expression simplifies to

$$\phi(\boldsymbol{x}) = \iint\limits_{h} G(\boldsymbol{x}, \boldsymbol{a}, \mu_R')Q(\boldsymbol{a})\, d\Sigma - Fn^2 \oint\limits_{c_h} G(\boldsymbol{x}, \boldsymbol{a}, \mu_R')n_a Q(\boldsymbol{a}) dy. \qquad (3.59)$$

3.2.2 Pressure on the hull

The pressure on the hull is determined using the non-dimensionalised steady state Bernoulli equation (3.12)

$$\frac{1}{2}|\nabla\Phi|^2 + p + \frac{1}{Fn^2}z + \mu_R'(\Phi + x) = p_0 + \frac{1}{2} + \frac{1}{Fn^2}z. \qquad (3.60)$$

The pressure is determined at a constant depth z and the atmospheric reference pressure p_0 is set to be zero. The steady state Bernoulli equation becomes

$$\frac{1}{2}|\nabla\Phi|^2 + p + \mu_R'(\Phi + x) = \frac{1}{2}. \qquad (3.61)$$

Inserting the perturbed velocity potential according to (3.16) gives

$$\frac{1}{2}|\nabla(-x + \phi)|^2 + p + \mu_R'\phi = \frac{1}{2}. \qquad (3.62)$$

The pressure is then

$$p = \frac{1}{2} - \frac{1}{2}\left[\left(-1 + \frac{\partial\phi}{\partial x}\right)^2 + \left(\frac{\partial\phi}{\partial y}\right)^2 + \left(\frac{\delta\phi}{\delta z}\right)^2\right] - \mu_R'\phi. \qquad (3.63)$$

The pressure is therefore

$$p = \frac{\partial\phi}{\partial x} - \frac{1}{2}\left[\left(\frac{\partial\phi}{\partial x}\right)^2 + \left(\frac{\partial\phi}{\partial y}\right)^2 + \left(\frac{\partial\phi}{\partial z}\right)^2\right] - \mu_R'\phi. \qquad (3.64)$$

The pressure force acting on the hull is determined by integrating over the hull

$$F_p = -\iint\limits_{h} p\boldsymbol{n} dh. \qquad (3.65)$$

3.3 Deriving Green function

The most common way to derive Green function is to apply the free surface condition to G which consists of a fundamental solution and an image source, the function is then integrated over the fluid domain to obtain Green function, see for example Fürth (2011). However a simpler approach is to apply a set of conditions on G and transform it using a Fourier transform to solve in the transformed plane and then transform it back. This technique was described in detail by Wehausen and Laitone (p. 475, 1960). Here the outline by Noblesse (1981) is followed.

The conditions set in chapter 3.2.1 on G are; the second derivative of Green function has to equal to the Dirac function according to (3.27), it is bounded by the condition in (3.45), which is similar to the free surface condition (3.26) but has a different sign on the Rayleigh damping term. Here it should be noted that the condition is applied to the space variable x instead of $\boldsymbol{a}$. Green function must also satisfy the infinity condition (3.39).

A commonly known solution to Poisson's equation is

$$4\pi G = -\frac{1}{r} \; where \; r = |\boldsymbol{x} - \boldsymbol{a}|. \tag{3.66}$$

The fundamental form to Green function can be expressed as

$$4\pi G(\boldsymbol{x}, \boldsymbol{a}, \mu_R') = -\frac{1}{r} + H(\boldsymbol{x}, \boldsymbol{a}, \mu_R'), \tag{3.67}$$

where H is harmonic in the lower half plane.

$$\nabla^2 H = 0 \tag{3.68}$$

Equation (3.67) is inserted into (3.44) to provide the corresponding conditions for H

$$\left[\frac{\partial^2}{\partial x^2} + \mu_R' \frac{\partial}{\partial x} + \frac{1}{Fn^2}\frac{\partial}{\partial z}\right] H = \left[\frac{\partial^2}{\partial x^2} + \mu_R' \frac{\partial}{\partial x} + \frac{1}{Fn^2}\frac{\partial}{\partial z}\right]\frac{1}{r} \; on \; z = 0 \tag{3.69}$$

and the following infinity condition is assumed to be satisfied:

$$H \to 0 \; as \; |\boldsymbol{x} - \boldsymbol{a}| \to \infty \tag{3.70}$$

This problem can be solved using a double Fourier transform. By transformation, the Partial Differential Equation in (3.68) will be reduced to an Ordinary Differential Equation. A double Fourier transform with respect to x and y is used, leaving z untransformed. The transform of $H(x,y)$ is designated $\widehat{H}(\xi,\eta)$ and satisfies:

$$\widehat{H}(\xi,\eta,z,\boldsymbol{a},\mu_R') = \frac{1}{2\pi}\int_{-\infty}^{\infty} dy \int_{-\infty}^{\infty} e^{i(\xi x+\eta y)}\, H(x,y,z,\boldsymbol{a},\mu_R')dx. \tag{3.71}$$

The double Fourier transform for $1/r$ is commonly known as

$$\widehat{\left(\frac{1}{r}\right)} = \left(\frac{1}{\nu}\right) e^{-\nu|z-c|+i(\xi a+\eta b)} \tag{3.72}$$

where

$$\nu = \sqrt{(\xi^2+\eta^2)}. \tag{3.73}$$

Transforming equation (3.68), (3.69) and (3.70) leads to:

$$\frac{d^2\widehat{H}}{dz^2} - \nu^2\widehat{H} = 0 \; in \; z < 0 \tag{3.74}$$

$$\left[-\xi^2 + \mu_R' i\xi + \frac{1}{Fn^2}\frac{d}{dz}\right]\widehat{H} = \frac{1}{\nu}\left[-\xi^2 + \mu_R' i\xi - \frac{\nu}{Fn^2}\right] e^{\nu c+i(\xi a+\eta b)} \; on \; z = 0 \tag{3.75}$$

$$\widehat{H} \to 0 \; as \; z \to -\infty. \tag{3.76}$$

The general solution to equation (3.74) is

$$\widehat{H} = C_1 e^{\nu z} + C_2 e^{-\nu z}. \tag{3.77}$$

From (3.76) it is obvious that $C_2 = 0. C_1$ can be determined from (3.75) as

$$C_1 = \frac{\frac{1}{\nu}\left[-\xi^2 + \mu_R' i\xi - \frac{\nu}{F_n^2}\right]}{\left[-\xi^2 + \mu_R' i\xi + \frac{\nu}{F_n^2}\right]} e^{\nu c+i(\xi a+\eta b)}. \tag{3.78}$$

Substituting (3.78) into (3.77) gives

$$\widehat{H} = \frac{1}{\nu} e^{\nu(z+c)+i(\xi a+\eta b)} - \frac{2\frac{1}{Fn^2}}{\left[\frac{\nu}{Fn^2} - (\xi^2 - \mu_R' i\xi)\right]} e^{\nu(z+c)+i(\xi a+\eta b)}. \tag{3.79}$$

The function $H(\boldsymbol{x},\boldsymbol{a},\mu_R)$can then be found by taking the inverse double Fourier transform of $\widehat{H}$. The double inverse transform is defined as

$$H(\boldsymbol{x},\boldsymbol{a},\mu_R') = \frac{1}{2\pi}\int_{-\infty}^{\infty} d\eta \int_{-\infty}^{\infty} d\xi\, e^{-i(\xi x+\eta y)}\, \widehat{H}(\xi,\eta,z,\boldsymbol{a},\mu_R'). \tag{3.80}$$

Using

$$X = x - a \quad Y = y - b \quad Z = z + c \quad r' = \sqrt{X^2 + Y^2 + Z^2} \quad \boldsymbol{X} = (X, Y, Z) \tag{3.81}$$

where r' is then the distance from the field point to the image source. Then

$$H(\boldsymbol{X}, \mu_R', Fn^2) = \frac{1}{r'} - \frac{1}{\pi}\int_{-\infty}^{\infty} d\eta \int_{-\infty}^{\infty} d\xi \frac{e^{\nu Z - i(\xi X + \eta Y)}}{[\nu - (\xi^2 - \mu_R' i\xi) Fn^2]}. \tag{3.82}$$

Inserting equation (3.82) in equation (3.67) gives

$$4\pi G(\boldsymbol{X}, \mu_R', Fn^2) = -\frac{1}{r} + \frac{1}{r'} - \frac{1}{\pi}\int_{-\infty}^{\infty} d\eta \int_{-\infty}^{\infty} d\xi \frac{e^{\nu z' - i(\xi x' + \eta y')}}{[\nu - (\xi^2 - \mu_R' i\xi) Fn^2]}. \tag{3.83}$$

Equation (3.82) is consistent with the Noblesse expression (1981) (when the fact that a different form of non-dimensionalisation is used has been taken into to account).

3.3.1 Double integral representation

The early work by Havelock (1932) relates to potential flow with Rayleigh damping. His derivation of a Green function for potential flow is most widely used (Baar, 1986). The benefit of Havelock's method is the fact that it includes a viscous damping parameter. However, Noblesse's (1981) derivation of Havelock's expression is easier to follow and hence it is adapted to this problem. The main drawback of Havelock's formula is that when the Green function is separated into near field and far field components, the lower limit on the far field integral makes it impractical to evaluate the function using Bessel functions. Baar recommends to use the Peters (1949) formulation. However Noblesse's (1981) method to derive the Peters formulation is very hard to adapt to include Rayleigh damping.

The Rayleigh damping has another benefit, besides modelling the damping behaviour of the wave profile, it will remove the singularity associated with this Green function. This will allow for the double integral to be evaluated without separating it into two single integrals.

The procedure below follows the approach of Noblesse (1981), but with added Rayleigh damping. The challenge is to simplify and integrate the integral in (3.83). To achieve this, the integral is expressed in cylindrical coordinates. There are two main benefits to using cylindrical coordinates. Firstly, it simplifies the integration of the double integral since only one of the integration limits (the radius) will be infinitely large. Secondly it simplifies the procedure of separating the double integral into near field and far field wave contributions. There is a strong correlation between the computational time and the range of integration (Hearn, 1977), it is therefore very beneficial to limit the integration range.

Initially let

$$\xi = vcos\theta \text{ and } \eta = vsin\theta \tag{3.84}$$

hence Green function (3.83) is then expressed as

$$4\pi G(\boldsymbol{X}, \mu_R') = -\frac{1}{r} + \frac{1}{r'} - \frac{1}{\pi}\int_{-\pi}^{\pi} d\theta \int_0^{\infty} vdv \frac{e^{v[Z-i(Xcos\theta+|Y|sin\theta)]}}{[v-(v^2cos^2\theta - \mu_R' ivcos\theta)Fn^2]}. \tag{3.85}$$

Here it must be noted that the absolute value of Y must be used due to symmetry reason.

Noting that $[v-(v^2cos^2\theta - \mu_R' ivcos\theta)Fn^2] = -v\cos^2\theta[vFn^2 - (sec^2\theta + i\mu_R' sec\theta Fn^2)]$, the function can be expressed as

$$4\pi G(\boldsymbol{X}, \mu_R') = -\frac{1}{r} + \frac{1}{r'} + \frac{1}{\pi}\int_{-\frac{\pi}{2}}^{\frac{3\pi}{2}} I(\theta, \boldsymbol{x}', Fn)sec^2\theta d\theta. \tag{3.86}$$

The integral $I(\theta, \boldsymbol{X}, \mu_R)$ is

$$I(\theta, \boldsymbol{X}, \mu_R', Fn) = \int_0^{\infty} \frac{e^{v[Z-i(Xcos\theta+|Y|sin\theta)]}}{vFn^2 - (sec^2\theta + i\mu_R' sec\theta Fn^2)} dv. \tag{3.87}$$

The integral in equation (3.86) can be separated into two integrals

$$\begin{aligned} 4\pi G(\boldsymbol{X}, \mu_R', Fn) &= -\frac{1}{r} + \frac{1}{r'} \\ &+ \frac{1}{\pi}\left[\int_{-\frac{\pi}{2}}^{\frac{\pi}{2}} I(\theta, \boldsymbol{X}, Fn)sec^2\theta d\theta + \int_{\frac{\pi}{2}}^{\frac{3\pi}{2}} I(\theta, \boldsymbol{X}, Fn)sec^2\theta d\theta\right]. \end{aligned} \tag{3.88}$$

Introducing $\psi = \theta - \pi$ in the last integral leads to

$$\begin{aligned} 4\pi G(\boldsymbol{X}, \mu_R', Fn) &= -\frac{1}{r} + \frac{1}{r'} \\ &+ \frac{1}{\pi}\left[\int_{-\frac{\pi}{2}}^{\frac{\pi}{2}} I(\theta, \boldsymbol{X}, Fn)sec^2\theta d\theta + \int_{-\frac{\pi}{2}}^{\frac{\pi}{2}} \bar{I}(\psi, \boldsymbol{X}, Fn)sec^2\psi d\psi\right], \end{aligned} \tag{3.89}$$

where $\bar{I}$ is the complex conjugate of I. This gives the double integral

$$4\pi G(\boldsymbol{X},\mu_R',Fn) = -\frac{1}{r}+\frac{1}{r'} \\ +\frac{2}{\pi}\int_{-\frac{\pi}{2}}^{\frac{\pi}{2}} Re\int_0^{\infty}\frac{e^{\nu[Z-i(Xcos\theta+|Y|sin\theta)]}}{\nu Fn^2-(sec^2\theta+\mu_R' isec\theta Fn^2)}d\nu sec^2\theta d\theta. \tag{3.90}$$

This means that Green function can be written as

$$4\pi G(\boldsymbol{X},\mu_R',Fn) = -\frac{1}{r}+\frac{1}{r'}+\frac{2}{\pi}Re\int_{-\frac{\pi}{2}}^{\frac{\pi}{2}}\int_0^{\infty}\frac{e^{\nu[Z-i(Xcos\theta+|Y|sin\theta)]}}{\nu Fn^2cos^2\theta-1-\mu_R' icos\theta Fn^2}d\nu d\theta. \tag{3.91}$$

The double integral is normalised with respect to the Froude number so that the convergence of the integrals can be determined independently of the speed. The double integral, D_I can be normalised using the following speed independent normalisation:

$$\rho = \nu Fn^2, \qquad x' = \frac{X}{Fn^2}, \qquad y' = \frac{Y}{Fn^2}, \qquad z' = \frac{Z}{Fn^2}, \qquad \mu_R = \mu_R' Fn^2 \tag{3.92}$$

so that

$$D_I' = \frac{2}{\pi Fn^2}\int_{-\pi/2}^{\pi/2} Re\int_0^{\infty}\frac{e^{\rho[z'-i(x'cos\theta+|y'|sin\theta)]}}{\rho cos^2\theta-(1-\mu_R icos\theta)}d\rho d\theta \equiv \frac{D_I}{Fn^2}. \tag{3.93}$$

The double integral in the Green function above has a major benefit compared to conventional methods. The location of the pole is off the real axis because of the damping as seen in Figure 11.

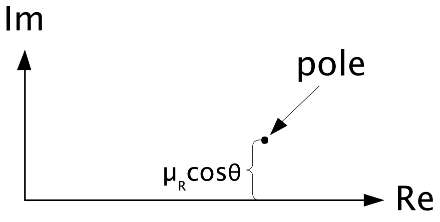

Figure 11 Location of the pole in the complex ρ-plane

A damping influence that is used to describe a physical phenomenon has a mathematical benefit; it enables direct integration without further algebraic manipulation. Conventional Green function definitions will have the pole of the double integral on the real axis, which makes the integration without further algebraic modifications very difficult. Next it is needed to divide the Green function of (3.91) into near field and far field parts, just as undertaken by Noblesse (1981), Baar (1986), Baar and Price (1988a, b) and Newman (1987b), which is a common convenient way to facilitate integration of the double integral when it includes singularities.

However, there are benefits to separating the double integral into two single integrals. Single integrals are much faster to evaluate numerically.

3.3.2 Single integral representation

The double integral in (3.91) can be separated into two single integrals. This is usually done in the case with no Rayleigh damping since the integral would otherwise be singular. However there are benefits in using two single integrals even with Rayleigh damping since single integrals are faster to evaluate numerically than double integrals. Green function will then consist of a source part, and image source part, a near field disturbance and far field disturbance (Baar, 1986, Baar & Price, 1988a, Eggers et al, 1967, Noblesse, 1981). Green function then becomes

$$4\pi G(\boldsymbol{x},\boldsymbol{a},\mu_R',Fn^2) = -\frac{1}{r}+\frac{1}{r'}+\frac{1}{Fn^2}[N(\boldsymbol{x}',\mu_R)+W(\boldsymbol{x}',\mu_R)]. \tag{3.94}$$

The double integral, D_I can be rewritten as:

$$D_I = \frac{2}{\pi}\int_{-\pi/2}^{\pi/2} Re\int_0^\infty \frac{e^{\rho[z\prime - i(x\prime cos\theta + |y\prime| sin\theta)]}}{\rho - \left(\frac{1}{cos^2\theta} - \frac{\mu_R i}{cos\theta}\right)} sec^2\theta d\rho d\theta. \tag{3.95}$$

Firstly a variable substitution is needed

$$T = tan\theta \;\; \Rightarrow \;\; dT = sec^2\theta d\theta \text{ and } sec^2\theta = (1+T^2). \tag{3.96}$$

The double integral in (3.95) is reduced to a single integral by analytically integrating the inner integral. Secondly double integral is rewritten as:

$$D_I = \frac{2}{\pi}\int_{-\infty}^{\infty} ReI'(T,\boldsymbol{x}')dT, \tag{3.97}$$

where

$$I' = \int_0^\infty \frac{e^{\rho\left[z' - i(x' + |y\prime| T)(1+T^2)^{-1/2}\right]}}{\rho - \left((1+T^2) + \mu_R i(1+T^2)^{1/2}\right)} d\rho. \tag{3.98}$$

is the complex integral along the real axis in the complex plane

$$\rho = \rho_r + i\rho_i. \tag{3.99}$$

Instead of integrating along the real axis, a pie shaped contour is used as seen in Figure 12.

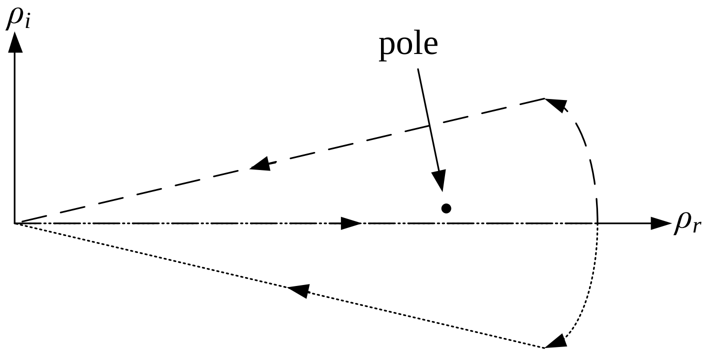

Figure 12 Integration contour in the complex plane

There are two possible integration routes, one with a positive and one with a negative radial line as seen in Figure 12. The integration along a closed contour in the complex plane is zero if the contour does not contain a pole. If the contour contains a pole the integration will yield the residue according to Cauchy residue theorem. This means that the contour integration can yield a residue in the upper half plane but not in the lower half plane. On the circle sector the integrand will go towards zero when ρ goes towards infinity in accordance with Jordan’s Lemma. Since the contour integral is zero in the lower half plane and the integral along the circle sector is zero the integral along the real axis must be equal to the integral along the radial line. There is no sign difference since the integral along the radial line is integrated from ∞ to 0 and the integral along real axis from 0 to ∞. In the upper half plane the pole can be either inside or outside the closed contour depending on the argument of the radial line and the pole as seen Figure 13. If the pole is outside the same argument as for the lower contour will apply and the integration along the real axis becomes the integration along the radial line. If the pole is inside the contour the closed contour integration will yield a residue. The integration along the real axis then becomes the integration along the radial line plus the residue. The integration along the radial line will be the near field disturbance and the residue will be far field disturbance.

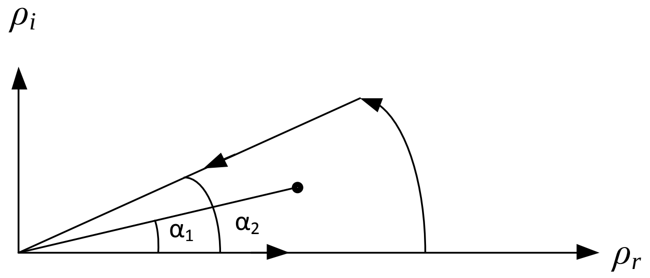

Figure 13 Magnification of the first quadrant with pole

The integral must be bounded which means that

$$Re\left[z' - i(x' + |y'|T)(1 + T^2)^{-1/2}\right]\rho < 0 \quad as\ |\rho| \to \infty. \tag{3.100}$$

The location of the radial line is selected to reflect the requirement

$$Im\left[z' - i(x' + |y'|T)(1 + T^2)^{-1/2}\right]\rho = 0. \tag{3.101}$$

(this is freely chosen but (3.101) will turn out to be a beneficial choice). Inserting (3.99) into (3.101) gives

$$\rho_i = \frac{(x' + |y'|T)}{z'(1 + T^2)^{\frac{1}{2}}}\rho_r. \tag{3.102}$$

Inserting (3.102) into (3.99) gives

$$\rho = \left[1 + \frac{i(x' + |y'|T)}{z'(1 + T^2)^{\frac{1}{2}}}\right]\rho_r. \tag{3.103}$$

Then letting

$$\rho_r = -z'\sigma \tag{3.104}$$

gives

$$\rho = \left[-z' - \frac{i(x' + |y'|T)}{(1 + T^2)^{\frac{1}{2}}}\right]\sigma \ where\ \sigma \geq 0. \tag{3.105}$$

This has the benefit that the location along the radial line can be described using only one variable σ. The exponent in I' (3.98) is rewritten as

$$\left[z' - \frac{i(x' + |y'|T)}{(1 + T^2)^{\frac{1}{2}}}\right]\rho = \left[z' - \frac{i(x' + |y'|T)}{(1 + T^2)^{\frac{1}{2}}}\right]\left[-z' - \frac{i(x' + |y'|T)}{(1 + T^2)^{1/2}}\right]\sigma \tag{3.106}$$

$$= -\left[z'^2 + \frac{(x' + |y'|T)^2}{(1 + T^2)}\right]\sigma.$$

along the radial lines and

$$d\rho = \left[-z' - \frac{i(x' + |y'|T)}{(1 + T^2)^{\frac{1}{2}}}\right] d\sigma. \tag{3.107}$$

The inner integral (3.98) becomes

$$I' = \int_0^\infty \frac{e^{-\left[z'^2 + \frac{(x'+|y'|T)^2}{(1+T^2)}\right]\sigma} \times \left[-z' - \frac{i(x' + |y'|T)}{(1 + T^2)^{\frac{1}{2}}}\right] d\sigma}{\left[-z' - \frac{i(x' + |y'|T)}{(1 + T^2)^{\frac{1}{2}}}\right]\sigma - \left((1 + T^2) + \mu_R i(1 + T^2)^{1/2}\right)}. \tag{3.108}$$

The denominator and numerator are multiplied with

$$\left[z' - i(x' + |y'|T)(1 + T^2)^{-1/2}\right]. \tag{3.109}$$

The inner integral then becomes

$$\begin{aligned} I' = \int_0^\infty & e^{-\left[z'^2 + \frac{(x'+|y'|T)^2}{(1+T^2)}\right]\sigma} \left[z'^2 + \frac{(x' + |y'|T)^2}{(1 + T^2)}\right] \\ & \times \left(-\left[z'^2 + \frac{(x' + |y'|T)}{(1 + T^2)}\right]\sigma \right. \\ & - \left(z'(1 + T^2) + \mu_R(x' + |y'|T)\right. \\ & \left.\left. + i\left[\mu_R z'(1 + T^2)^{1/2} - (x' + |y'|T)(1 + T^2)^{1/2}\right]\right)\right)^{-1} d\sigma \end{aligned} \tag{3.110}$$

This can be simplified using the following substitution:

$$\tau = [z'^2 + (x' + |y'|T)^2/(1 + T^2)]\sigma, \tag{3.111}$$

so that

$$\begin{aligned} I' = \int_0^\infty & -e^{-\tau} \\ & \times \left(-\tau - \left(z'(1 + T^2) - i(x' + |y'|T)(1 + T^2)^{1/2}\right.\right. \\ & \left.\left. + \mu_R i\left[z'(1 + T^2)^{\frac{1}{2}} - i(x' + |y'|T)\right]\right)\right)^{-1} d\tau \end{aligned} \tag{3.112}$$

This is the same as

$$I' = \int_0^\infty \frac{e^{-\tau}}{\tau + \chi} d\tau. \tag{3.113}$$

Here

$$\begin{aligned} \chi &= z'(1 + T^2) + \mu_R(x' + |y'|T) \\ &\quad + i\left[\mu_R z'(1 + T^2)^{1/2} - (x' + |y'|T)(1 + T^2)^{1/2}\right]. \end{aligned} \tag{3.114}$$

This integral has similarities with the exponential integral E_1 (5.1.1 Abramowitz & Stegun, 1964). A new variable substitution is needed to express the integral of this standard form. This will simplify the evaluation of the function. The substitution $\Lambda = \tau + \chi$ is used to get

$$I' = e^\chi \int_\chi^\infty \frac{e^{-\Lambda}}{\Lambda} d\Lambda. \tag{3.115}$$

Using the integral expression (5.1.1 Abramowitz & Stegun, 1964) gives

$$I' = e^\chi E_1(\chi). \tag{3.116}$$

As mentioned before this is the case in the lower half plane. In the upper half plane the residue must be taken into account. The radial lines are described by (3.103), the radial line in the first quadrant has a positive imaginary part and the radial line in the fourth quadrant has a negative imaginary part. The sign of the imaginary part depends on T so that

$$-\infty < T < -\frac{x'}{|y'|} \quad \textit{is the positive radial line} \tag{3.117}$$

and

$$-\frac{x'}{|y'|} < T < \infty \quad \textit{is the negative radial line.} \tag{3.118}$$

However as mentioned before, the pole does not have to be inside the contour in the upper plane. The pole is inside of the contour if $\alpha_2 > \alpha_1$ as seen in Figure 13. The equation for the radial line is

$$\frac{\rho_i}{\rho_r} = \frac{x' + |y'|T}{z'(1 + T^2)^{1/2}} = \alpha_2 \tag{3.119}$$

And the pole, upon reverting to (3.98), is:

$$\rho_0 = (1 + T^2) + \mu_R i(1 + T^2)^{1/2} = \rho_{0r} + i\rho_{0i} \tag{3.120}$$

and

$$\alpha_1 = \frac{\rho_{0i}}{\rho_{0r}} = \frac{\mu_R}{(1+T^2)^{1/2}}. \tag{3.121}$$

The pole is inside the contour if

$$\frac{\rho_i}{\rho_r} > \frac{\rho_{0i}}{\rho_{0r}} \Rightarrow \frac{x' + |y'|T}{z'(1+T^2)^{1/2}} > \frac{\mu_R}{(1+T^2)^{1/2}}. \tag{3.122}$$

This gives

$$x' + |y'|T < \mu_R z' \tag{3.123}$$

since z' is always negative. The pole is therefore inside the contour if

$$T < -\frac{x'}{|y'|} + \underbrace{\frac{\mu_R z'}{|y'|}}_{<0}. \tag{3.124}$$

Since T must satisfy both (3.124) and (3.117), where if (3.124) is satisfied (3.117) must be satisfied as well. The residue for the simple pole with respect of the singular integral in (3.98) is (18.7 (1) Priestley, 2003)

$$Res\big(I' : (1+T^2) + \mu_R i (1+T^2)^{1/2}\big) = 2\pi i e^{\chi}. \tag{3.125}$$

Here the exponent χ is given by (3.114). The residue is included when the pole is inside the contour and is excluded otherwise by using a Heaviside step function. Then (3.116) becomes

$$I' = e^{\chi} E_1(\chi) + H_s\left(-\frac{x'}{|y'|} + \frac{\mu_R z'}{|y'|} - T\right) 2\pi i e^{\chi} \tag{3.126}$$

where H_s is the Heaviside step function. The double integral in (3.97) has then become the single integral

$$D_I = \frac{2}{\pi}\int_{-\infty}^{\infty} Re\left(e^{\chi} E_1(\chi) + H_s\left(-\frac{x'}{|y'|} + \frac{\mu_R z'}{|y'|} - T\right) 2\pi i e^{\chi}\right) dT. \tag{3.127}$$

Now the double integral can be split into two single integrals according to (3.94). The image source term is sometimes included in the near field disturbance.

However, here the near field disturbance is only the single integral over the standard function E_1. The near field and far field disturbance is then

$$N(\boldsymbol{x}', \mu_R) = \frac{2}{\pi} \int_{-\infty}^{\infty} Re\{e^{\chi} E_1(\chi)\} dT \tag{3.128}$$

$$W(\boldsymbol{x}', \mu_R) = \frac{2}{\pi} \int_{-\infty}^{\infty} Re\left(H_s\left(-\frac{x'}{|y'|} + \frac{\mu_R z'}{|y'|} - T \right) 2\pi i e^{\chi} \right) dT. \tag{3.129}$$

The far field or wave like disturbance W can be rewritten using the relationship

$$Reiz = Im\bar{z} \quad since\ Re\big(i(x + iy)\big) = Re(ix - y) = -y \tag{3.130}$$

to give

$$W(\boldsymbol{x}', \mu_R) = 4 \int_{-\infty}^{\infty} Im\left(H_s\left(-\frac{x'}{|y'|} + \frac{\mu_R z'}{|y'|} - T \right) e^{\bar{\chi}} \right) dT. \tag{3.131}$$

Since the step function is zero when $T \geq -\frac{x'}{|y'|} + \frac{\mu_R z'}{|y'|}$, the integral only has to be evaluated up to this limit. So

$$W(\boldsymbol{x}', \mu_R) = 4 \int_{-\infty}^{-\frac{x'}{|y'|} + \frac{\mu_R z'}{|y'|}} Im(e^{\bar{\chi}}) dT. \tag{3.132}$$

Here $\bar{\chi}$ is the complex conjugate of χ.

$$\bar{\chi} = (1 + T^2)z' + \mu_R(x' + |y'|T) + i\left[(x' + |y'|T)(1 + T^2)^{\frac{1}{2}} - \mu_R z'(1 + T^2)^{\frac{1}{2}}\right]. \tag{3.133}$$

The integration limits can be changed using $\tau = -T$ to give

$$W(\boldsymbol{x}', \mu_R) = 4 \int_{\frac{x'}{|y'|} - \frac{\mu_R z'}{|y'|}}^{\infty} Im\left(e^{(1+T^2)z' + \mu_R(x' - |y'|T) + i[(x' - |y'|T) - \mu_R z'](1+T^2)^{\frac{1}{2}}} \right) dT. \tag{3.134}$$

To determine the derivatives it is noted that

$$\frac{\partial W}{\partial x} = \frac{\partial W}{\partial X} = Fn^2 \frac{\partial W}{\partial x'} \ and\ \frac{\partial N}{\partial x} = \frac{\partial N}{\partial X} = Fn^2 \frac{\partial N}{\partial x'}, \tag{3.135}$$

$$\frac{\partial W}{\partial y} = \frac{\partial W}{\partial Y} = Fn^2 \frac{\partial W}{\partial y'} \ and\ \frac{\partial N}{\partial y} = \frac{\partial N}{\partial Y} = Fn^2 \frac{\partial N}{\partial y'}, \tag{3.136}$$

$$\frac{\partial W}{\partial z} = \frac{\partial W}{\partial Z} = Fn^2 \frac{\partial W}{\partial z'} \ and\ \frac{\partial N}{\partial z} = \frac{\partial N}{\partial Z} = Fn^2 \frac{\partial N}{\partial z'}. \tag{3.137}$$

To differentiate under the integral sign Leibniz's rule is used (p. 137 Råde & Westergren, 2004)

$$\frac{d}{dx}\int_{u(x)}^{a} F(x,t)\,dt = \int_{u(x)}^{a} \frac{\partial}{\partial x}F(x,t)dt - F(x,u)\frac{du}{dx}. \tag{3.138}$$

Applying (3.138) to W for $\frac{d}{dx},\frac{d}{dy}$ and $\frac{d}{dz}$ gives

$$\begin{aligned}\frac{\partial W(\boldsymbol{x}',\mu_R)}{\partial \mathrm{x}} &= \frac{4}{Fn^2}\int_{\frac{x'}{|y'|}-\frac{\mu_R z'}{|y'|}}^{\infty} Im\left\{\left[\mu_R + i(1+T^2)^{\frac{1}{2}}\right]\right. \\ &\qquad \left.\times\, e^{(1+T^2)z'+\mu_R(x'-|y'|T)+i[(x'-|y'|T)-\mu_R z'](1+T^2)^{\frac{1}{2}}}\right\} dT\end{aligned} \tag{3.139}$$

$$\begin{aligned}\frac{\partial W(\boldsymbol{x}',\mu_R)}{\partial \mathrm{y}} &= -\frac{4}{Fn^2}sgn(y')\int_{\frac{x'}{|y'|}-\frac{\mu_R z'}{|y'|}}^{\infty} Im\left\{\left[\mu_R T + iT(1+T^2)^{\frac{1}{2}}\right]\right. \\ &\qquad \left.\times\, e^{(1+T^2)z'+\mu_R(x'-|y'|T)+i[(x'-|y'|T)-\mu_R z'](1+T^2)^{\frac{1}{2}}}\right\} dT\end{aligned} \tag{3.140}$$

$$\begin{aligned}\frac{\partial W(\boldsymbol{x}',\mu_R)}{\partial \mathrm{z}} &= \frac{4}{Fn^2}\int_{\frac{x'}{|y'|}-\frac{\mu_R z'}{|y'|}}^{\infty} Im\left\{\left[(1+T^2) - \mu_R i(1+T^2)^{\frac{1}{2}}\right]\right. \\ &\qquad \left.\times\, e^{(1+T^2)z'+\mu_R(x'-|y'|T)+i[(x'-|y'|T)-\mu_R z'](1+T^2)^{\frac{1}{2}}}\right\} dT.\end{aligned} \tag{3.141}$$

Because the last term of (3.138) is zero since $W(\boldsymbol{x}',\mu_R,T)$ becomes $W\left(\boldsymbol{x}',\mu_R,x'/|y'|\text{-}\mu_R z'/|y'|\right)$ and $Im\left\{W\left(\boldsymbol{x}',\mu_R,x'/|y'|\text{-}\mu_R z'/|y'|\right)\right\} = 0$. It is beneficial to express the near field disturbance, N as a function of $\bar{\chi}$ as well. Hence the following relationship is used

$$Re[e^{\chi}E_1(\chi)] = Re\overline{[e^{\chi}E_1(\chi)]} \text{ and } \overline{e^{\chi}E_1(\chi)} = e^{\bar{\chi}}E_1(\bar{\chi}) \quad |arg(\bar{\chi})| < \pi \tag{3.142}$$

so that

$$N(\boldsymbol{x}',\mu_R) = \tfrac{2}{\pi}\textstyle\int_{-\infty}^{\infty} Re\{e^{\bar{\chi}}E_1(\bar{\chi})\}dT, \tag{3.143}$$

where $\bar{\chi}$ is determined according to (3.133).

It is also seen that for the near field disturbance, the absolute value of y' is not needed since for $y' > 0$ it makes no difference and for $y' < 0$ the negative sign can be removed yet again using $\tau = -T$. However it must be remembered that for symmetry reasons (since the lower limit is infinite in the wave like disturbance) the absolute value of y' must be used in the far field disturbance. The expression for the near field disturbance (3.143) and the wave disturbance (3.134) are equal to the expressions for the Havelock formula by Noblesse (1981) if $\mu_R = 0$.

The derivative of the near field disturbance is obtained using the product rule. For the standard function E_1 the derivative is

$$E'_1(\bar{\chi}) = E_0(\bar{\chi}) = -\frac{e^{-\bar{\chi}}}{\bar{\chi}}. \tag{3.144}$$

The derivatives of the near field disturbance (3.143) are

$$\frac{\partial N(\boldsymbol{x}',\mu_R)}{\partial x} = \frac{2}{\pi Fn^2}\int_{-\infty}^{\infty} Re\{[\mu_R + i(1+T^2)^{1/2}]e^{\bar{\chi}}(E_1(\bar{\chi}) - E_0(\bar{\chi}))\}dT \tag{3.145}$$

$$\frac{\partial N(\boldsymbol{x}',\mu_R)}{\partial y} = \frac{2}{\pi Fn^2}\int_{-\infty}^{\infty} Re\{[\mu_R T + iT(1+T^2)^{1/2}]e^{\bar{\chi}}(E_1(\bar{\chi}) - E_0(\bar{\chi}))\}dT \tag{3.146}$$

$$\frac{\partial N(\boldsymbol{x}',\mu_R)}{\partial z} = \frac{2}{\pi Fn^2}\int_{-\infty}^{\infty} Re\{[(1+T^2) - \mu_R i(1+T^2)^{1/2}]e^{\bar{\chi}}(E_1(\bar{\chi}) - E_0(\bar{\chi}))\}dT. \tag{3.147}$$

With the use of (3.144) the derivatives are simplified to

$$\frac{\partial N(\boldsymbol{x}',\mu_R)}{\partial x} = \frac{2}{\pi Fn^2}\int_{-\infty}^{\infty} Re\left\{[\mu_R + i(1+T^2)^{1/2}]\left(e^{\bar{\chi}}E_1(\bar{\chi}) - \frac{1}{\bar{\chi}}\right)\right\}dT \tag{3.148}$$

$$\frac{\partial N(\boldsymbol{x}',\mu_R)}{\partial y} = \frac{2}{\pi Fn^2}\int_{-\infty}^{\infty} Re\left\{[\mu_R T + iT(1+T^2)^{1/2}]\left(e^{\bar{\chi}}E_1(\bar{\chi}) - \frac{1}{\bar{\chi}}\right)\right\}dT \tag{3.149}$$

$$\frac{\partial N(\boldsymbol{x}',\mu_R)}{\partial z} = \frac{2}{\pi Fn^2}\int_{-\infty}^{\infty} Re\left\{[(1+T^2) - \mu_R i(1+T^2)^{1/2}]\left(e^{\bar{\chi}}E_1(\bar{\chi}) - \frac{1}{\bar{\chi}}\right)\right\}dT. \tag{3.150}$$

4 Numerical theory and implementations

Green function and its derivatives need to be evaluated for a large number of field- source point relationships. Thus, the formulation of an efficient algorithm for numerical calculation is of utmost importance for practical use of the calculation scheme.

To apply the method discussed in the previous chapter a discretisation of the body is needed. The aim is to modify the continuous integral equation (3.59) into a discrete form.

4.1 Discretisation

The disturbance potential of the flow about a moving ship is expressed in (3.59) in terms of a continuous distribution of Kelvin wave sources over the mean hull surface. Two types of discretisations are used; thin ship approximation and a panel method. Thin ship theory is only applicable to thin and slender ships but is much less complex and requires less computational time. Thin ship theory will approximate a 3D body as a 2D body and therefore only use 2D panels. A panel method using 3D panels can be used on both slender and fuller bodies but it is computationally much more demanding. Schematic pictures of a 2D and 3D panel are illustrated in Figure 14.

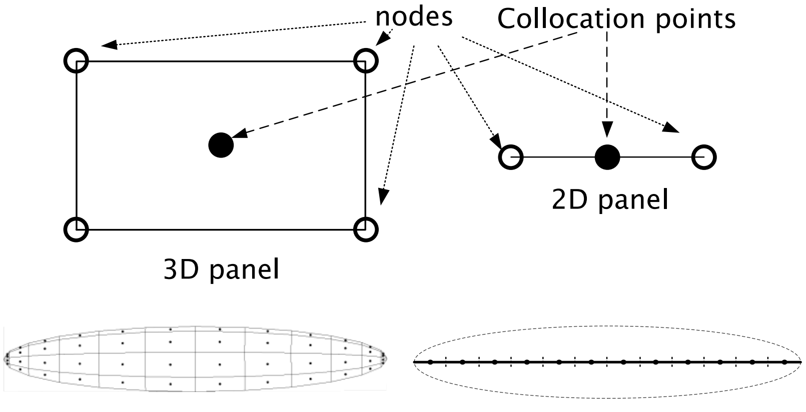

Figure 14 3D and 2D panel

4.1.1 Thin ship approximation

Michell (1898) developed thin ship theory. The theory is powerful since the manner in which the wave profile along the hull, the pressure on the hull, the hydrodynamic lift and pitch moment, sinkage, trim, drag and the wave pattern can be determined using only sources distributed on the centre plane, meaning that a 3D problem essentially becomes a 2D problem (Noblesse et al, 2009). The local source strength is proportional to the change of geometry of the hull in the x direction (Faltinsen, 2006). Michell's theory is exceptionally simple and robust when it comes to evaluating steady flow around a ship and it is the most widely used theory for determining wave resistance (Noblesse et al, 2009). Thin ship theory places the sources on the centre plane only so that equation (3.38) becomes

$$\phi(\boldsymbol{x}) = -\iint_{centre\ plane} G(\boldsymbol{x}, \boldsymbol{a}, \mu_R') \frac{\partial \phi}{\partial \boldsymbol{n}} d\Sigma. \tag{4.1}$$

Since there is no inner domain, the hull is just its centre plane, the source strength becomes

$$Q(a, b) = \frac{\partial \phi}{\partial \boldsymbol{n}}. \tag{4.2}$$

It is assumed that when the hull is divided into panels, Green function is relatively constant over each 2D panel (the difference between the node point and control point for each panel is very small) so that

$$\phi(\boldsymbol{x}) = -\sum_{panel} G(\boldsymbol{x}, \boldsymbol{a}, \mu_R') \iint_{panel} Q(a, b) da db. \tag{4.3}$$

The panels are a discretisation of the centre plane. The methodology outline presented next follows the approach of Faltinsen (p. 110, 2006). Hull integrity means there will be no flow through the hull, as stated in (3.1). The derivative along the normal vector can be expressed as

$$\frac{\partial}{\partial \boldsymbol{n}} = n_a \frac{\partial}{\partial a} + n_b \frac{\partial}{\partial b} + n_c \frac{\partial}{\partial c}. \tag{4.4}$$

The Neumann boundary condition in (3.1) combined with the defined perturbation potential of (3.16) leads to

$$0 = \frac{\partial \Phi}{\partial \boldsymbol{n}} = -n_a + n_a \frac{\partial \phi}{\partial a} + n_b \frac{\partial \phi}{\partial b} + n_c \frac{\partial \phi}{\partial c} \qquad on\ the\ hull\ surface. \tag{4.5}$$

The unit normal $\boldsymbol{n} = (n_a, n_b, n_c)$ is positive into the fluid domain. (4.5) can be simplified using the slenderness of the ship geometry. In particular one ship dimension (hull length) is distinctly larger compared to the draught of the ship and hence, see Figure 15 and Figure 16, follows that $n_a << n_b$ and $n_a << n_c$.

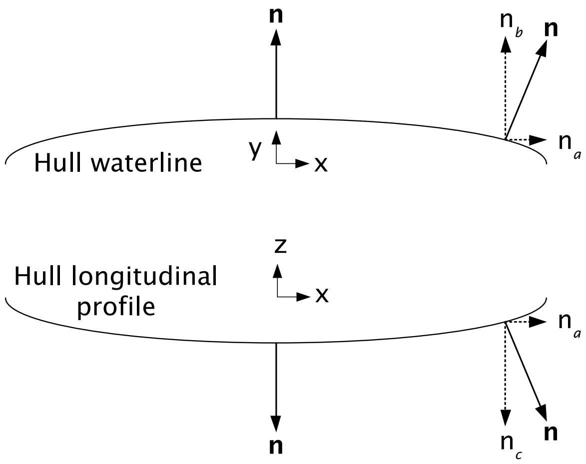

Figure 15 Normal to hull surface in horizontal xy- and vertical xz-plane

The ship is also assumed to be thin, so that $n_c << n_b$ and that $n_b = \pm 1$, for positive and negative y values respectively, as illustrated in Figure 16.

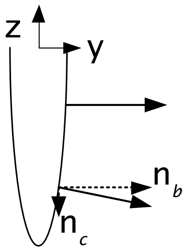

Figure 16 Transverse section of hull showing the normal in yz-plane

The unit normal to the hull surface is therefore

$$\boldsymbol{n} = \left(\frac{\partial y_s}{\partial a}, \pm 1, \frac{\partial y_s}{\partial c}\right), \tag{4.6}$$

where both $\partial y_s/\partial a$ and $\partial y_s/\partial c$ are very small. Here y_s is the expression for the hull shape in the y direction.

The dominant terms within (4.5) are therefore

$$n_a = \pm \frac{\partial \phi}{\partial b}, \tag{4.7}$$

since $\nabla\phi$ is small. The sign of n_a depends on what side of the centre plane one is considering. This means that the flow outwards from the ship in the horizontal direction is:

$$\frac{\partial \phi}{\partial b} = \mp \frac{\partial y_s}{\partial a} \tag{4.8}$$

on the 2 sides of the hull. Fluid appears to be either pushed out or sucked in depending on the sign of $\partial y_s/\partial a$. Because $\partial y_s/\partial a$ is positive in the bow region fluid is pushed out there and the opposite occurs in the stern region. The source strength is determined depending on the mass flux. The source strength of a single source is equal to a continuous source distribution with source density $Q(a,c)$ flowing through an area $dadc$. A sphere with radius ε so small that it only includes one source is illustrated in Figure 17. The mass flux through the sphere is the same in any direction.

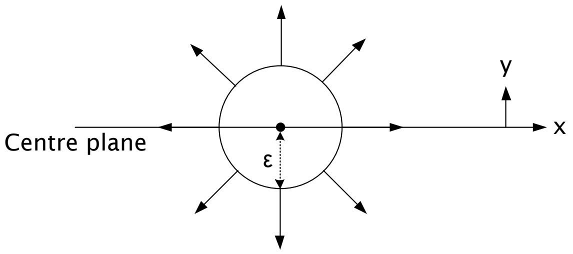

Figure 17 The mass flux from one source on the centre plane

This means that the mass flux through an area $dadc$ must be

$$Q(a,b) = 2\frac{\partial y_s}{\partial a} = 2\int_{x_0}^{x_1} da \int_{z_1}^{z_0} \frac{\partial y_m}{\partial a} dc, \tag{4.9}$$

for further details see Faltinsen (p. 111, 2006). Hence the velocity potential of (4.3) becomes

$$\phi(\boldsymbol{x}) = G(\boldsymbol{x}, \boldsymbol{a}, \mu_R')2\int_{x_0}^{x_1} da \int_{z_1}^{z_0} \frac{\partial y_s}{\partial a} dc, \tag{4.10}$$

where x_0 is the forward edge of each panel, x_1 the aft panel edge, z_0 the panel edge closest to the free surface and z_1 the deepest panel edge.

4.1.2 Panel method

The method described in the previous section is inadequate for fuller shapes, which represents the majority of ships. In the panel method the discretisation is done by describing the object as a series of panels. The mean hull surface h is divided into triangular or quadrilaterals panels, these are identified by their area Δh_j and the collocation points $\boldsymbol{x}_i$. For simplicity an ordinary panel method is used, which means that each panel has no curvature. The panel with the collocation point is numbered i (field panel) and the panel with the source point j (source panel). Each panel has the collocation point at the centroid. The potential at the collocation point is determined by integrating the source strength and Green function over the hull according to (3.59), for a submerged object the surface line integral can be neglected so (3.59) becomes

$$\phi(\boldsymbol{x}_i) = \iint_h G(\boldsymbol{x}, \boldsymbol{a}, \mu_R) Q(\boldsymbol{a})\, d\Sigma. \tag{4.11}$$

To determine the unknown source strengths, Q, the boundary condition (3.1) is used, inserting the perturbed potential (3.16) in (3.1) gives

$$\frac{\partial \phi}{\partial \boldsymbol{n}} = n_x \; on\ the\ body. \tag{4.12}$$

Applying the boundary condition in (4.12) to the potential in (4.11) gives

$$n_x = \iint_h \frac{\partial G(\boldsymbol{x}, \boldsymbol{a}, \mu_R)}{\partial \boldsymbol{n}} Q(\boldsymbol{a})\, d\Sigma, \tag{4.13}$$

where (4.13) is satisfied at the centroid on each panel. A source is placed at each collocation point. The integral identities in (4.13) can be written in discretised form

$$\sum_{j=1}^{N} I_{ij} Q(\boldsymbol{a}_j) = n_x(\boldsymbol{x}_i) \tag{4.14}$$

where

$$I_{ij} = \iint_{\Delta h_j} \frac{\partial G(\boldsymbol{x}_i, \boldsymbol{a}_j, \mu_R)}{\partial \boldsymbol{n}}\, d\Sigma. \tag{4.15}$$

I_{ij} is the influence matrix that describes how the sources influence the flow in the normal direction to the panels. Q is obtained by solving (4.14). The derivative with respect to the normal is

$$\frac{\partial G(\boldsymbol{x}_i, \boldsymbol{a}_j, \mu_R)}{\partial \boldsymbol{n}} = \nabla G \cdot \boldsymbol{n} \tag{4.16}$$

where

$$\nabla 4\pi G = -\nabla\frac{1}{r} + \nabla\frac{1}{r'} + \frac{1}{Fn^2}[\nabla N + \nabla W] \tag{4.17}$$

and

$$\nabla\frac{1}{r} = \left(\frac{a-x}{r^3}, \frac{b-y}{r^3}, \frac{c-z}{r^3}\right) \tag{4.18}$$

$$\nabla\frac{1}{r'} = \left(\frac{a-x}{r'^3}, \frac{b-y}{r'^3}, \frac{-z-c}{r'^3}\right) \tag{4.19}$$

and the derivative of the far field and near field disturbance is calculated according to (3.139) to (3.141) and (3.148) to (3.150) respectively. The first terms in the Green function $1/r$ and $1/r'$ are integrated analytically over the panel according to Price and Tan (1987). To determine the pressure in (3.65) ϕ is determined according to (4.11) and $\nabla\phi$ is calculated by differentiating (4.11)

$$\nabla\phi(\boldsymbol{x}_i) = \iint_h \nabla G(\boldsymbol{x}, \boldsymbol{a}, \mu_R) Q(\boldsymbol{a})\, d\Sigma, \tag{4.20}$$

and the discrete form is

$$\nabla\phi(\boldsymbol{x}_i) = \sum_{j=1}^{N} J_{ij} Q(\boldsymbol{a}_j), \tag{4.21}$$

where

$$J_{ij} = \iint_{\Delta h_j} \nabla G(\boldsymbol{x}_i, \boldsymbol{a}_j, \mu_R)\, d\Sigma \tag{4.22}$$

and ∇G is obtained from (4.17).

It is problematic to evaluate the Green function when the source point and the collocation point are on the same panel. Since $1/r$ and $1/r'$ are integrated analytically the problems associated with numerical integration of the singularities are avoided. However, the single integrals cannot be evaluated numerically at $x' = y' = 0$ because of the assumption made when integration is along the radial line instead of along the positive axis (see (3.117) and (3.118)). There are two possible approaches to generating a solution, either rework the derivation of the single integrals for the case when $x' = y' = 0$ to get special case single integrals, or, when the collocation point is on the same panel, four one point Gaussian quadrature are adopted as shown in Figure 18 to evaluate the contribution of the two single integrals.

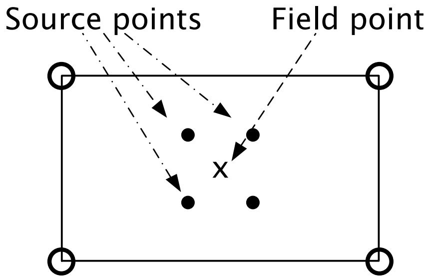

Figure 18 Evaluation points for the single integrals

4.2 Behaviour and limitations of the double integral

To numerically evaluate the double integral of (3.91) and its derivatives is problematic, especially for the case with no damping. The pole will then be located on the real axis. The closer to the real axis the pole is, the more challenging the integral will be to evaluate.

Firstly the behaviour of the integrand is investigated. To capture the oscillatory behaviour the integrand must be evaluated close to where the denominator is zero (see Figure 21), however it cannot be evaluated when the denominator is zero. The maximum computed value of the integrand depends on the number of sections; a finer discretisation gives higher values of the integrand, because it is evaluated closer to the pole. The double integral cannot be evaluated if the denominator is zero which can happen only when $\mu_R' = 0$. Here the sections in the one point Gaussian quadrature are spaced so that the integrand is not evaluated at $\rho cos^2\theta = 1$ when $\mu_R' = 0$.

To illustrate the behaviour of the integrand, values of $\boldsymbol{x}'$ are selected based on the example of a crude ellipsoid discretisation provided in Figure 19. Typical distances between field and source points are shown in Table 2. The distances in Table 2 are used to show the behaviour of the integrand. For the convergence study distances are normalised with $Fn^2 = 1$.

Table 2 Typical distances between field and source points

Panels	x'	y'	z'
red	0	0.0075	-0.5221
purple	-0.9773	0	-0.4934
green	0	0	-0.5040
cyan	-0.9773	0	-0.5040
yellow	-1.1287	0.0427	-0.4613

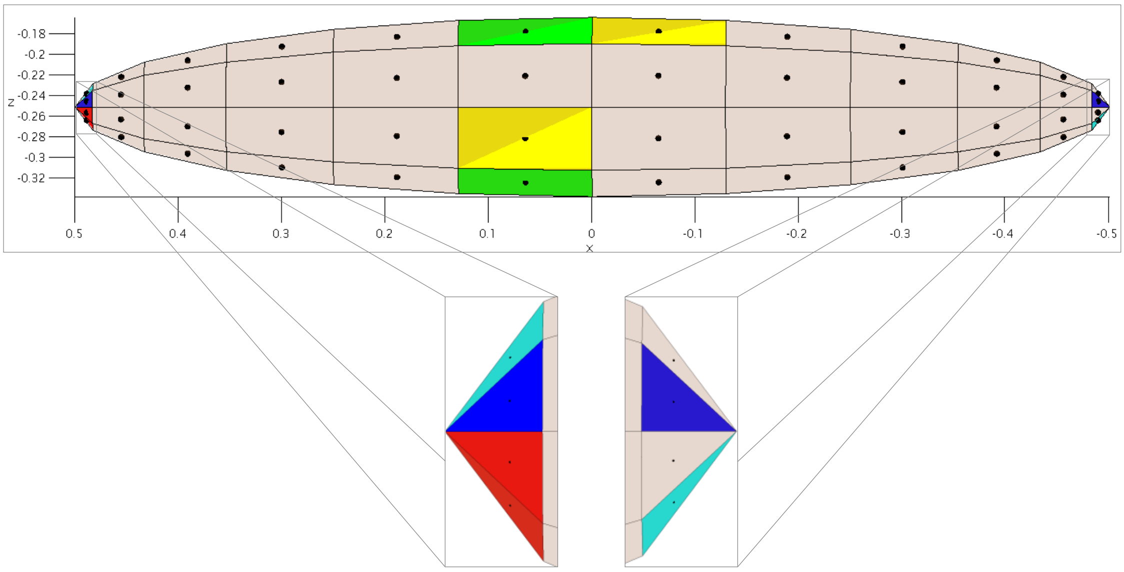

Figure 19 Crude ellipsoid translated with location equal to -0.252 in z-direction

The integrand behaves similarly for all values x', y' but it decays more slowly if z' is small. The integrand will approach zero as ρ increases, the location of areas where the values of the integrand are greater than 0.1% of the absolute maximum value of the integrand is shown in Figure 20.

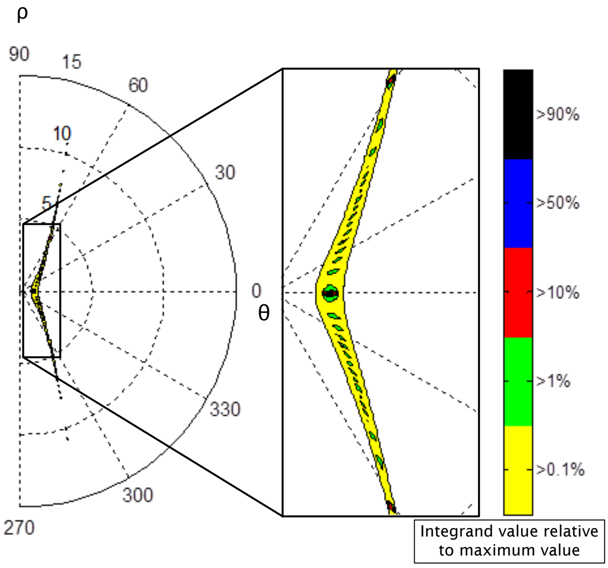

Figure 20 Spread of values between 0.1-100% of the maximum function value **x'**= (-0.1287, 0.0427, -0.4613)

The values of ρ and θ, where the denominator in (3.93) is zero i.e. $\rho cos^2\theta - (1 - \mu_R icos\theta)$, is seen in Figure 21.

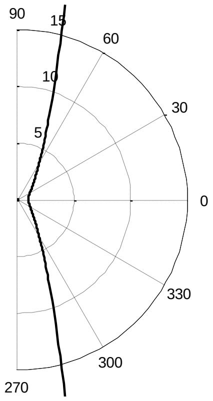

Figure 21 Values of ρ and θ corresponding to a zero denominator

The real part of the numerator of the integrand can be split into two functions

$$D_1 = e^{\rho z'} \tag{4.23}$$

$$D_2 = cos\left(x'cos(\theta) + |y'|sin(\theta)\right), \tag{4.24}$$

which are shown in Figure 22.

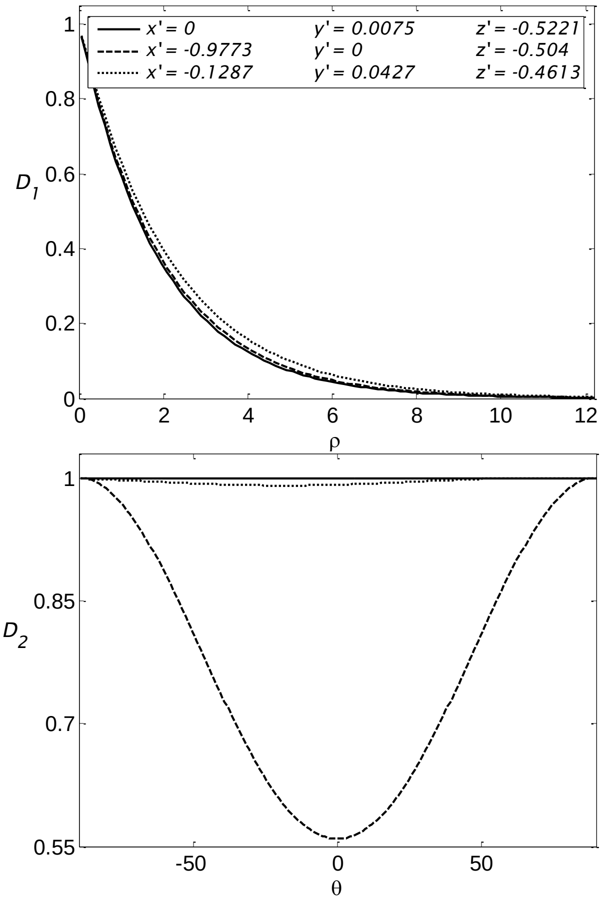

Figure 22 Functions D_1 and D_2

From Figure 22 it is clear that the numerator of (3.93) is small when D_1 is small given that $\mu_R = 0$. D_1 is shown for different values of z' in Figure 23.

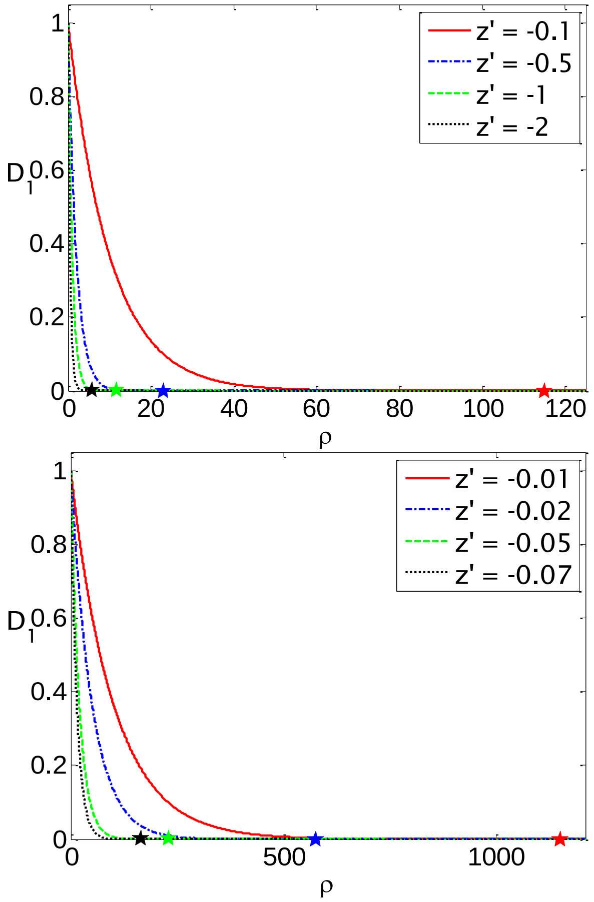

Figure 23 Function D_1 for different values of z'

The marked points in Figure 23 correspond to where the value of D_1 becomes less than 10^{-5}, the star marked points are tabulated in Table 3.

Table 3 Values of ρ when (4.23) is less than 10^{-5} with a discretisation of $d\rho = 0.1$

$z' \leq$	$\rho \geq$
-0.01	1151.3
-0.02	575.7
-0.05	230.3
-0.07	164.5
-0.1	115.2
-0.5	23.1
-1	11.6
-2	5.8

A larger ρ_{max} is required when the submerged body is approaching the free surface, as seen in Figure 23 and Table 3. It is necessary that $|z'| \geq 0.01$ $\rho_{max} \geq$

1150 for the integrand to be less than 10^{-5}. This means that the minimum distance between the centroid of the top panel and the surface is 0.005. Since z' is normalised with Fn^2 this submersion corresponds to between $1.28 \cdot 10^{-4} L$ and $1.352 \cdot 10^{-3} L$ for Froude numbers ranging from 0.16 to 0.52.

Based on Table 3, three typical values of ρ_{max} are defined for the double integral as seen in Table 4.

Table 4 ρ_{max} for far field disturbance

$\lvert z' \rvert \geq$	ρ_{max}
0.5	23
0.05	230
0.01	1150

The error is determined by setting n_θ to 300 and $n_\rho = 125\rho_{max}$ and then doubling ρ_{max} to determine the change in $\partial D_I/\partial x$ and D_I. n_θ is the number of sections in the one point Gaussian quadrature for θ and n_ρ for ρ. This process is illustrated in Figure 24.

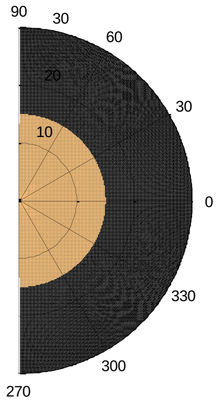

Figure 24 ρ_{max} is doubled from the yellow to include black area as well to determine the error

The maximum difference for $\frac{\partial D_I}{\partial x}$ is 0.21% when ρ_{max} is doubled for the crude ellipsoid discretisation in Figure 19. For D_I the maximum difference is $9 \cdot 10^{-5}$ % when ρ_{max} is doubled.

4.2.1 Limitations of the double integral

The numbers of summation steps in the one point Gaussian quadrature, n_ρ and n_θ need to be large enough so that the integral converges. However, the computational time will increase with increasing n_ρ and n_θ. It is clear from Figure 20 that it would be beneficial to space the evaluation points in the one point

Gaussian quadrature more densely around the integration area where the denominator is close to zero, which is showed in Figure 21, but without evaluation of the function at the pole itself.

The main problem with the convergence of the double integral for zero damping is the singular behaviour of the integrand. However, a finer discretisation does not always lead to evaluation points closer to the pole as seen in Figure 25. This limits the possibility to evaluate the double integral using a uniform discretisation.

A single integral approach is favoured from a numerical efficiency point of view.

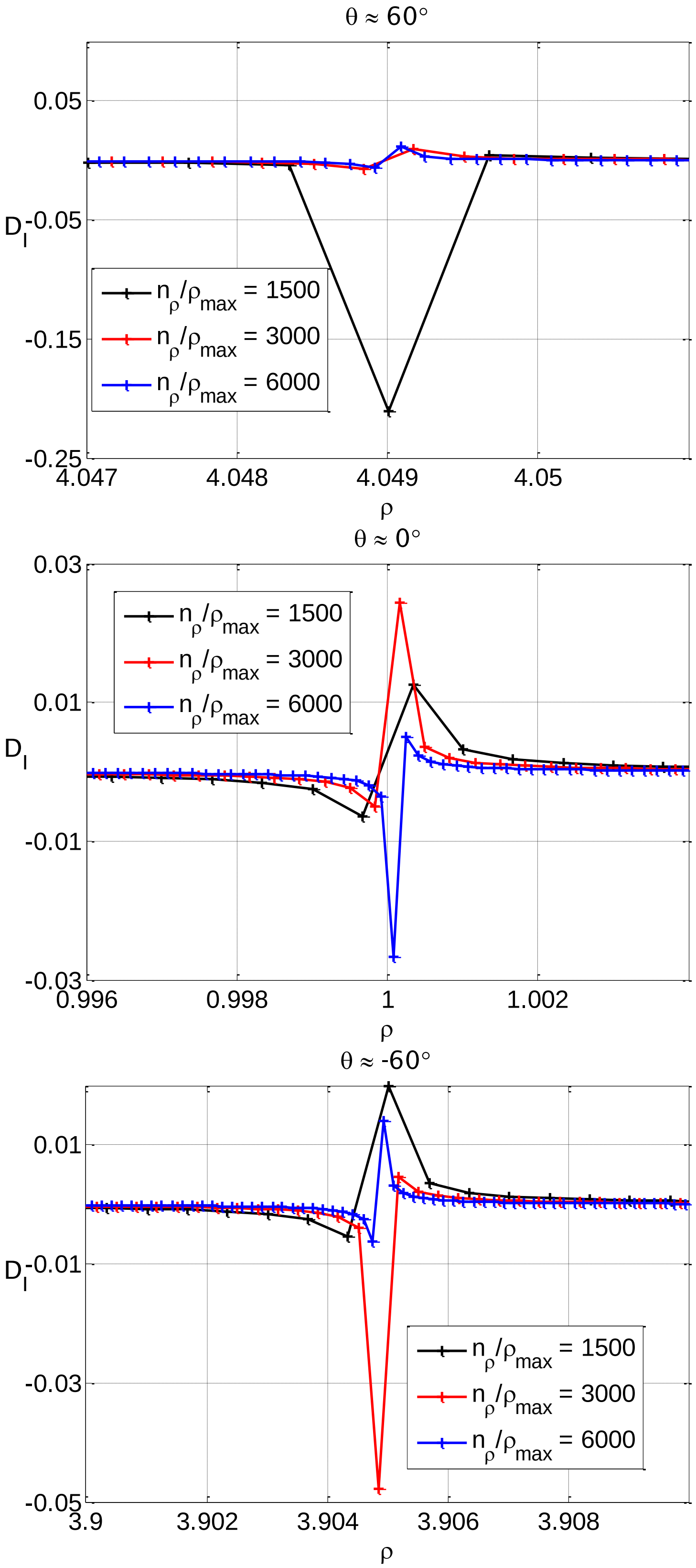

Figure 25 D_l for different spacing of ρ

4.3 Evaluation of the single integrals

No experimental validation of a numerical method can be convincing however good it is if consistency and the accuracy of the numerical method have not been established independently.

To numerically evaluate the single integrals in (3.134) and (3.143) and their respective derivatives, the infinite integral limit is replaced with a finite limit T_{max}. The integral is divided into n_T sections and the contribution from each section is evaluated using a one point Gaussian quadrature. This means that the far field integral is divided from $x'/|y'| - \mu_R z'/|y'|$ to T_{max} into n_T sections that are calculated independently. The near field integral is divided into $2n_T$ sections from $-T_{max}$ to T_{max}.

The behaviour of the integrands are examined to determine the convergence of the single integrals. The closer to the real axis the pole is, the more difficult the integrand will behave. Therefore the case when μ_R is zero is used to determine the convergence. All other values of μ_R will yield a more regular integrand. The solution must converge both for small and large $\boldsymbol{x}'$. Smaller values of $\boldsymbol{x}'$ such as when the source point is close to the field point, are used to calculate the pressure on the hull and large values of $\boldsymbol{x}'$ are used to determine the wave pattern.

Both the far field and near field integrands and their derivatives approach zero as $|T| \to \infty$. It is important to determine a suitable T_{max} so that the integrand is small enough that further summations would not change the result. This is determined by not allowing the value of the integral to change more than 0.5% if T_{max} is doubled.

The number of summation steps n_T will ultimately determine the speed of the calculation. However, this is linked with the value of T_{max} since a larger n_T is required for larger T_{max} in order to keep the same resolution as shown in Figure 26.

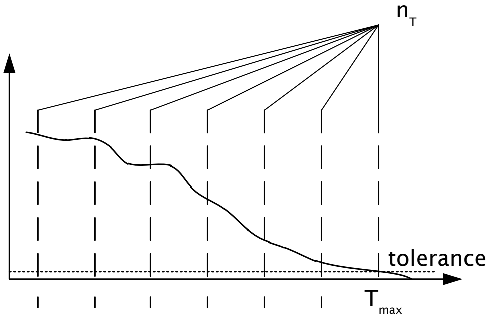

Figure 26 T_{max} and n_T

4.3.1 Convergence of the far field integral

The far field integral in (3.134) with $\mu_R = 0$ is

$$W(\boldsymbol{x}') = 4\int_{\frac{x'}{|y'|}}^{\infty} Im\left(e^{(1+T^2)z'+i[(x'-|y'|T)](1+T^2)^{\frac{1}{2}}}\right) dT. \tag{4.25}$$

Taking the imaginary part gives

$$W(\boldsymbol{x}') = 4\int_{\frac{x'}{|y'|}}^{\infty} e^{(1+T^2)z'} sin\left([(x'-|y'|T)](1+T^2)^{\frac{1}{2}}\right) dT. \tag{4.26}$$

The far field integrand can be split into two functions

$$W_{Int} = e^{(1+T^2)z'} sin\left([(x'-|y'|T)](1+T^2)^{\frac{1}{2}}\right) = W_1 \cdot W_2 \tag{4.27}$$

here

$$W_1 = e^{(1+T^2)z'} \tag{4.28}$$

$$W_2 = sin\left([(x'-|y'|T)](1+T^2)^{\frac{1}{2}}\right). \tag{4.29}$$

For surface piercing bodies $z' \leq 0$, but for submerged bodies $z' < 0$. T is the integration variable and $x'/|y'| < T < T_{max}$.The exponent of W_1 is always negative since $z' < 0$. W_1 is approaching zero when the absolute value of T is increasing. W_2 is an oscillating function and $-1 \leq W_2 \leq 1$. Figure 27 shows W_{Int}, W_1 and W_2 for the values of $\boldsymbol{x}'$ for the red, green and yellow panels in Figure 19. The integral is zero when $y' = 0$ and $x' \neq 0$, since the lower limit becomes positively infinite, and hence the upper and lower limits of the integral are equal. When the exponential part of the integrand of W_1 has reached the tolerance level the total integrand W_I will also be below the tolerance level since $|W_2| \leq 1$. The maximum value of the near field and far field combined is less than 10. Therefore it is a reasonable assumption that when the value of W_1 is $\leq 10^{-5}$

further summation is not necessary when computing the value of the far field integral and its derivatives.

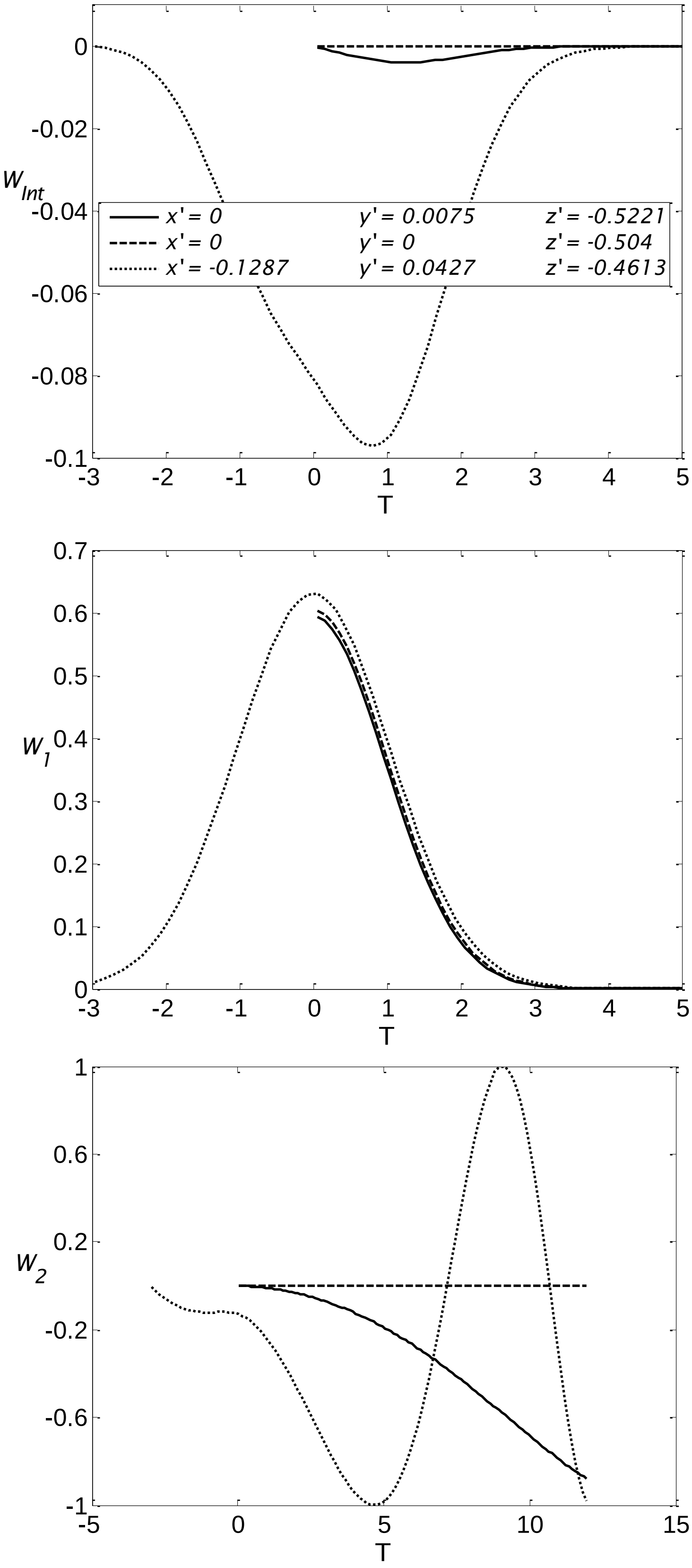

Figure 27 Integrand W_{Int}, integrand W_1 and integrand W_2

W_1 is shown for different values of z' in Figure 28. It is clear that the decay is fast. T_{max} depends on the value of z', $W_1(z',T)$ and $W_2(x',y',T)$.

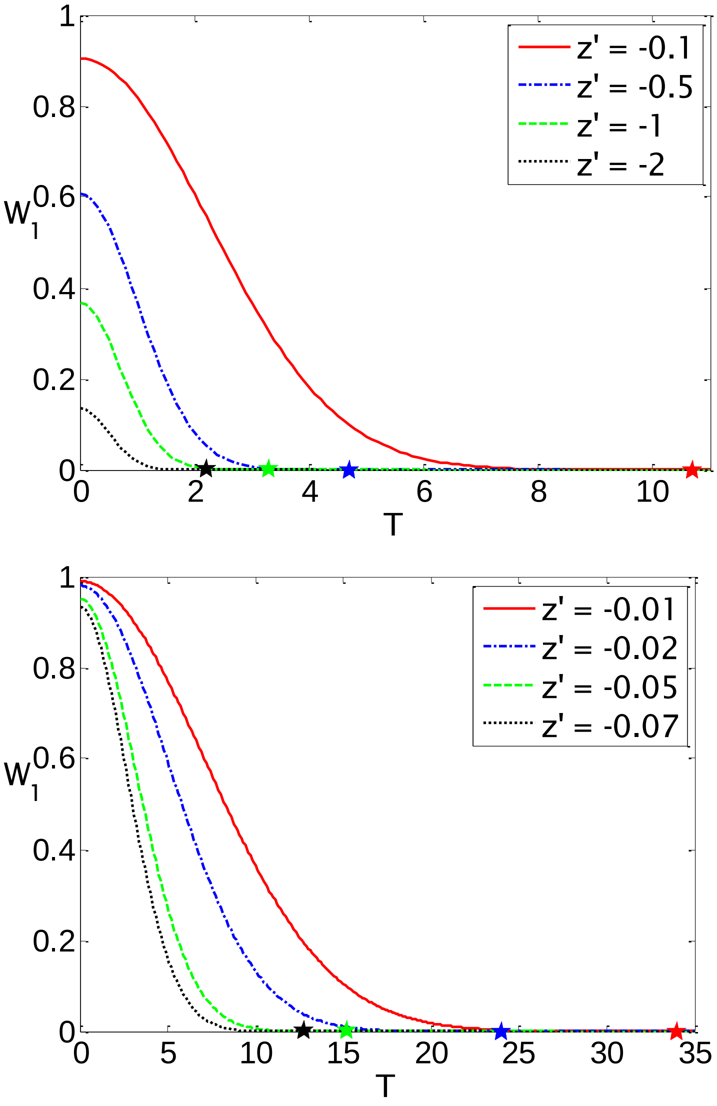

Figure 28 The function W_1 for different values of z'

The marked points in Figure 28 correspond to where the value of W_1 becomes less than 10^{-5}, the star marked points are tabulated in Table 5.

Table 5 Values of T when (4.28) is less than 10^{-5} with a discretisation of $dT = 0.1$

$z' \geq$	T
-0.01	34
-0.02	24
-0.05	15.2
-0.07	12.8
-0.1	10.7
-0.5	4.7
-1	3.3
-2	2.2

A larger T_{max} is required when the submerged body is approaching the free surface as seen in Figure 28 and Table 5. Convergence for $|z'| \geq 0.01$ is established at $T_{max} = 34$. This means that the minimum distance between the centroid of the top panel and the surface is 0.005. Since z' is normalised with the Froude number squared, this submersion is between $1.28 \cdot 10^{-4} L$ and $1.352 \cdot 10^{-3} L$ for Froude numbers ranging from 0.16 to 0.52.

Based on Table 5, 3 typical values of T_{max} are defined for the far field disturbance as presented in Table 6.

Table 6 T_{max} for far field disturbance

$\|z'\| \geq$	T_{max}
0.5	5
0.05	15
0.01	35

The error is determined by setting n_T to $300T_{max}$ and then doubling T_{max} to determine the change in W and its derivatives. For the submerged ellipsoid, illustrated in Figure 19, the maximum difference for W and $\partial W/\partial x$ does not exceed1.47%. In evaluating the integrals of these quantities any section that provides a contribution that is less than 10^{-4} are excluded.

4.3.1.1 n_T *for* W *and its derivative in* x*-direction*

The pressure is calculated according to (3.64) the leading terms are the far field and near field and its derivative in x-direction. The number of summation steps in the one point Gaussian quadrature, n_T needs to be large enough so that the integral converges. The computational time will increase with increasing n_T.

A percentage difference is used to determine the error. The percentage error is determined with $n_T = 10000T_{max}$ as a reference solution. This is done since no "true" value is available for comparison. The percentage error is seen in Table 7. It is clear that $n_T = 10T_{max}$ is sufficient to determine $\partial W/\partial x$ to within a tolerance of 1% of the reference value.

Table 7 Percentage difference depending n_T

$\frac{n_T}{T_{max}}$	$\% \frac{\partial W}{\partial x}$	$\% W$
5	1.6543	1.5763
10	0.4169	0.3968
15	0.1858	0.1769
20	0.1045	0.0994
50	0.0171	0.0161

4.3.2 Convergence of the near field integral

The near field disturbance in (3.143) with $\mu_R = 0$ is

$$N(\boldsymbol{x}') = \frac{2}{\pi}\int_{-\infty}^{\infty} Re\{e^{\bar{\chi}}E_1(\bar{\chi})\}dT \tag{4.30}$$

where

$$\bar{\chi} = (1+T^2)z' + i[x' + y'T](1+T^2)^{1/2}. \tag{4.31}$$

The near field integrand for the selected panels in Figure 19 are shown in Figure 29, the near field is integrated from $-\infty$ to ∞, but only the positive side is shown in Figure 29. Changing the sign of T in (4.31) is the same as changing the sign of y so the behaviour of negative T for negative y is the same as the behaviour of positive T for positive y. The near field for the green panels is very similar to the near field for the red panels (see Figure 19); the only difference is that the imaginary part is zero.

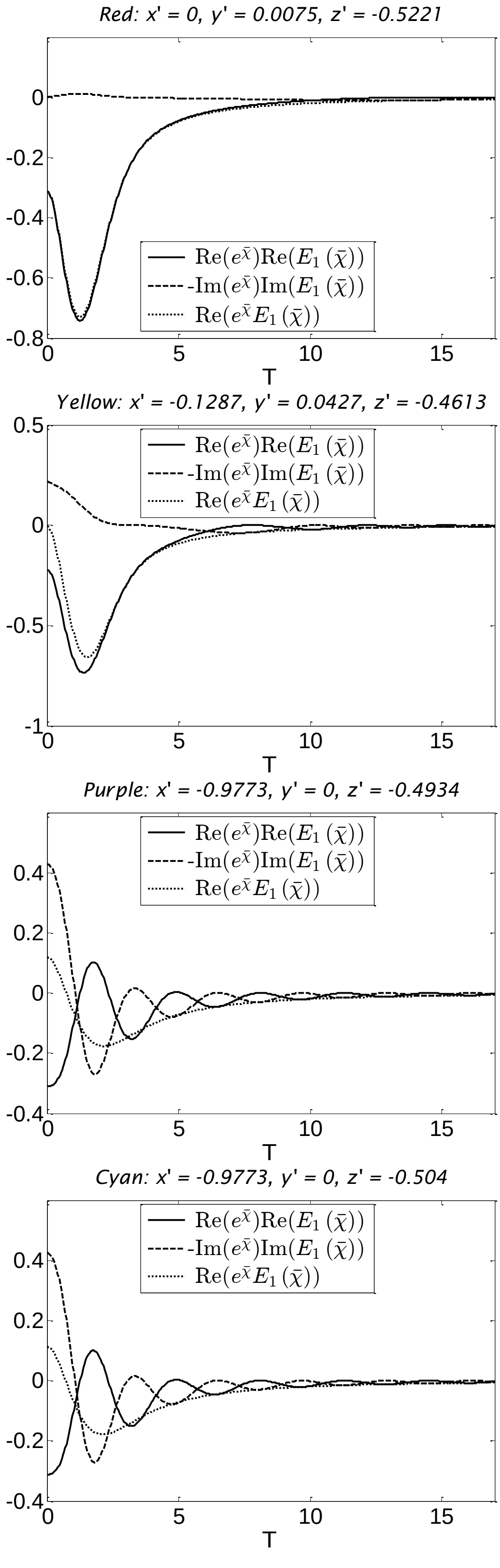

Red: x' = 0, y' = 0.0075, z' = -0.5221

Yellow: x' = -0.1287, y' = 0.0427, z' = -0.4613

Purple: x' = -0.9773, y' = 0, z' = -0.4934

Cyan: x' = -0.9773, y' = 0, z' = -0.504

Figure 29 Near field integrand

The standard function E_1 is evaluated using a Taylor expansion for the special case around $y' = 0$. For small arguments (small $\bar{\chi}$) a series expansion (5.1.10, Abramowitz & Stegun, 1964) is used and for larger arguments a continued fraction (5.1.22, Abramowitz & Stegun, 1964). For further information on the evaluation of the exponential integral see Pegoraro and Slusallek (2011). To determine when the integrand approaches zero only the case when T is large is of interest. The continued fraction is

$$E_n(\bar{\chi}) = e^{-\bar{\chi}}\left(\frac{1}{\bar{\chi}+}\frac{n}{1+}\frac{1}{\bar{\chi}+}\frac{n+1}{1+}\frac{2}{\bar{\chi}+}\dots\right) \quad (|arg\bar{\chi}| < \pi). \tag{4.32}$$

Inserting (4.32) in the integrand in (4.30) will eliminate the exponential part and only leave the continued fraction

$$N_I = Re\left\{\left(\frac{1}{\bar{\chi}+}\frac{n}{1+}\frac{1}{\bar{\chi}+}\frac{n+1}{1+}\frac{2}{\bar{\chi}+}\dots\right)\right\} \quad (n = 1). \tag{4.33}$$

$\bar{\chi}$ is complex and the real part is negative since for submerged bodies $z' < 0$. To limit the continued fraction an inequality is used, this must be done using the absolute value since the function is complex, since $n = 1$ and without loss of generality it is assumed that

$$\cfrac{1}{\bar{\chi} + \cfrac{n}{1 + \cfrac{1}{\bar{\chi} + \cfrac{1}{\ddots}}}} = \lim_{m\to\infty} \cfrac{1}{\bar{\chi} + \cfrac{n}{1 + \cfrac{1}{\bar{\chi} + \cfrac{1}{\bar{\chi} + \ddots \frac{1}{1}}}}} = C^m. \tag{4.34}$$

By induction:

$$|C^m| < \frac{1}{|\bar{\chi}| - 1}, \tag{4.35}$$

since if $m = 1$

$$\left|\frac{1}{|\bar{\chi}| + 1}\right| < \frac{1}{|\bar{\chi}| - 1}. \tag{4.36}$$

Assume that if $m = m$, (4.35) is valid, then must

$$\begin{aligned}|C^{m+1}| &= \left|\frac{1}{\bar{\chi}+C^m}\right| < \frac{1}{|\bar{\chi}|-|C^m|} < \frac{1}{|\bar{\chi}|-\frac{1}{|\bar{\chi}|-1}} = \frac{1}{\frac{|\bar{\chi}|(|\bar{\chi}|-1)-1}{|\bar{\chi}|-1}} \\ &= \frac{|\bar{\chi}|-1}{|\bar{\chi}|^2-|\bar{\chi}|-1}.\end{aligned} \tag{4.37}$$

(4.35) is satisfied if

$$\frac{|\bar{\chi}|-1}{|\bar{\chi}|^2-|\bar{\chi}|-1} < \frac{1}{|\bar{\chi}|-1}, \tag{4.38}$$

which hold true if

$$|\bar{\chi}| > 3. \tag{4.39}$$

(4.39) is satisfied as long as T is sufficiently large. As before there is no reason to continue integration when the integrand is less than 10^{-5}, therefore T_{max} is set to satisfy:

$$\frac{1}{|\bar{\chi}|-1} \leq 10^{-5}. \tag{4.40}$$

When looking at $\bar{\chi}$ in (3.133) it is evident that (3.142) will go to zero faster when $|y'|$ or $|z'|$ are large and that the value of x' is of less importance. T_{max} will therefore depend only on z' and y'. T_{max} as a function of z' and y' for $x' = 0$ is shown in Figure 30.

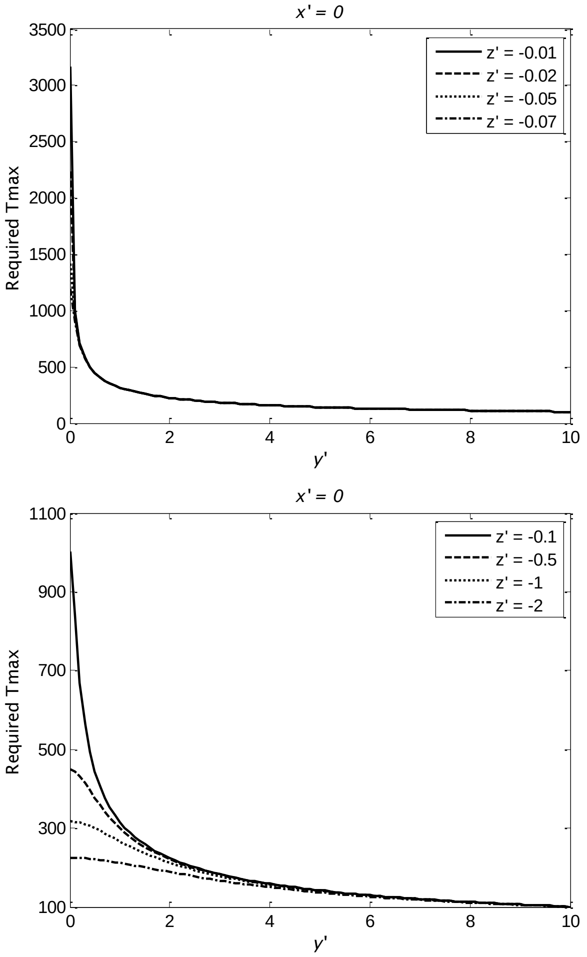

Figure 30 Required T_{max} as a function of y' for varying z'

From Figure 30 it is clear that $T_{max} = 500$ is sufficient if $z' \leq -0.5$. Figure 31 shows two magnifications of Figure 30.

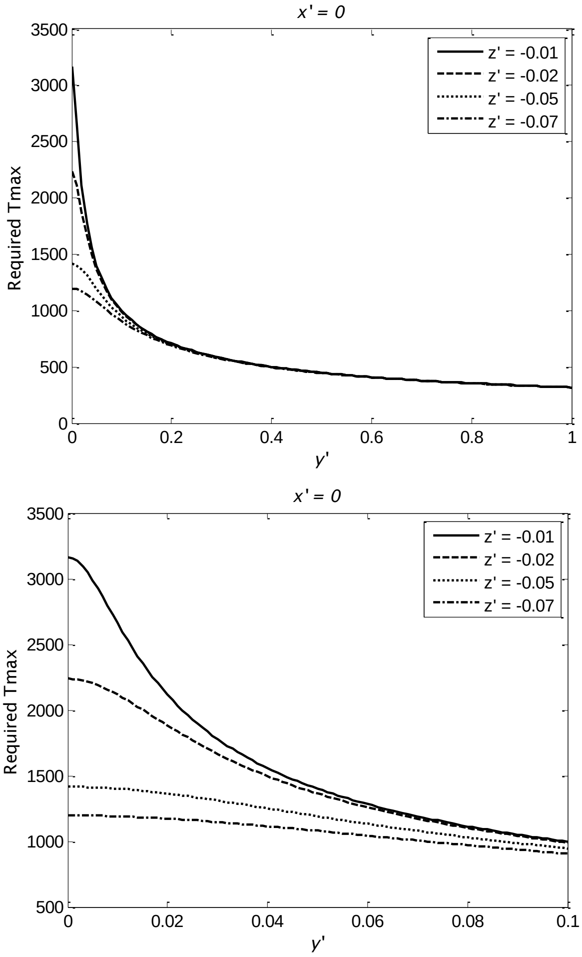

Figure 31 Magnifications of Figure 30

Based on Figure 30 and Figure 31, the required T_{max} for different values of y' and z' are shown in Figure 32. All required T_{max} according to Figure 32 are sufficiently large satisfy (4.39).

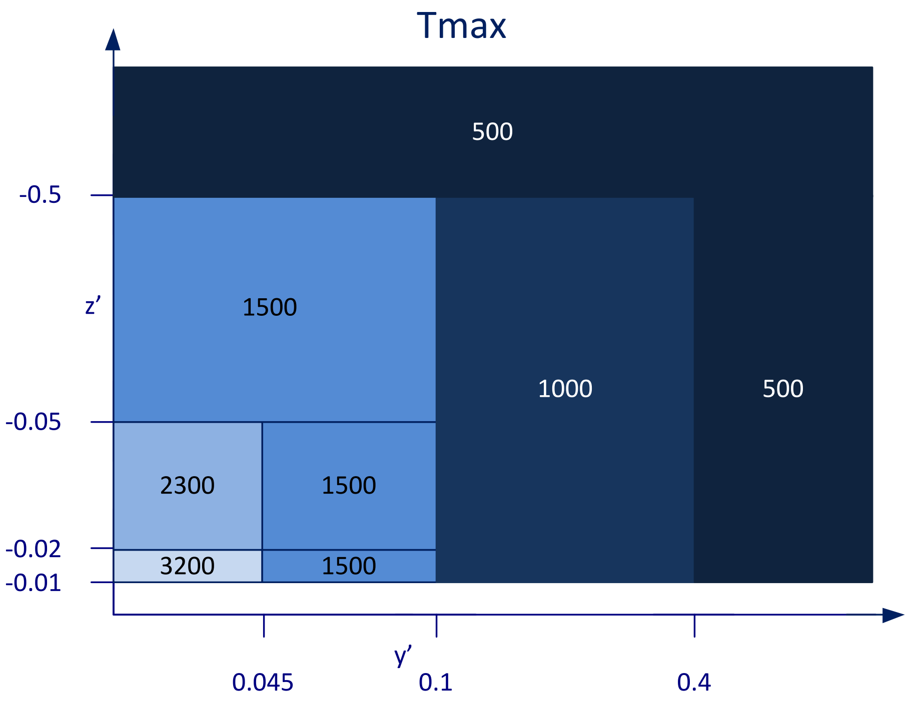

Figure 32 T_{max} as a function of z' and y'

The error is determined by setting n_T to $100T_{max}$ and then doubling T_{max} to determine the change in $\frac{\partial N}{\partial x}$ and N. The pressure is calculated according to (3.65) where the leading terms are the far field and near field and its derivatives in x −direction. For the submerged ellipsoid in Figure 19 the maximum difference for $\frac{\partial N}{\partial x}$ is $7.3 \cdot 10^{-6}$% when T_{max} is doubled. For N the maximum difference is 0.3% when T_{max} is doubled.

4.3.2.1 n_T for the Near field integral

For the near field integral n_T is determined by establishing the percentage difference with $n_T = 10000T_{max}$ as a reference value. N is unaffected by the change of n_T. N is not as dependent on n_T as $\partial N/\partial x$. From Table 8 it is clear that $n_T = 15T_{max}$ is sufficient.

Table 8 Percentage difference n_T

$\frac{n_T}{T_{max}}$	$\% \frac{\partial N}{\partial x}$
5	1.7
10	1.1
15	0.47
20	0.31
50	0.065

4.3.3 Summary

The far field integral and its derivative approach zero fast so a low T_{max} is possible. The near field integral and its derivatives approach zero slowly and therefore require a large T_{max}. Because T_{max} depends on z' and y', n_T must be a function of T_{max} to allow the step length in the summations to be constant. The findings are summarised in Table 9.

Table 9 Summary T_{max} and n_T

	Far field	Near field
T_{max}	5 to 35	500 to 3200
n_T/T_{max}	10	15

5 Validation

The presented method is evaluated against numerical and experimental results for a range of validation cases. Having verified the level of numerical accuracy of the solutions in Chapter 4, comparisons with existing data must be made in order to assess the actual validity of the method. Three standard cases will be shown that are far from discriminative but they permit comparison with results of others. Firstly section 5.1 evaluates the results for a single source, section 5.2 concerns the wave pattern for a thin ship Wigley hull and finally section 5.3 evaluates the resistance of fully submerged bodies.

5.1 Single source

Combinations of sources and sinks are used in the presented method to represent arbitrary bodies. If the method is successful in the case of a single source, it should in principle be applicable in general. The wave pattern behind a single source is well known from previous studies. When the field point is on the free surface Green function will reduce to the single integrals. Combining (3.23), (3.59), (3.94), (3.139) and (3.148) gives the wave profile for a single submerged source. The wave pattern due to a unit single source is seen in Figure 33, where the Froude number refers to the depth Froude number. The source is located at $(a,b,c) = (0,0,-0.3)/Fn^2$ and the surface profile is evaluated in 41x21 points. The results show good correlation with the results by Hoff (p. 207, 1990) (not shown). The general profile of the free surface is also consistent with Nakatake (1966) and Aanesland (p. 71,1986), Nakos and Sclavounos (1990).

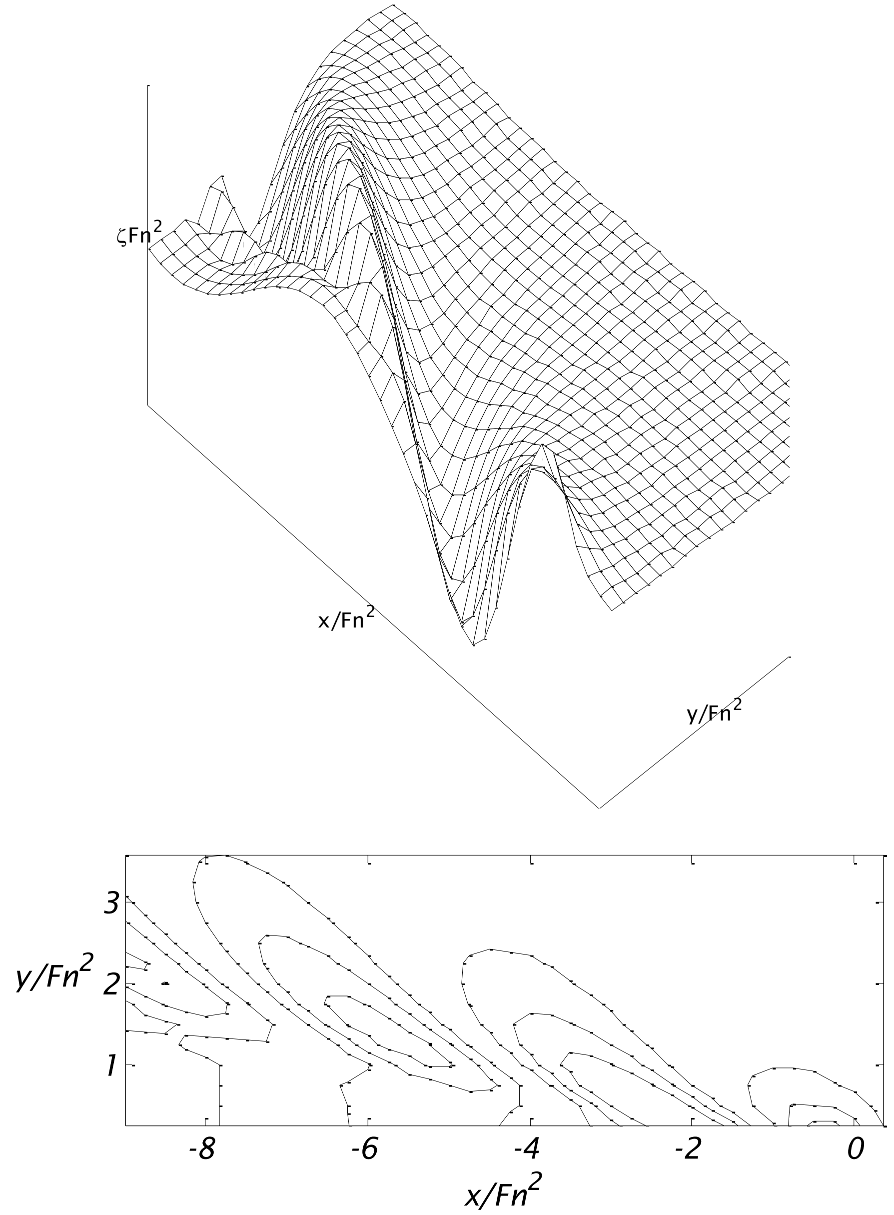

Figure 33 Wave pattern behind a single source

5.2 Wigley hull

The next test case is the mathematical Wigley hull. The hull has a smooth gradient, has a fore-aft symmetry and can be categorised as thin. An abundance of numerical and experimental data exist for the Wigley hull which makes it well suited for comparison. The Wigley hull shape is defined as

$$y_s = \frac{B}{2}\left(1 - \left(\frac{z_s}{D}\right)^2\right)(1 - 4x_s^2), \tag{5.1}$$

where B is the beam D the depth and (x_s, y_s, z_s) is the location of the hull surface. Using (4.9) it follows that the non-dimensionalised source strength in a single point is

$$Q(x_s, z_s) = -4B \left(z_{s0} - z_{s1} + \frac{z_{s1}^3 - z_{s0}^3}{3D^2} \right) (x_{s1}^2 - x_{s0}^2). \tag{5.2}$$

Table 10 provides the non-dimensionalised hull form for the Wigley hull. The ship length L is used as the characteristic length in the Froude number.

Table 10 Wigley hull

L	1
B	0.1
D	0.0625

The wave pattern is evaluated using thin-ship theory with no damping. Figure 34 depicts the wave pattern along the hull normalised with the Froude number squared compared with the thin-ship theory predictions by Noblesse et al. (2009) and experimental results measured at the University of Tokyo (Kajitani et al, 1983, Mccarthy, 1985). The results shows good comparison with the numerical results by Noblesse et al. (2009) and reasonable accuracy compared with the experimental results.

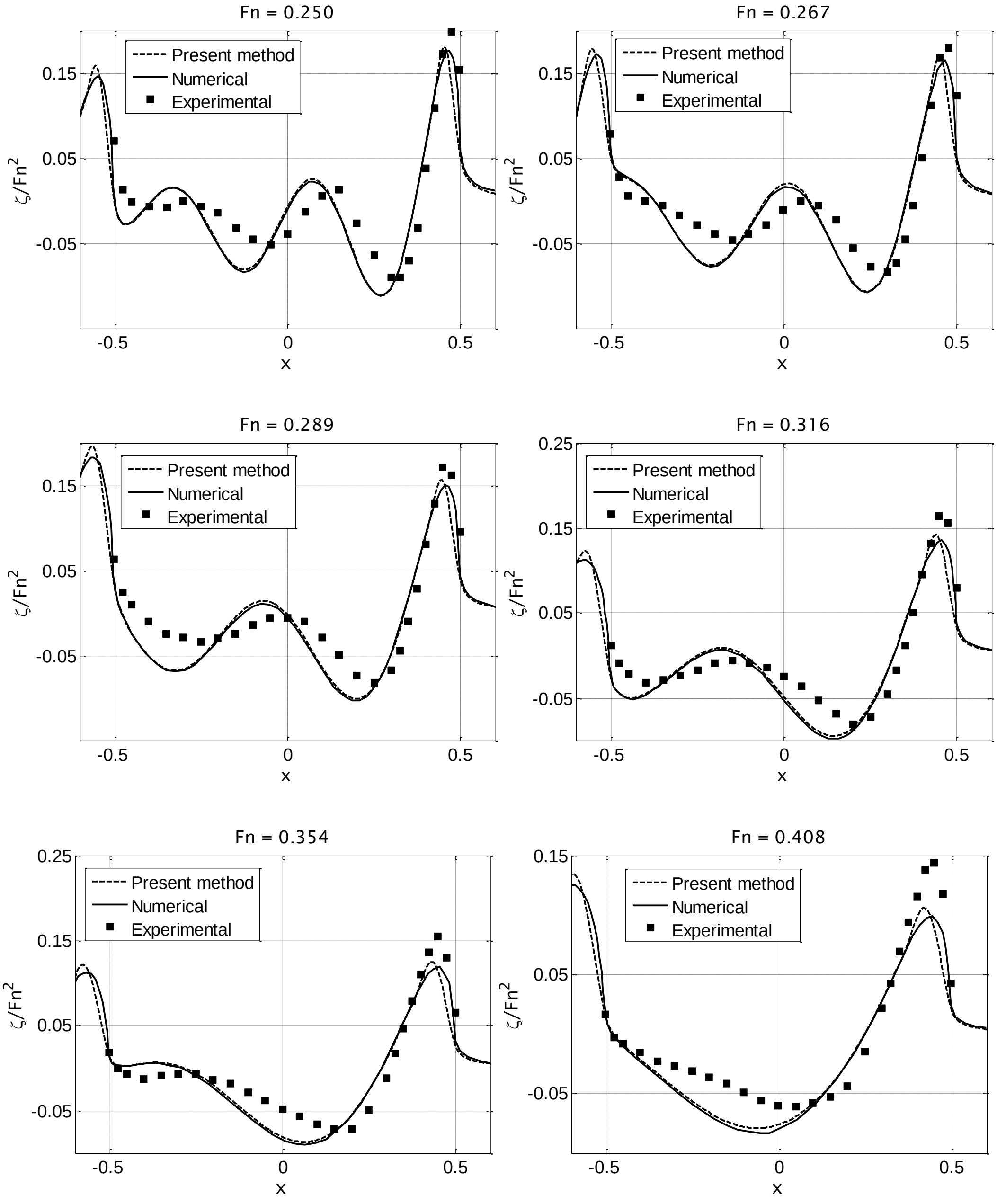

Figure 34 Wave elevation of the wave profile predicted by thin-ship theory compared to numerical (Noblesse et al, 2009) and experimental (Kajitani et al, 1983, Mccarthy, 1985) results

5.3 Fully submerged bodies

Previous numerical results for the wave resistance of a body travelling at constant forward speed near a free surface are widely available. These are usually presented in the form of the wave resistance coefficient C_w defined as;

$$C_w = \frac{-R_w}{\pi \rho g {L_{ref}}^3}. \tag{5.3}$$

The present method is evaluated here against previous results for a submerged ellipsoid and sphere. The characteristic reference length L_{ref} is the focal distance c_e for the ellipsoid and the radius R_s for the sphere. R_w is the wave resistance force acting on the submerged body.

5.3.1 Ellipsoid

An ellipsoid with the major axis parallel to the free surface is submerged to 3 different depths corresponding to $d_e/c_e = (0.252, 0.3266, 0.5)$. The lengths of major and minor axes are $2a_e = 2.3$ and $2b_e = 0.4$, the axis are illustrated in Figure 35. The Froude number is calculated with twice the focal distance as the characteristics length.

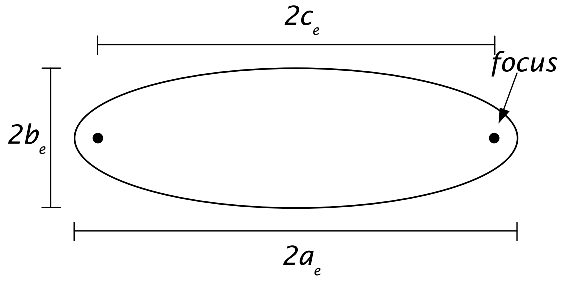

Figure 35 Axes of the ellipsoid

The surface of the half ellipsoid is discretised using 20 panels along the major axis and 10 panels along the minor axis. The results are compared with the semi-analytical results by Farell (1973), the panel based method by Chen et al. (2001) and the panel method by Baar (1986) in Figure 36. Baar's results are generated for this ellipsoid using a code based on his method. The results are tabulated in Table 11 to Table 13; Farell did not provide any tabulated data so his results are not included in the tables. Chen et al. (2001) discretised the ellipsoid using 90 panels, 8 along the major axis, 10 around the x-axis except at the forward and aft vertices where only 5 panels are used. Farell has not presented any result for the deepest submersion for this ellipsoid.

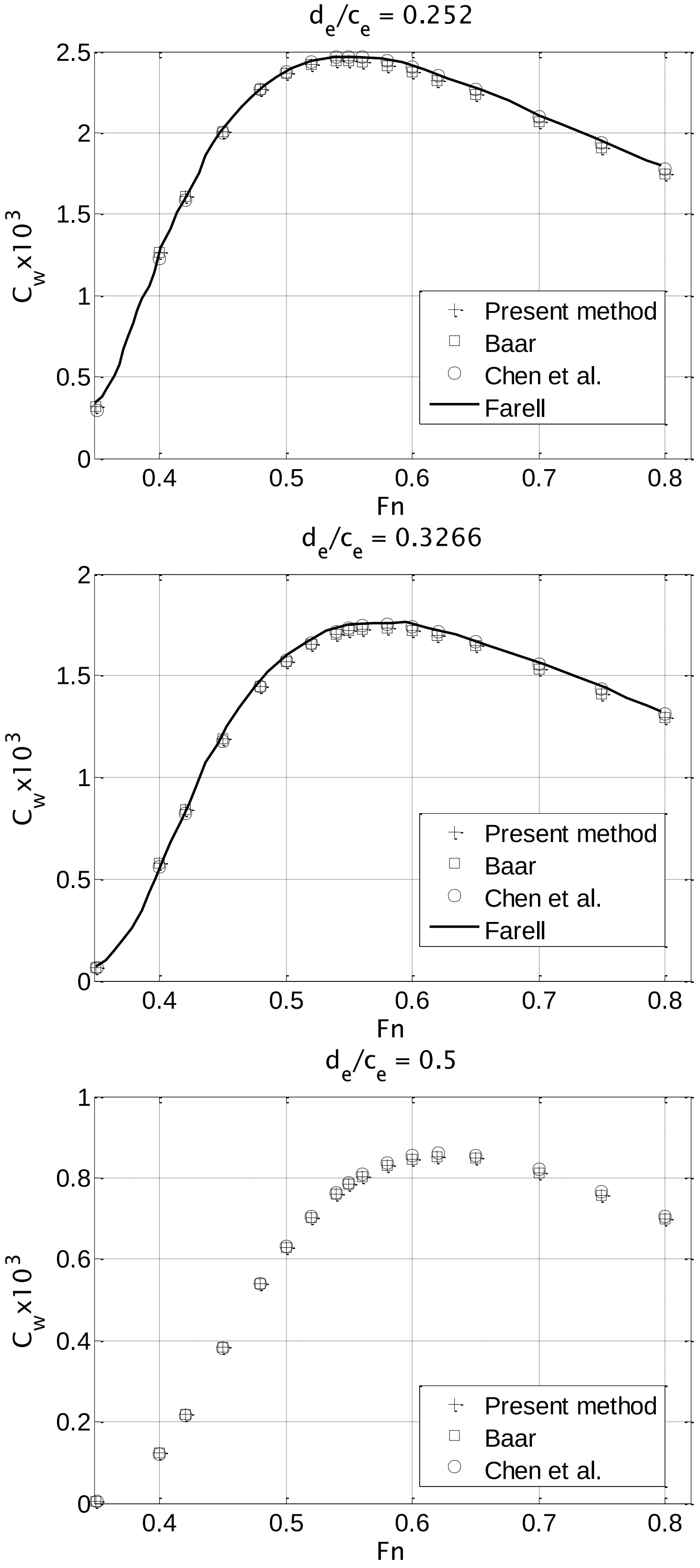

Figure 36 Wave resistance coefficient as a function of Froude number

Table 11 C_wx10^3 for d_e/c_e=0.252

Fn	Present method	Baar	Chen
0.35	0.3191	0.3191	0.2907
0.4	1.2622	1.2622	1.2293
0.42	1.6113	1.6112	1.5862
0.45	2.01	2.0099	2.0017
0.48	2.2633	2.2631	2.2685
0.5	2.3629	2.3627	2.3762
0.52	2.4195	2.4192	2.4386
0.54	2.4414	2.4411	2.4649
0.55	2.4419	2.4416	2.4673
0.56	2.4366	2.4363	2.4636
0.58	2.4117	2.4114	2.441
0.6	2.372	2.3718	2.4027
0.62	2.3214	2.3212	2.3534
0.65	2.233	2.2329	2.2655
0.7	2.0694	2.0694	2.1017
0.75	1.9037	1.9039	1.9351
0.8	1.7467	1.7469	1.7766

Table 12 $C_w x10^3$ for d_e/c_e =0.3266

Fn	Present method	Baar	Chen
0.35	0.0671	0.0671	0.0614
0.4	0.5766	0.5766	0.5620
0.42	0.8383	0.8383	0.8244
0.45	1.1872	1.1872	1.1799
0.48	1.4484	1.4484	1.4480
0.5	1.5691	1.5691	1.5739
0.52	1.6529	1.6529	1.6614
0.54	1.7045	1.7045	1.7163
0.55	1.7199	1.7199	1.7332
0.56	1.7297	1.7297	1.7442
0.58	1.734	1.734	1.7505
0.6	1.7222	1.7222	1.7401
0.62	1.6981	1.698	1.7169
0.65	1.6459	1.6458	1.6655
0.7	1.5346	1.5345	1.5543
0.75	1.4127	1.4126	1.4318
0.8	1.2926	1.2926	1.3108

Table 13 C_wx10^3 for d_e/c_e =0.5

Fn	Present method	Baar	Chen
0.35	0.0053	0.00528	0.0049
0.4	0.1244	0.12441	0.1222
0.42	0.2194	0.21940	0.2167
0.45	0.3823	0.38231	0.3808
0.48	0.5396	0.53960	0.5396
0.5	0.6289	0.62886	0.6306
0.52	0.7030	0.70293	0.7059
0.54	0.7606	0.76060	0.7618
0.55	0.7832	0.78319	0.7883
0.56	0.8025	0.80250	0.8081
0.58	0.8306	0.83054	0.8372
0.6	0.8467	0.84662	0.8541
0.62	0.8528	0.85274	0.8607
0.65	0.8472	0.84713	0.8557
0.7	0.8113	0.81126	0.8201
0.75	0.7576	0.75762	0.7663
0.8	0.6976	0.69759	0.7059

An ellipsoid with the major axis parallel to the free surface is submerged to 2 different depths corresponding to $d_e/c_e = (0.3266, 0.5)$. The lengths of major and minor axes are $2a_e = 5$ and $2b_e = 1$ respectivly. The Froude number is calculated with the major axis as the characteristics length. The surface of the half ellipsoid is discretised using 20 panels along the major axis and 10 panels along the minor axis. The results are compared with the semi-analytical results by Farell (1973), the Neumann-Kelvin panel method by Doctors and Beck (1987a) and a higher order panel by Belibassakis et al. (2013) in Figure 37 and Figure 38 . Doctors and Beck (1987a) discretised the ellipsoid using 16 panels along the major axis and 8 around the x-axis. Belibassakis et al. (2013) uses two different discretisations for their spline based higher order panels. They differ in the sense one uses 2-knot insertion and the other a 4-knot insertion process. It is clear that the agreement is good compared to existing data. Farell (1973) only provides result for low and medium Froude number for the shallow submersion as seen in Figure 38 (top).

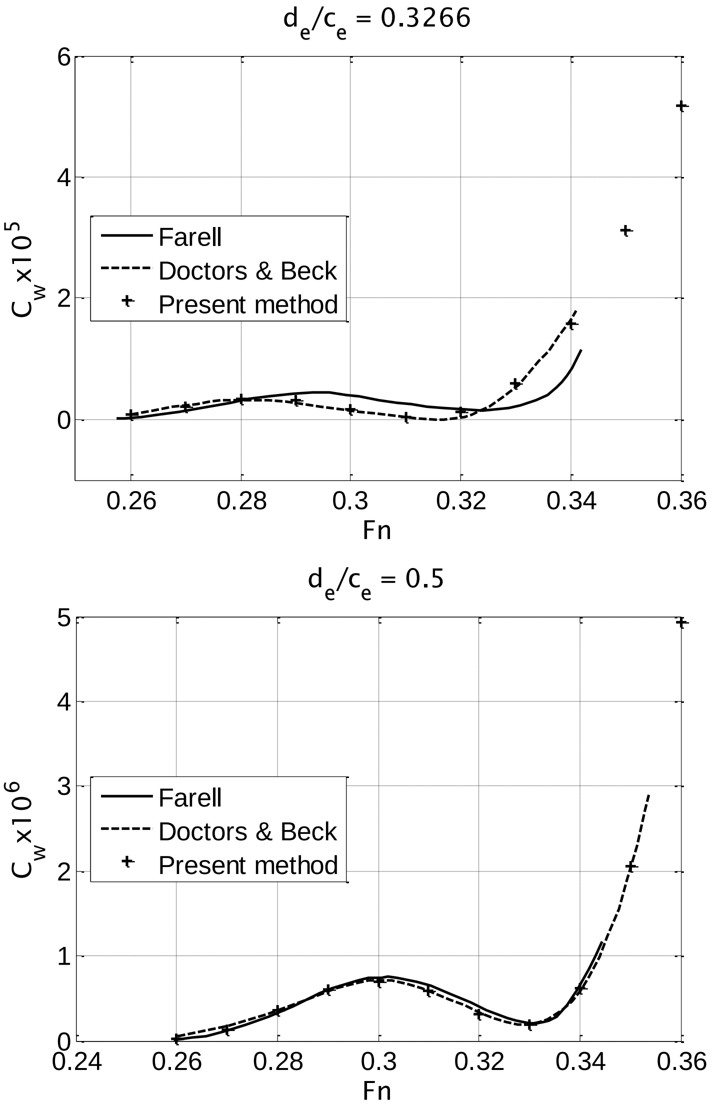

Figure 37 Ellipsoid with a_e/b_e = 5 at low Froude numbers

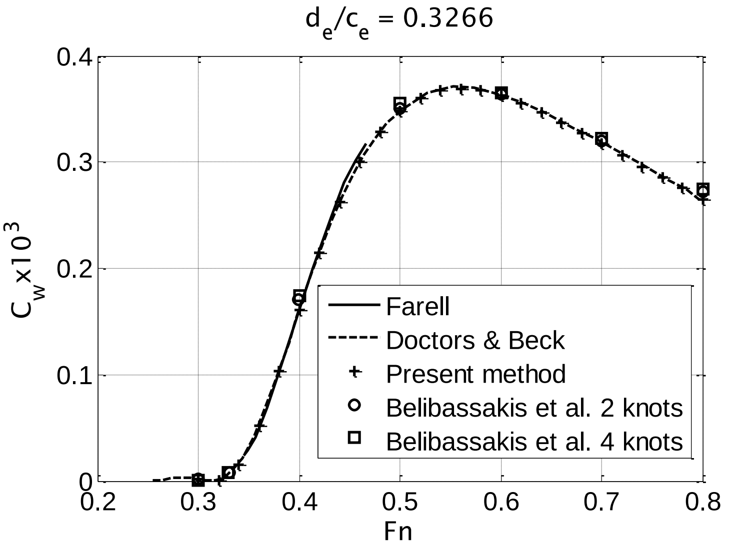

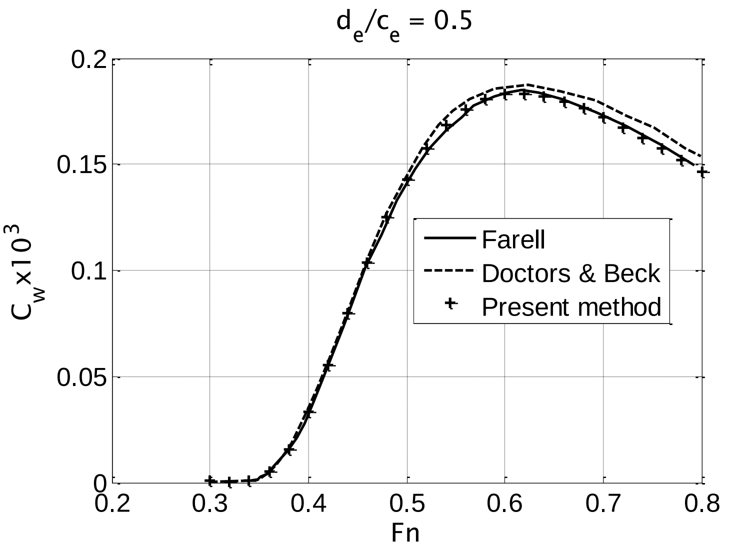

Figure 38 Ellipsoid with $a_e/b_e = 5$ at high Froude numbers

5.3.2 Sphere

A sphere with radius R_s and diameter D_s defined by Wu (1995) is submerged to two depths corresponding to $d_s/R_s = (1.1, 2.0)$. The Froude number is calculated with the diameter as the characteristic length. The results are compared with the panel based method by Chen et al. (2001) and the panel method by Baar (1986) in Figure 39. Again Baar's results are generated for this sphere using a code based on his method. The results for the shallow submersion are tabulated in Table 14; Chen et al. (2001) did not provide any tabulated data for the deeper submersion. Chen et al. (2001) discretised the sphere using 56 panels, 8 along x-axis, 8 around the x-axis except at the forward and aft vertices where only 4 panels are used. It is clear from Figure 39 that more panels are needed for the present method and the one by Baar, compared to Chen et al. (2001) method, for all the results to converge to a common curve. For the present method a larger number of panels are used along the x-axis.

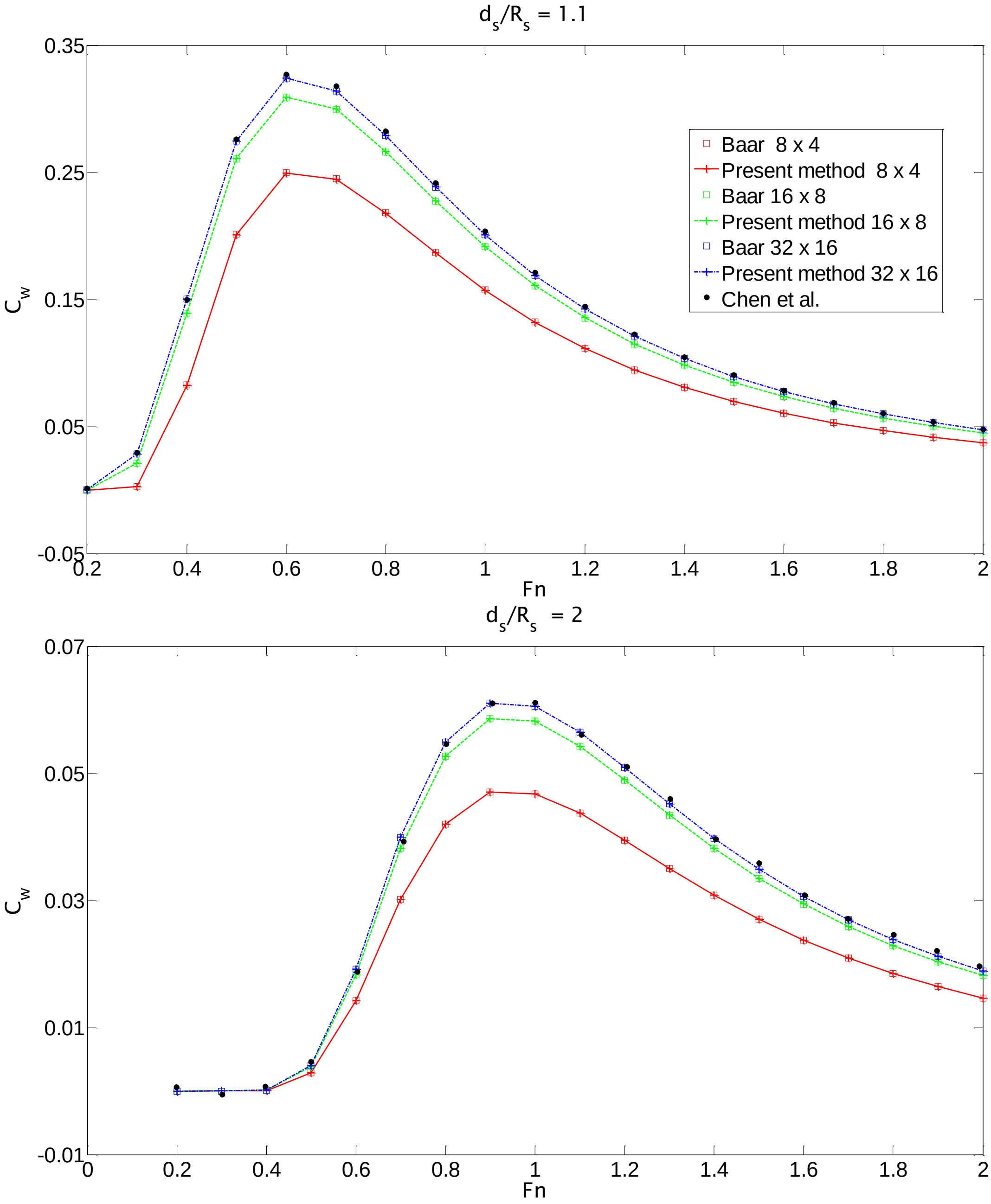

Figure 39 C_w for the submerged sphere

Table 14 $C_w x10^3$ for d_s/R_s=1.1 and 32x16 panels

Fn	Present method	Baar	Chen
0.2	5E-05	5E-05	0.0010
0.3	0.0284	0.0283	0.0296
0.4	0.1501	0.1500	0.1497
0.5	0.2744	0.2744	0.2759
0.6	0.3238	0.3238	0.3270
0.7	0.3140	0.3140	0.3178
0.8	0.2789	0.2788	0.2824
0.9	0.2384	0.2383	0.2415
1.0	0.2009	0.2008	0.2035
1.1	0.1688	0.1688	0.1710
1.2	0.1424	0.1424	0.1442
1.3	0.1209	0.1209	0.1224
1.4	0.1035	0.1034	0.1047
1.5	0.0892	0.0892	0.0903
1.6	0.0776	0.0776	0.0784
1.7	0.068	0.0679	0.0687
1.8	0.0599	0.0599	0.0605
1.9	0.0532	0.0532	0.0537
2.0	0.0476	0.0476	0.0480

6 Applications

The theory developed in the foregoing chapters has been compared to existing numerical results to show that it produces similar results when $\mu_R' = 0$. However, the purpose of developing the present method has been to improve on these methods and to produce results when $\mu_R' \neq 0$. This chapter serves to give an indication of suitable values of μ_R'. Results are presented over a prescribed range of Froude number and compared with experimental data. Both the exact Neumann-Kelvin solution and thin ship approximation are considered. The present method with zero Rayleigh damping gives the wave resistance, whereas if damping is added it can determine the residual resistance. The residual resistance coefficient is

$$C_r = \frac{-R_r}{\pi \rho g {L_{ref}}^3}, \tag{6.1}$$

Where the R_r is the residual resistance and L_{ref} is the characteristic length.

6.1 Range of the damping coefficient

The damping coefficient μ_R' is small compared to the other variables in the modified Navier-Stokes equation (3.9). However the effect of μ_R' on the wave pattern behind a Wigley hull is clearly seen in Figure 40. A further indication of the range of possible damping coefficients can be found in Fürth (2011) and Fürth et al. (2013) (Appendix A). The Wigley hull is modelled using thin-ship theory with different values of the damping coefficient. 40x1 sources are placed on the centre plane to model the hull. As μ_R' is increased the wave pattern becomes more dampened.

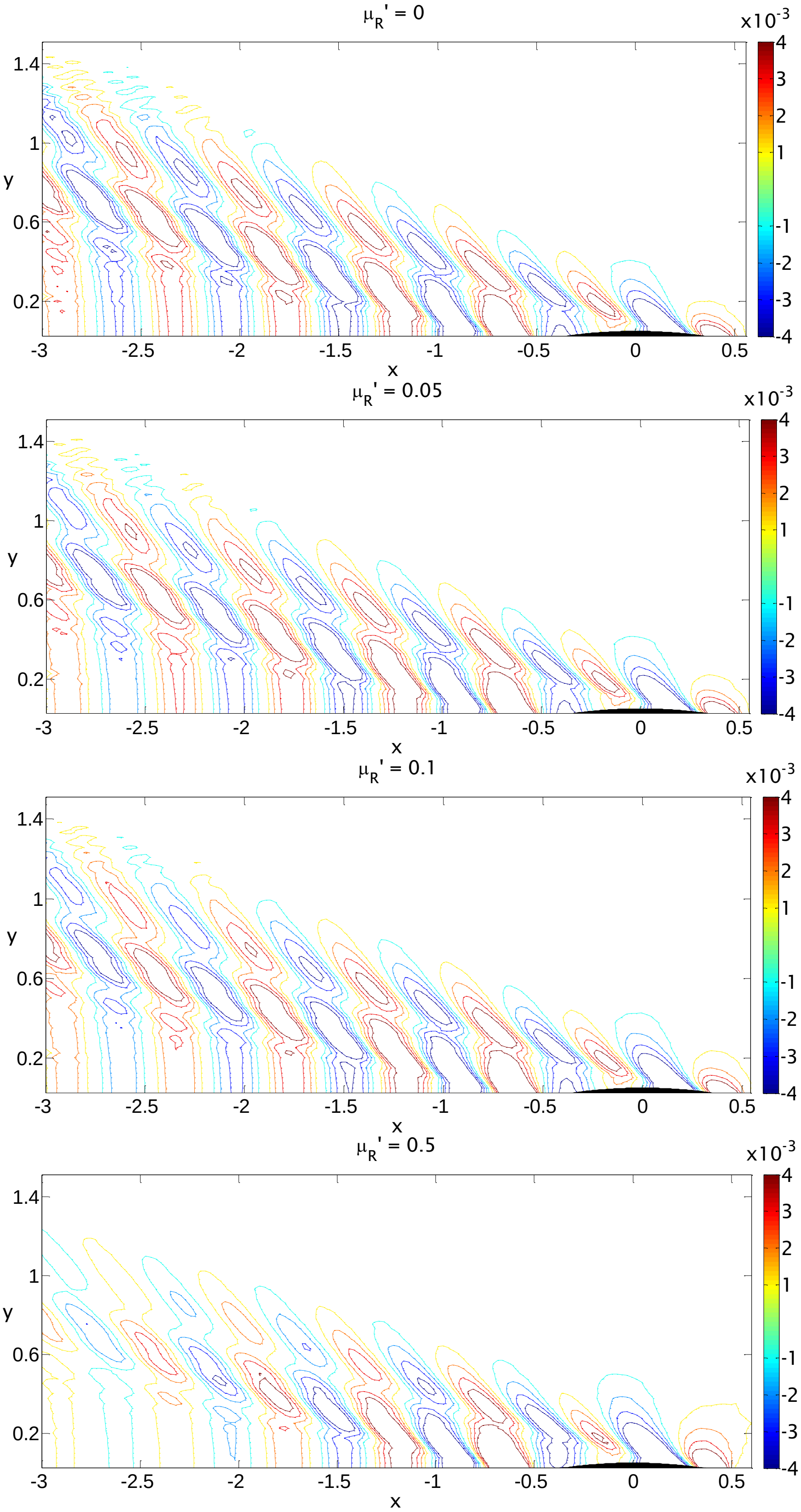

Figure 40 Wave behind a Wigley hull using thin ship theory $Fn = 0.3$

6.1.1 Range of the damping coefficient for a slender body

The ellipsoid previously described in chapter 5.3.1. is used to investigate the influence on resistance of a range of μ_R' values, as before the characteristic length used to determine the resistance coefficient is the focal distance and the Froude number it is twice the focal distance. A possible range for μ_R' is shown in Figure 41 and Figure 42 for a slender body at shallow submersion. From Figure 41 it is clear that the profile for the residual resistance coefficient C_r distorts for $\mu_R' > 0.1$, which could imply a upper limit for μ_R' since it is unlikely that low speeds would give this much larger resistance coefficient than higher speeds. The resistance curves in Figure 42 cross each other between $Fn = 0.4$ and $Fn = 0.45$ and again at in the region of $Fn = 0.6$. This characteristic could indicate that the damping has changed the relationship between the bow and stern waves. That is, these waves interact at a different Froude number and hence the resistance hump occurs at a different Froude number. Consequently the curves cross so that a higher damping yields a lower resistance, which is not physically correct. Intuitively a higher damping coefficient implies a more viscous fluid and a more viscous fluid would yield a higher resistance.

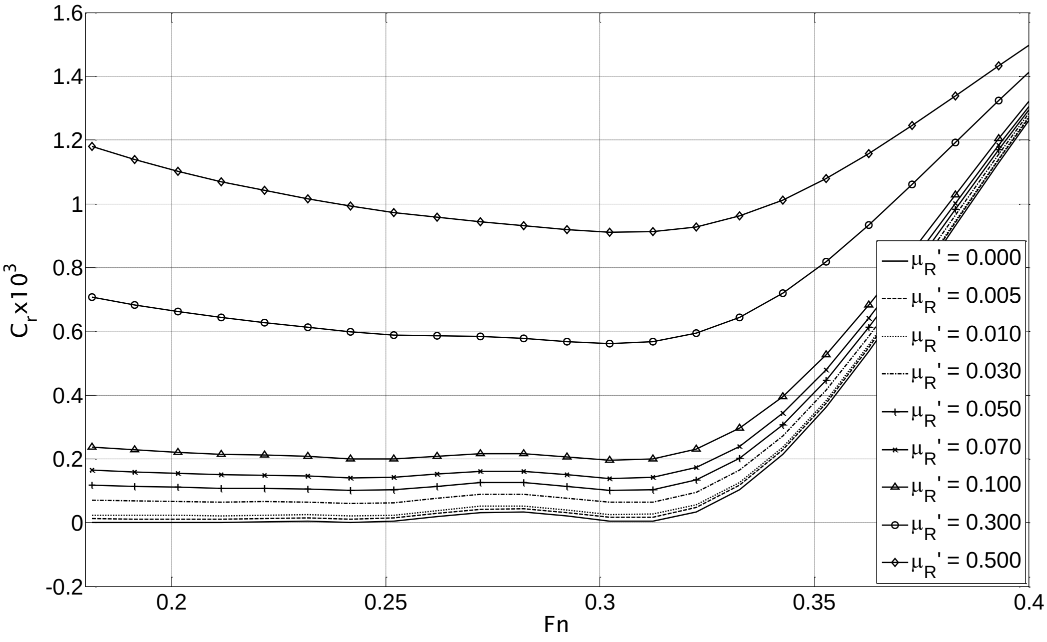

Figure 41 C_r for an ellipsoid submerged to d_e/c_e =0.252 at low speeds

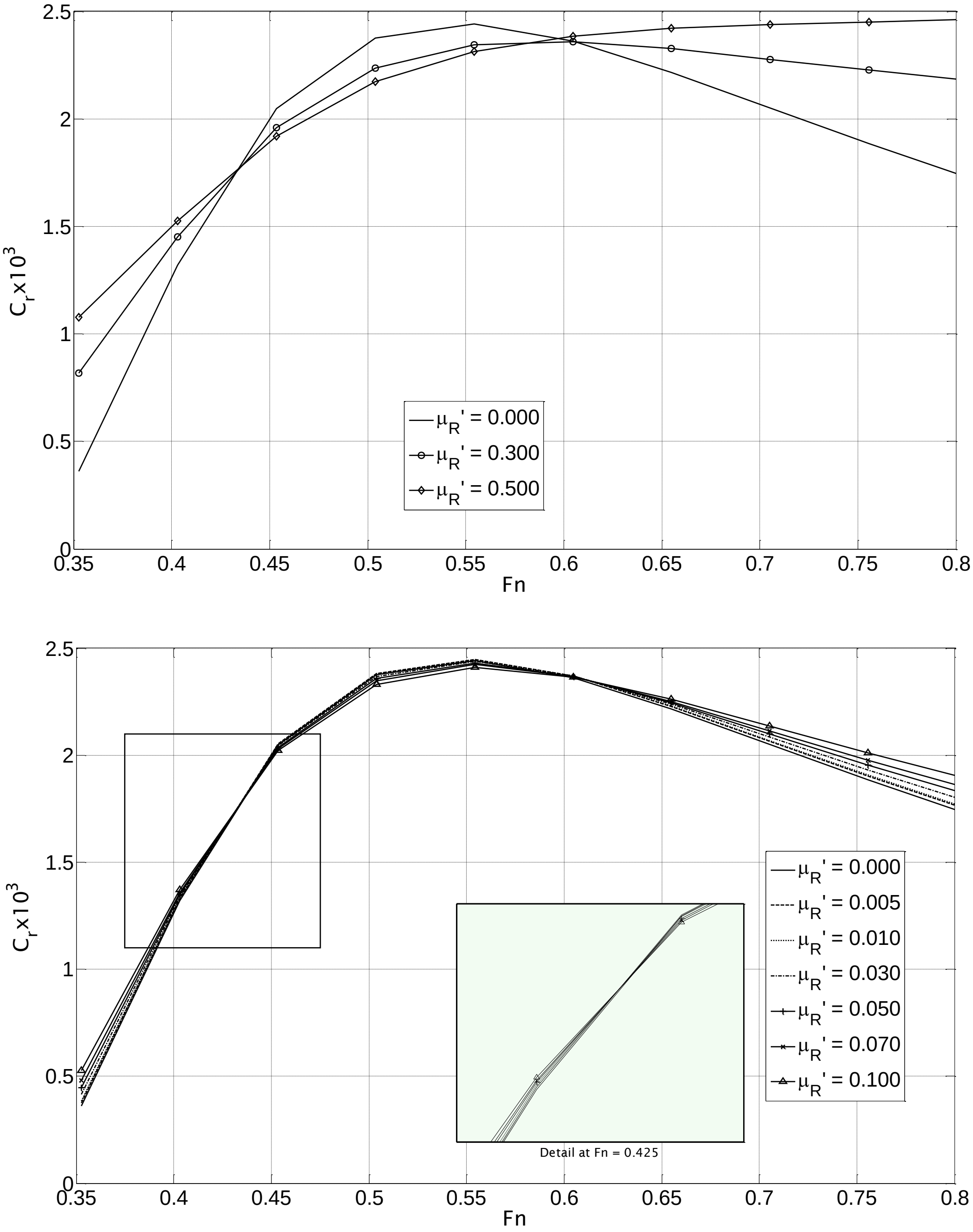

Figure 42 C_r for an ellipsoid submerged to d_e/c_e =0.252 at high speeds

Results for a deeper submersion of the ellipsoid are depicted in Figure 43 to Figure 44. A final and deepest submersion is shown in Figure 45 and Figure 46. From Figure 43 and Figure 45 it is clear that the effect of μ_R' is the same regardless of submersion depth for the slender ellipsoid at low speeds. From Figure 43, Figure 45 and Figure 46 it can be seen that $\mu_R' > 0.1$ may not be suitable since the general shape of the curve distorts. However Figure 44 and

Figure 46 show that for larger submersions the resistance curves do not cross each other as in Figure 42.

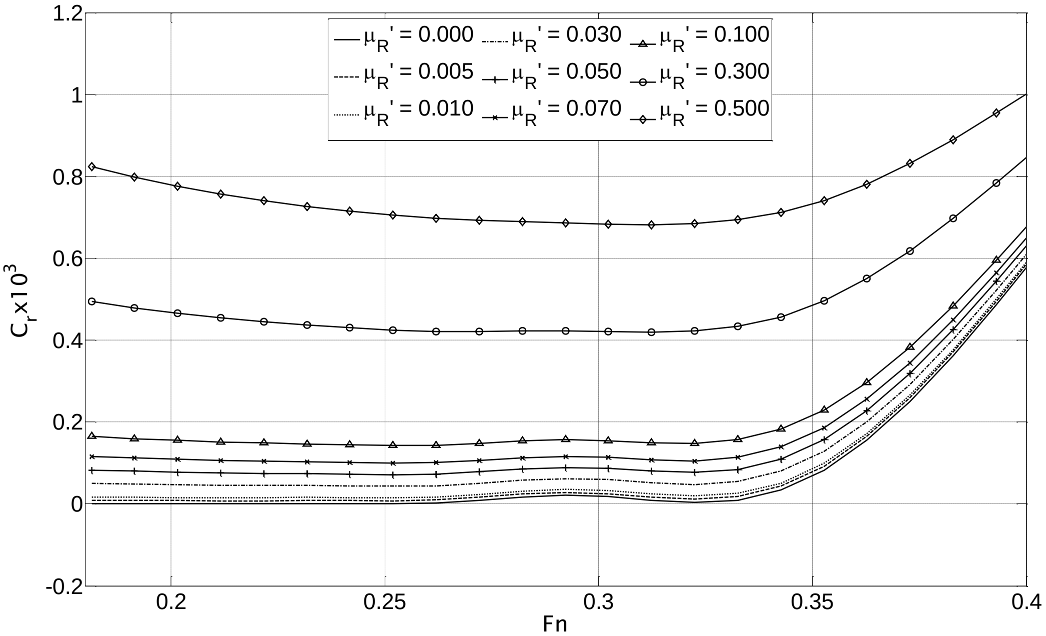

Figure 43 C_r for an ellipsoid submerged to d_e/c_e =0.3266 at low speeds

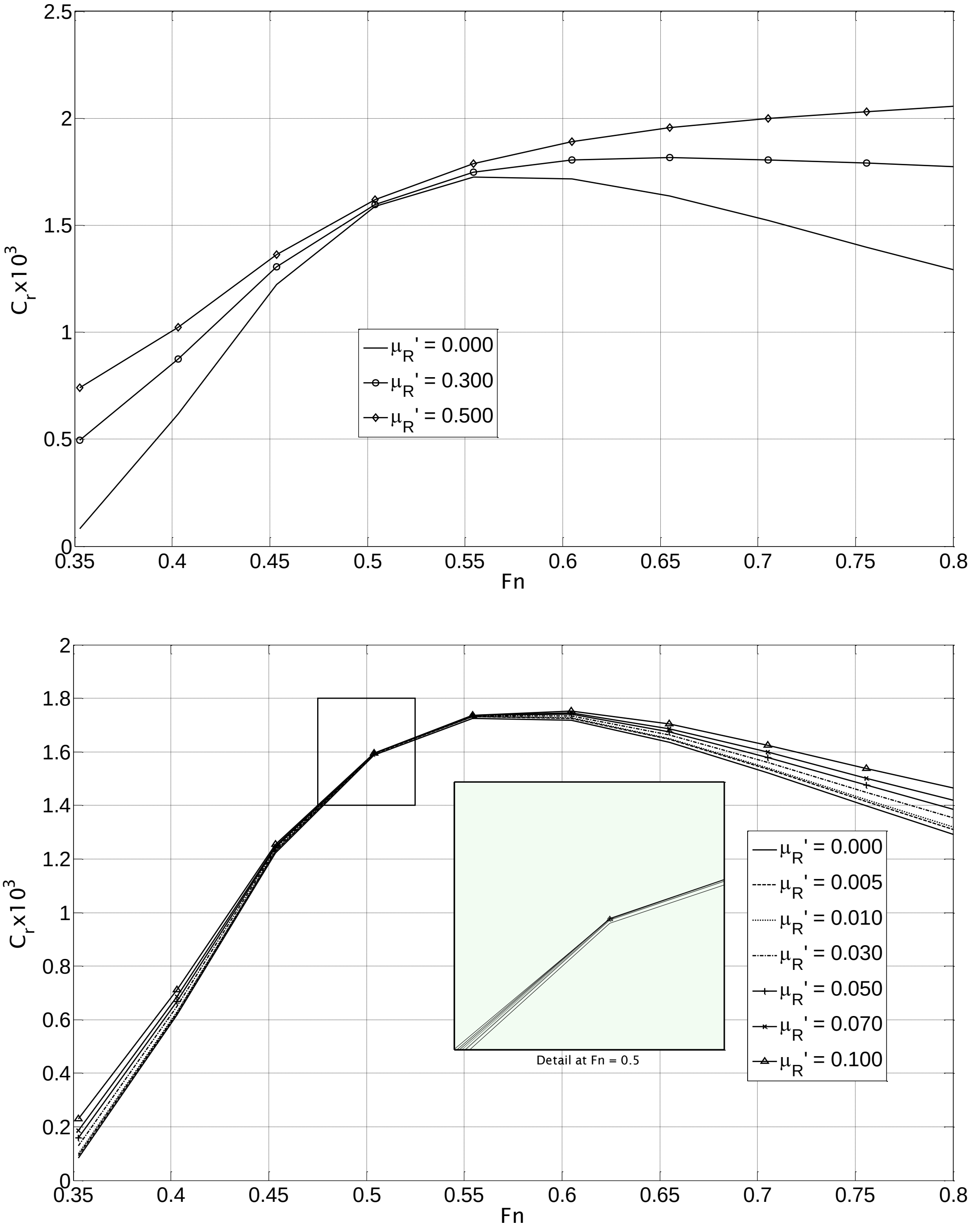

Figure 44 C_r for an ellipsoid submerged to d_e/c_e =0.3266 at high speeds

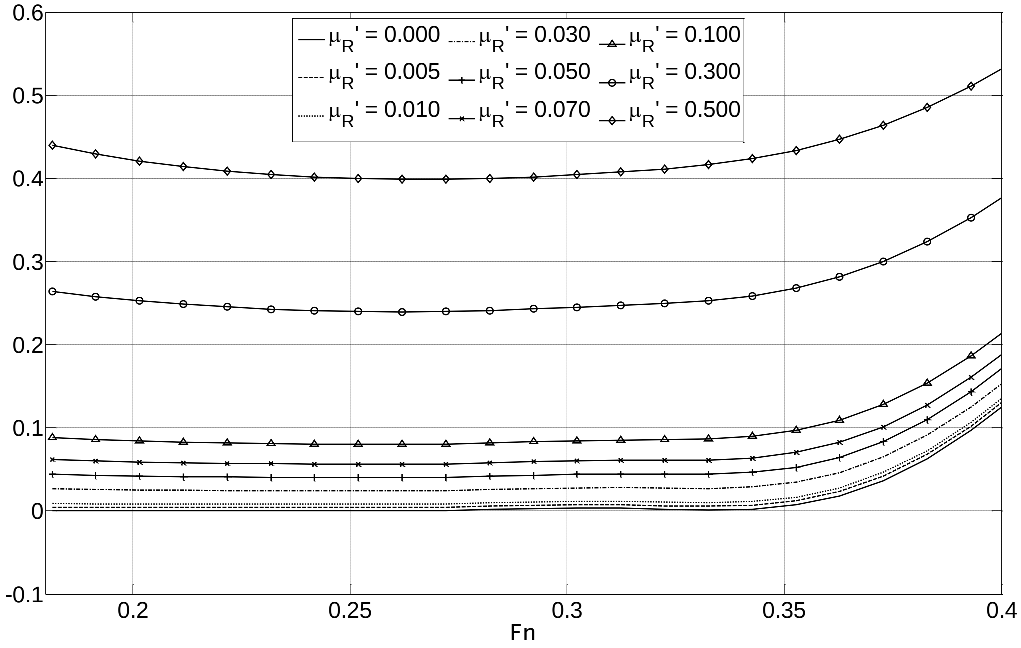

Figure 45 C_r for an ellipsoid submerged to d_e/c_e =0.5 at low speeds

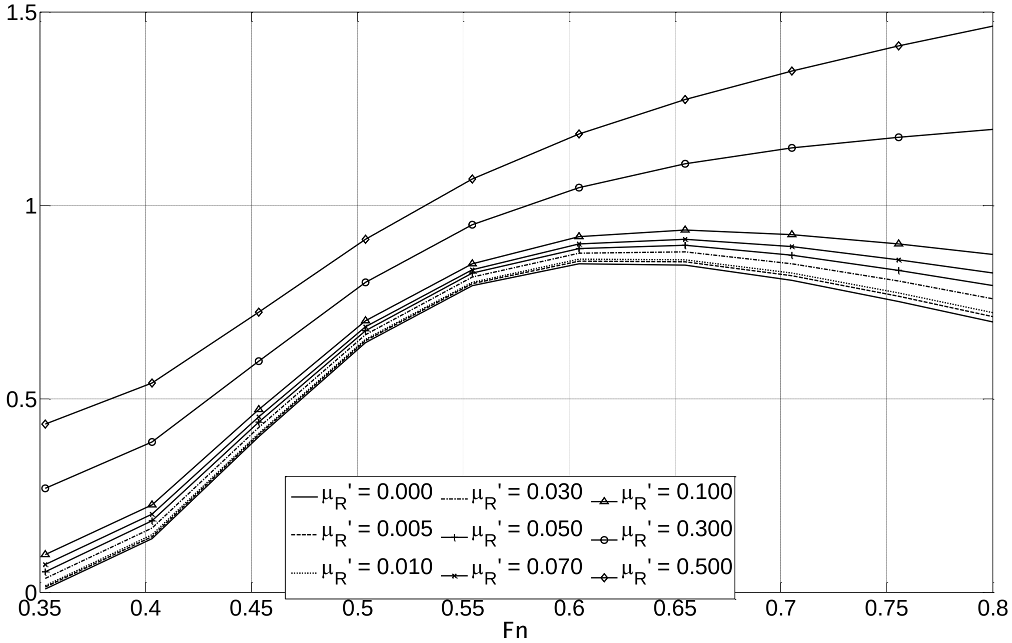

Figure 46 C_r for an ellipsoid submerged to d_e/c_e =0.5 at high speeds

6.1.2 Range of the damping coefficient for a bluff body

A sphere with diameter $D_s = 1$ is submerged to $d_s/R_s = (1.1, 2.0)$. The Froude number is calculated with the diameter as the characteristic length and resistance coefficient with the radius as the characteristic length. It is clearly seen in Figure 47 that the resistance curve with a high damping coefficient such as $\mu_R' = 0.3$ and $\mu_R' = 0.5$ deviates from the general profile of the C_w curve for no damping and gives a proportionally higher resistance for low Froude numbers. It is also clear that $\mu_R' = 0.3$ and $\mu_R' = 0.5$ is distinctly different from the C_w curve for no damping at higher Froude numbers. It is also shown that after $Fn = 0.6$ only $\mu_R' < 0.01$ yields a C_w curve that follows the shape of the no damping curve.

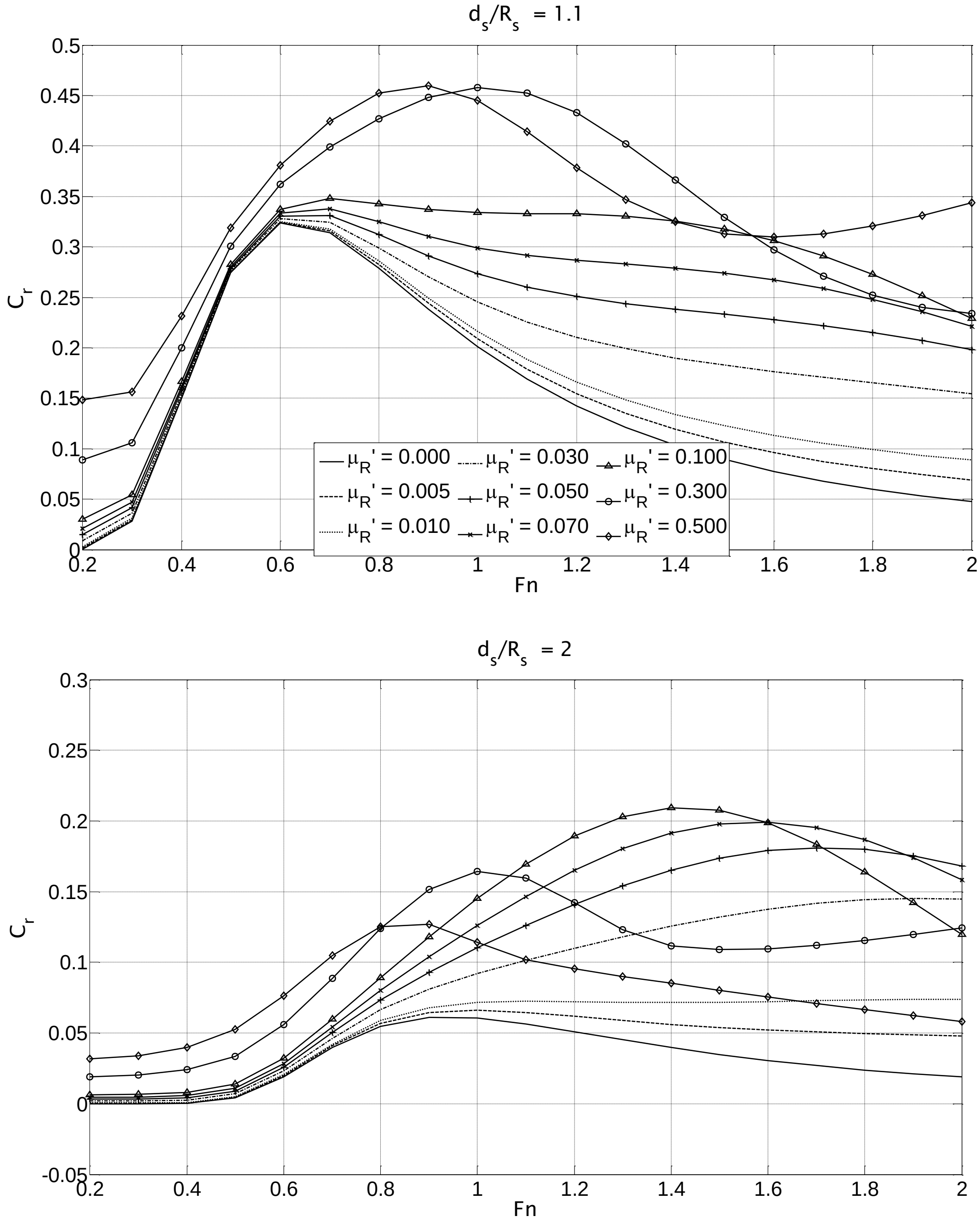

Figure 47 C_w for the submerged sphere for different values of μ_R'

From this, it is likely that for $Fn < 0.6$ μ_R' should be less or equal to 0.1 and for $Fn > 0.6$ μ_R' should be less or equal to 0.01 for a bluff body such as the sphere. This applies both to shallow and deep submersion of the sphere.

6.1.3 Summary on the range of the damping coefficient

A suitable range for the submerged ellipsoid is shown in Table 15 and the range for the sphere is shown in Table 16.

Table 15 Ellipsoid range of μ_R'

$d_e/2a_e$	$\mu_R' \leq$	$Fn \leq$
0.1241	0.1	0.4
0.1608	0.1	0.8
0.2462	0.1	0.8

Table 16 Sphere range of μ_R'

d_s/R_s	$\mu_R' \leq$	$Fn \leq$
1.1	0.10	0.6
1.1	0.01	2.0
2.0	0.10	0.6
2.0	0.01	2.0

6.2 Comparisons with experiments

The method shows good comparison with existing numerical results as shown in the previous chapter however the question remains whether the added damping factor can better capture some of the physical phenomena that a totally inviscid model discards. To determine this, results from the present method must be compared with experiments. There is a limited amount of experimental data available for fully submerged shapes. To the author's knowledge there are no results published for a fully submerged sphere. This is likely to be because of the limited resemblance between a sea going vessel and a sphere, but there is on-going work into the topic at the University of Southampton where results for a surface piercing sphere can be found in James at al. (2013).

6.2.1 Wave profile

It has been showed that the wave profile decays with distance in Figure 40. Conventional potential flow is somewhat lacking in determining the wave elevation on the hull and sometimes it overestimates the stern wave. By more correctly estimating the wave elevation on the hull the pressure on the hull could be more accurately determined. So the wave profile along a Wigley hull determined using thin ship theory. The wave elevation on the hull for different damping coefficients is shown in Figure 48 to Figure 50. From Figure 48 to Figure 50 it is clear that the damping parameter does not dampen the wave close to the hull and that in fact it increases both the bow and stern wave. However thin-ship theory is known to give poor estimations of the wave elevation close to the hull and may not be the most suitable model to determine the wave elevation on the hull. A better accuracy compared to experimental results is achieved by Lee and Soni (2006) using a incompressible RANS based solver and a moving grid approach.

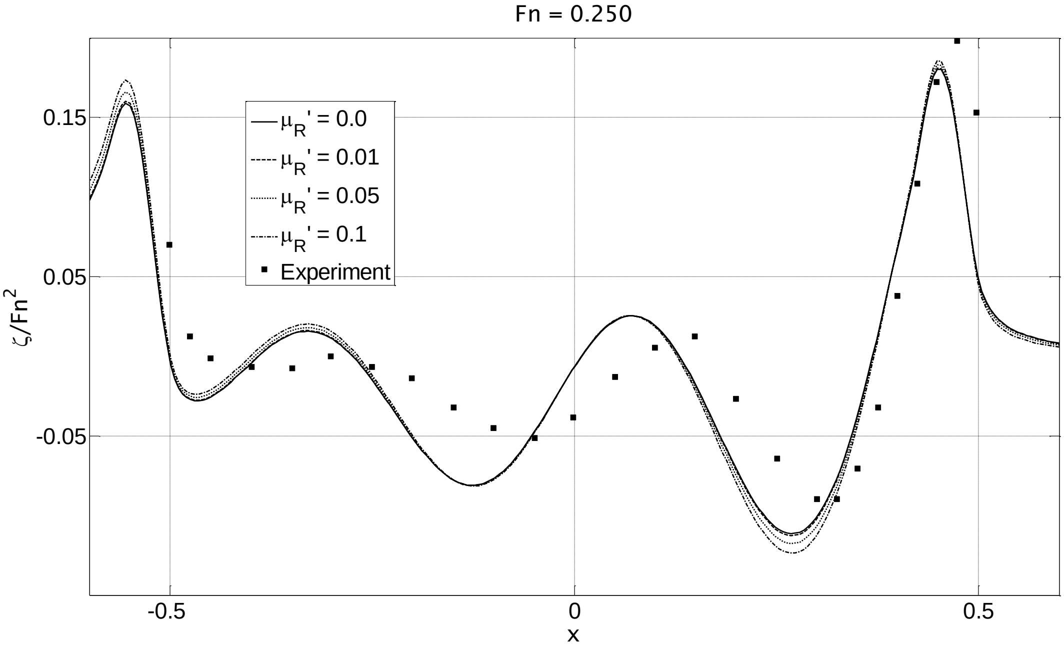

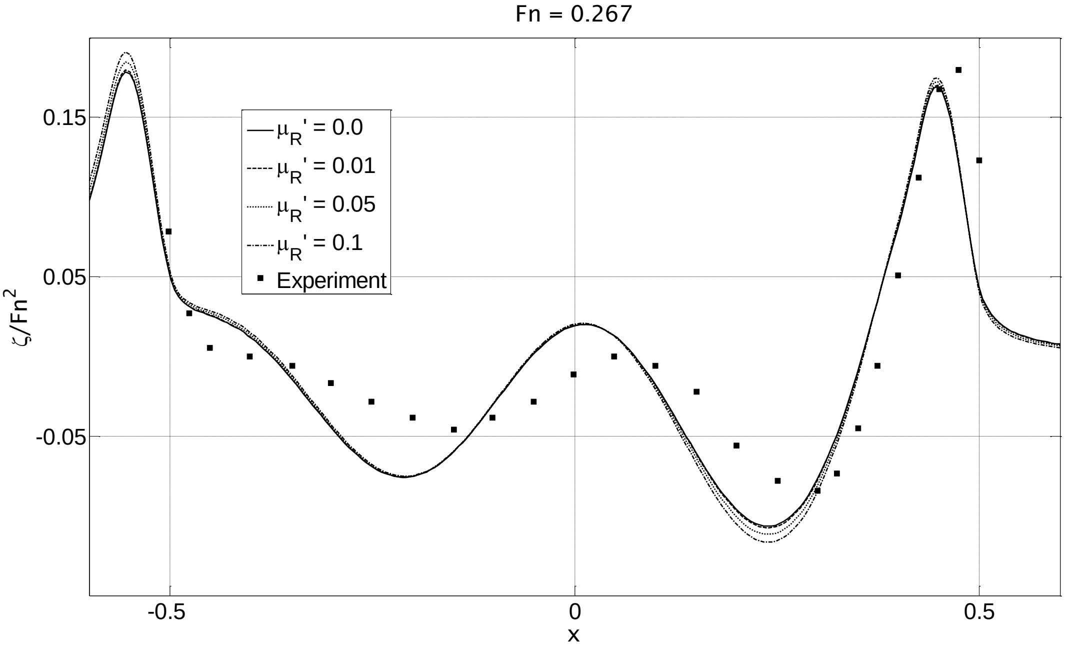

Figure 48 Wave elevation along the Wigley hull at $Fn = 0.25$ and $Fn = 0.267$

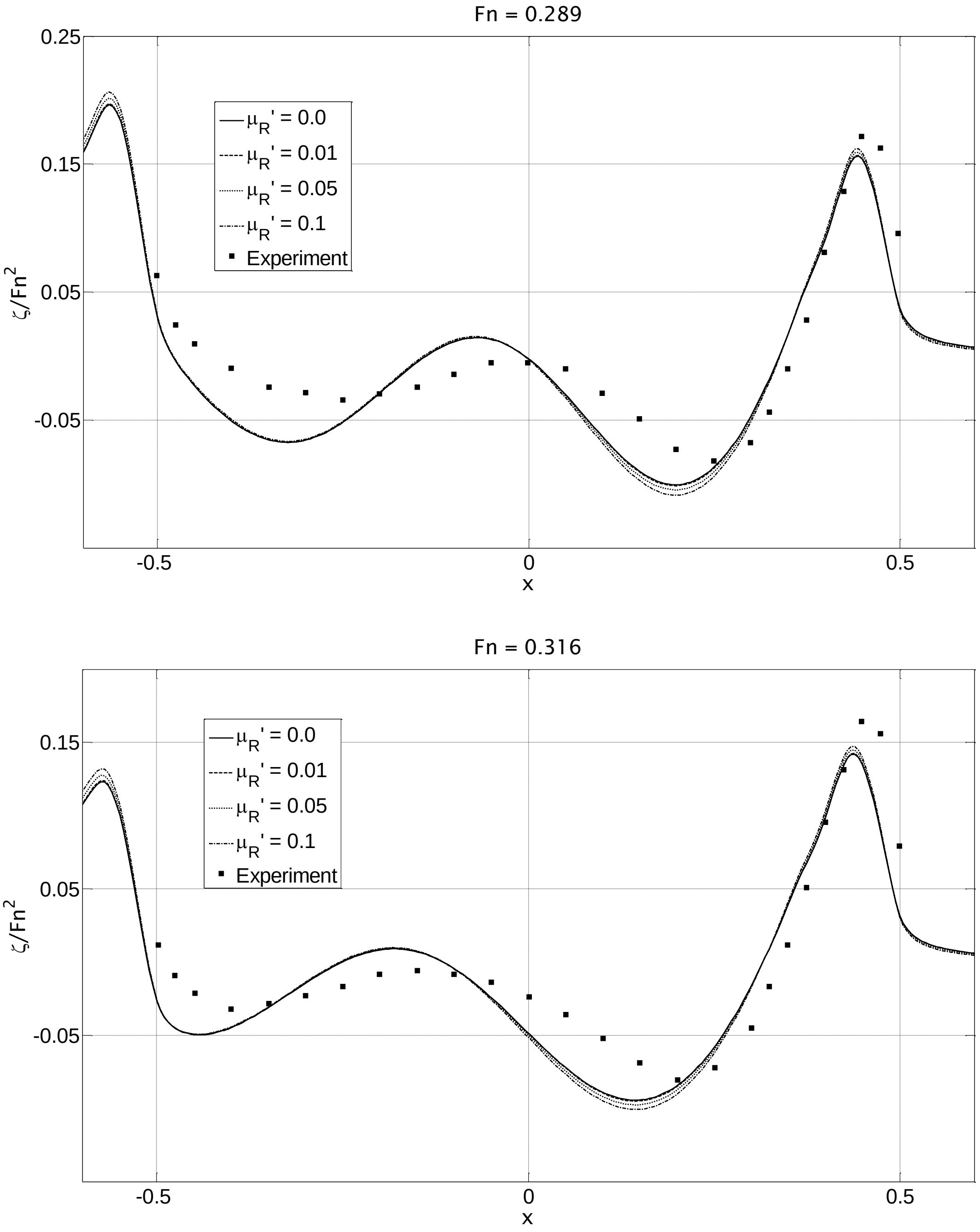

Figure 49 Wave elevation along the Wigley hull at $Fn = 0.289$ and $Fn = 0.316$

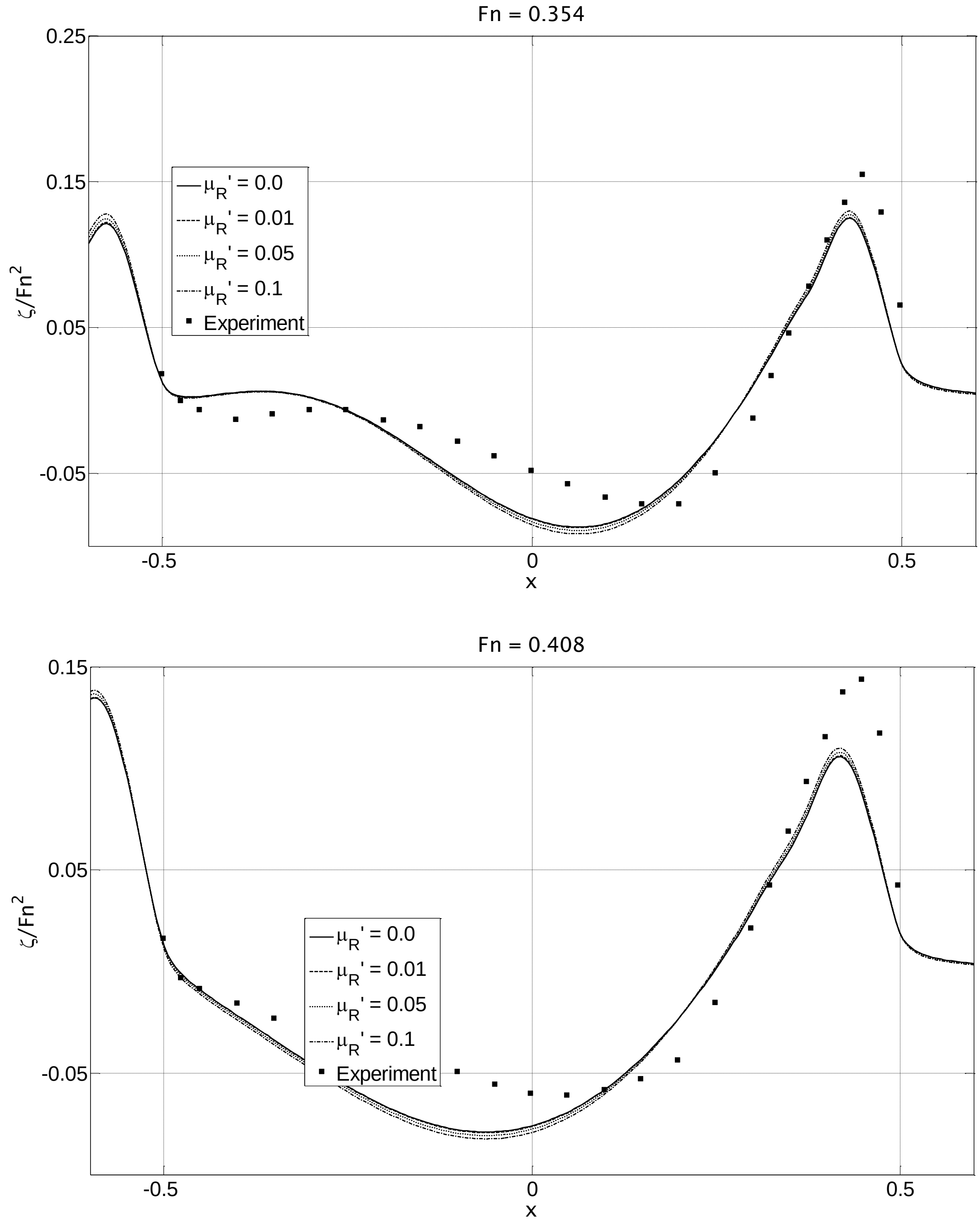

Figure 50 Wave elevation along the Wigley hull at $Fn = 0.354$ and $Fn = 0.408$

6.2.2 Wave resistance

A comparison with the experimental results of Farell and Güven's (1973) for an ellipsoid is shown in Figure 51. Farell and Güven's (1973) have measured the residual resistance with a wake-survey and then subtracted it from the total measured resistance in order to obtain the wave resistance. C_r is determined using the focal distance c_e as the reference length and twice the focal distance for the Froude number. The results show that none of the resistances curves using the present method corresponds to the experimental results for all Froude numbers. But as the speed increases a higher damping coefficient gives a better result than an inviscid method. This could imply that μ_R' could depend on the Froude number.

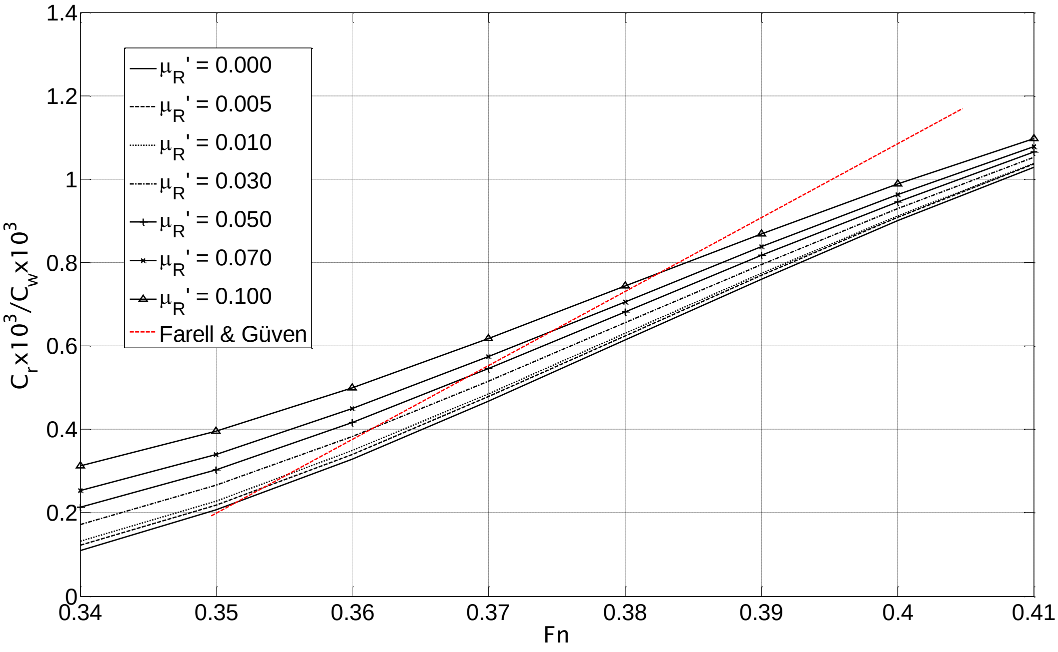

Figure 51 Submerged Ellipsoid d_e/c_e = 0.3232 and $2a_e/b_e$ = 10 compared with experiment

6.2.3 Residual resistance

To determine if the present method can be used to determine the residual resistance, results are compared with experiments conducted at the Berlin Towing tank (Weinblum et al, 1950), where the total resistance has been measured and the residual resistance coefficient has been determined by subtracting the Schoenherr (1932) frictional resistance coefficient from the total resistance coefficient. L_{ref} in (6.1) is the length of the major axis which is also used as the characteristic length for the Froude number. The residual resistance coefficient is seen in Figure 52 to Figure 54 for an ellipsoid with $2a_e/2b_e = 8$ submerged to different depths. From Figure 52 to Figure 54 it is clear that the current method can capture the behaviour of the residual resistance better than an inviscid method. But there is not a single value of μ_R' which would be suitable for all Froude number and depths. This implies that μ_R' is Froude- or possible Reynold number dependent.

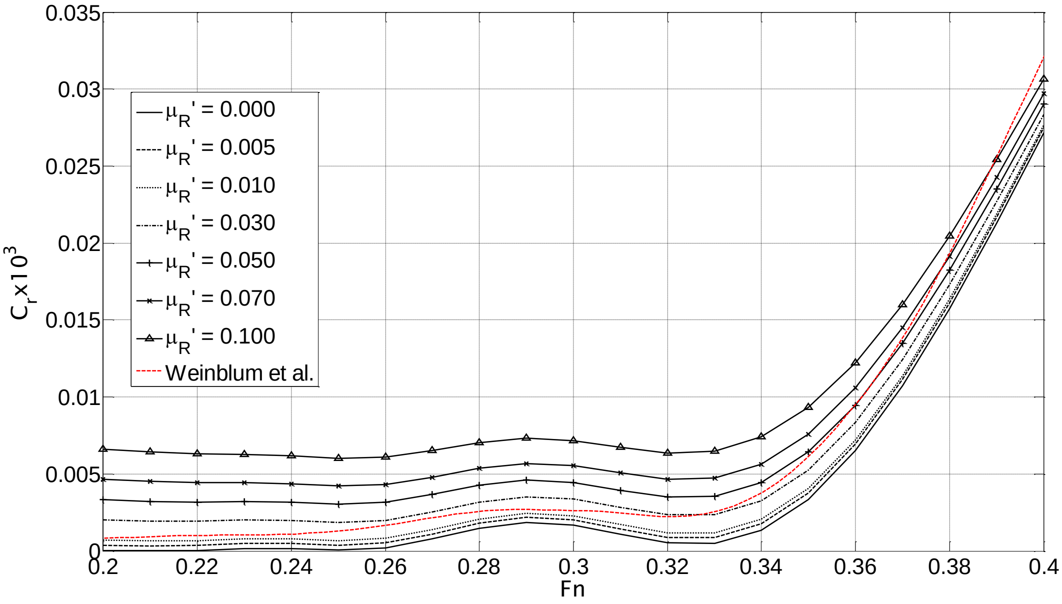

Figure 52 C_r for Ellipsoid with $d_e=2b_e$

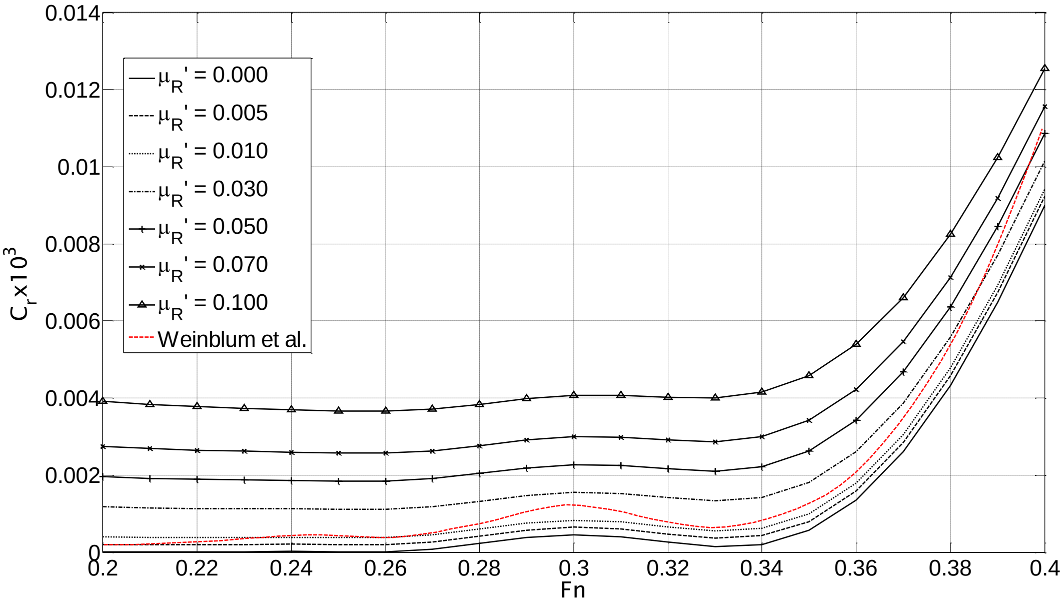

Figure 53 C_r for Ellipsoid with $d_e=3b_e$

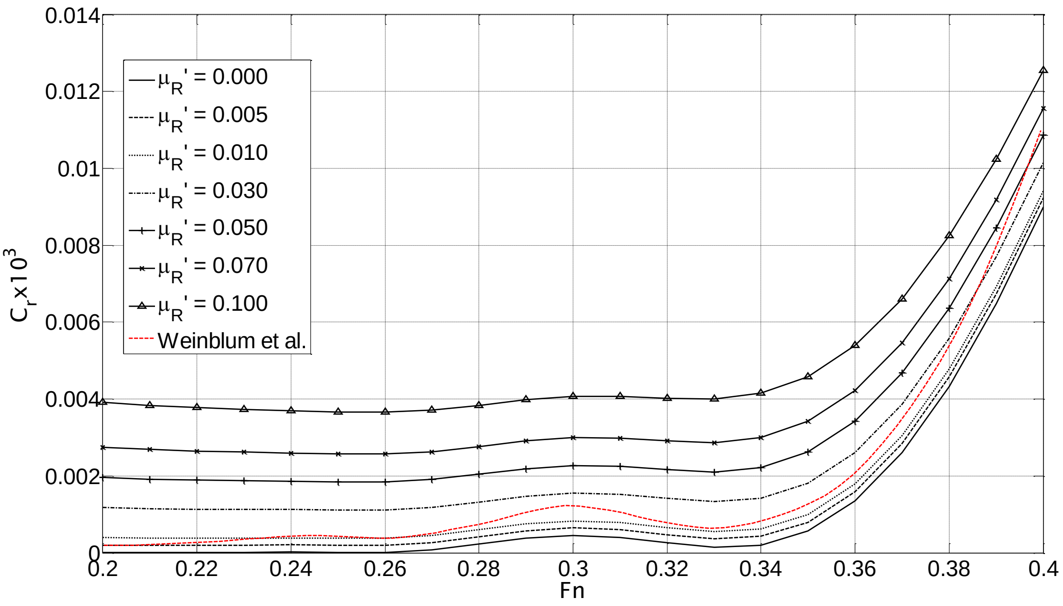

Figure 54 C_r for Ellipsoid with $d_e=4b_e$

7 Conclusions and recommendations

A numerical method is developed to determine the resistance of submerged bodies using a dissipative potential flow model. The problem is modelled using translating Neumann-Kelvin sources. Rayleigh damping is introduced into the potential flow model in order to capture the residual resistance. A dissipative 3D Green function is derived where the Laplace equation, free surface condition and the infinity condition are transformed using a Fourier transform to obtain the Havelock-Lunde formula of the double integral. The double integral is converted into two single integrals to improve the speed and accuracy of the computations. Thin ship theory is adopted to determine the wave pattern behind a Wigley hull. A panel method is implemented to determine the pressure distribution and wave pattern of fuller submerged bodies. The pressure is used to determine the wave- and residual resistance of an ellipsoid. The resistance coefficients are compared to numerical and experimental data from other sources. The present method shows good potential at determining the residual resistance. The main conclusions from this study are listed below.

7.1 Conclusions

- A new Green function is derived that is the first in 3D to include a damping parameter. This allows the assessment of the effects of the values of Rayleigh damping on the wave pattern and resistance. The general approach of obtaining the present Green function is well known. Some conventional methods retain the damping factor to simplify the derivation. However, at one stage or another they all set the damping to zero.

- The present method has proven to be successful in solving linear wave resistance problems. The calculation of the associated Green function and its derivatives have been verified against data from other sources based on different formulations. Results are generally in good agreement with existing numerical data for $\mu_R' = 0$.

- The present method is considerably slower than the method developed by Baar. This could be improved by a more efficient evaluation of the single integral such as approximating the integrals with series representation or applying a parallel computing scheme. The current evaluation scheme is particularly suitable to a parallel computing scheme since the integrands are evaluated separately in each point and not dependent on the value in any other point. However the order of magnitude of the speed is still much closer to that of potential flow models than full RANS based solvers.

- The Havelock expression of Green function is favoured because it is easily adapted to include damping. This may be because Havelock's original intention was to include such a damping coefficient. The main difficulty of the Havelock formulation, the lower variable integration limit, has not caused a problem because the single integrals have not been rewritten into Bessel functions. This may be the reason for the longer computational time.

- In theory, the inclusion of μ_R' allows for the direct integration of the double integral. However, in practise the numerical evaluation of the double integral is challenging and the method is considerably slower than the numerical evaluation of the corresponding single integrals. It is therefore recommended to apply a single integral formulation of Green function with damping.

- By including a damping parameter, there could be a possibility to better capture the decay of waves. The damping parameter has been shown to have some effect on the wave pattern. It has been proven that μ_R' has a damping effect on the wave pattern downstream of the ship that increases as μ_R' increases. However no such effect has been proven close to the ship.

- The inclusion of μ_R' seems to allow for the residual resistance to be modelled more accurately, at least at low speeds. No existing data for the residual resistance at larger speeds have been available, but a comparison with existing experimental data for the wave resistance could imply that the present method only captures the wave resistance at larger speeds. However, by including Rayleigh damping a better comparison to experimental data of C_w at larger speeds is obtained. However no single value of μ_R' can be determined. It is likely that μ_R' is Froude number or possible Reynolds number dependent. It is also possible that μ_R' depends on the shape of the submerged body.

- For an adequate description of the steady ship motion problem the three-dimensional features of the fluid flow and hull geometry cannot be neglected. Therefore Michell's thin ship theory is not suitable for evaluation of realistic hull shapes. For the method to be used on realistic hull forms the method must be extended to include fuller, surface piercing bodies. This will also allow for better evaluation of the method since there exists an abundance of both numerical and experimental results available for surface piercing ships.

- Conventional potential flow is somewhat lacking in determining the wave elevation on the hull and sometimes it overestimates the stern wave. This is especially important if the method is extended to include non-linear surface effects. Because of the apparent decay of the wave pattern due to μ_R' it was assumed that the wave profile along the hull would decay as well and that by including the damping term the pressure on a surface piercing body could be determined more accurately. However the expected decay of the stern wave has not been proved, instead μ_R' will increase both the bow and stern wave. However it is not clear if the inaccuracy in the wave elevation compared to experimental data from other sources is due to the use of thin-ship theory to model the wave pattern, since thin-ship theory is known to be less accurate than a panel method when it comes to modelling the wave elevation on the hull.
- The quantitative agreement between the experimental results and theoretical predictions with varying μ_R' shows the method has good potential, although there is a limited amount of comparative data available. Comparisons with more experimental results would have been favoured but it has not been possible due to the lack of experimental data for fully submerged bodies.

7.2 Future research

Due to the fundamental nature of this research project, it is a stepping stone for future work which should aim at making this model applicable to realistic hull forms.

7.2.1 Validations

There is a limited amount of data available for fully submerged shapes. This could be because the shapes and their behaviour are fairly known or because the most commonly fully submerged sea vessel is the submarine for which, due to its nature as a military vessel, few results tend to be published.

To determine the suitable values of μ_R' data from other sources are needed. It would be beneficial with more available experimental or RANS equations based data regarding fully submerged bodies. Since this method does not capture the total resistance the comparison data must separate the friction resistance from the total resistance.

7.2.2 Surface piercing body

This research is a first step towards developing a potential flow based model to determine the resistance of ships. As such it must be able to evaluate the resistance of surface piercing bodies. Usually this is done by including the line integral in (3.59).

7.2.3 Non-linear effects

This works aims to assess the effect of damping in the resistance calculation. To better assess the effects of μ_R' non-linear effects could be included in the model.

The method could be improved to at least incorporate partial non-linear surface effects. Partial non-linear surface means that free panels are located on the hull and they change with the wave elevation on the hull but the boundary conditions do not change.

A full non-linear model would give better accuracy but it seems wiser as a first step to evaluate the influence of a partial non-linear free surface before moving on to a fully non-linear free surface if needed, because a fully non-linear model will increase the computation time.

References

Aanesland, V. (1986). *A Theoretical and Numerical Study of Ship Wave Resistance.* Thesis (Ph.D.), The University of Trondheim.

Abramowitz, M.,Stegun, I.A. (eds.) (1964) *Handbook of Mathematical Functions with Formulas, Graphs and Mathematical Tables,* New York: Dover Publications.

Airy, G. (1841) Tides and Waves. *Encyclopaedia metropolitana (1817–1845), Mixed Sciences,* Vol **3**.

Anderson, J.D. (1997) *A History of Aerodynamics,* Cambridge, Cambridge University Press.

Andrew, R.N., Baar, J.J. & Price, W.G. (1988) Prediction of Ship Wavemaking Resistance and Other Steady Flow Parameters Using Neumann-Kelvin Theory. *Transactions of the Royal Institution of Naval Architects,* Vol **130,** pp. 119-133.

Argyris, J.,Patton, P. (1966) Computer Oriented Research in a Universitymilieu. *Applied Mechanics Reviews,* Vol **19,** pp. 1029-1039.

Baar, J.J.M. (1986). *A Three-Dimensional Linear Analysis of Steady Ship Motion in Deep Water.* Thesis (Ph.D.), Brunel University.

Baar, J.J.M.,Price, W.G. (1988a) Developments in the Calculation of the Wavemaking Resistance of Ships. *Proceedings of the Royal Society of London. Series A,* Vol **416,** pp. 115-147.

Baar, J.J.M.,Price, W.G. (1988b) Evaluation of the Wavelike Disturbance in the Kelvin Wave Source Potential. *Journal of Ship Research,* Vol **32,** pp. 44-53.

Bal, S. (2008) Prediction of Wave Pattern and Wave Resistance of Surface Piercing Bodies by a Boundary Element Method. *International Journal for numerical methods in fluids,* Vol **56,** pp. 305-329.

Ball, W.W.R. (1960) *A Short Account of the History of Mathematics,* New York, Dover Publications.

Belibassakis, K., Feurer, C., Gerostathis, T., Ginnis, A.A., Kaklis, P., Karigiannis, J., Kostas, K., Mourkogiannis, D., Politis, C.,Theodoulides, A. (2010) *Software Module for Isogeometric BEM Wave Resitance Calculations for an Immersed Ellipsoid*. No. 2.2.

Belibassakis, K.A., Gerostathis, T.P., Kostas, K.V., Politis, C.G., Kaklis, P.D., Ginnis, A.I.,Feurer, C. (2013) A BEM-Isogeometric Method for the Ship Wave-Resistance Problem. *Ocean Engineering,* Vol **60,** pp. 53-67.

Bertram, V. (2000) *Practical Ship Hydrodynamics,* Oxford, Butterworth-Heinemann.

Bessho, M. (1964) On the Fundamental Function in Theroy of the Wave-Making Resitance of Ships. *Memoirs of the Defense Acadamy, Japan,* Vol **4,** pp. 99-119.

Brard, R. (1972) The Representation of a Given Ship Form by Singularity Distributions When the Boundary Condition on the Free Surface Is Linearized. *Journal of Ship Research,* Vol **16,** pp. 79-92.

Breunig, P. (1996) The 8000-Year-Old Dugout Canoe from Dufuna (Ne Nigeria). *In:* Pwiti, G. and Soper, R. (eds.) *10th Congress of the Pan African Association for Prehistory and related Studies.* Harare: University of Zimbabwe Publications.

Chen, C.Y.,Noblesse, F. (1983) Comparison between Theoretical Predictions of Wave Resistance and Experimental Data for the Wigley Hull. *Journal of Ship Research,* Vol **27,** pp. 215-226.

Chen, X.B., Diebold, L. & Doutreleau, Y. (2001) New Green-Function Method to Predict Wave-Induced Ship Motions and Loads. *Twenty-Third Symposium on Naval Hydrodynamics.* Val de Reuil, France: The National Academies Press.

Demanche, J.F. (1981) Potential of a Moving Pulsating Source. *Ptoceedings of the 3rd International Conference on Numerical Ship Hydrodynamics.* Paris, France.

Denayer, A. (1978) Automatic Generation of Finite Element Meshes. *Computers & Structures,* Vol **9,** pp. 359-364.

Diken, O., Du, S.X., Hudson, D.A.,Temarel, P. (2004) Calculation of Steady-State Ship Wave Patterns Using a General Rankine Source Method. *Proceedings of 14th International Offshore Polar Engineering Conference.* Toulon, France: The International Society of Offshore and Polar Enginners.

Doctors, L.,Beck, R. (1987a) Convergence Properties of the Neumann-Kelvin Problem for a Submerged Body. *Journal of Ship Research,* Vol **31**.

Doctors, T.,Beck, R. (1987b) Numerical Aspects of the Neumann-Kelvin Problem. *Journal of Ship Research,* Vol **31,** pp. 1-13.

Dong, X., Wang, Y., Li, Y.,Zeng, L. (2013) Numerical Simulation of Underwater Ellipsoid Motion near Free Surface. *Applied Mechanics and Materials,* Vol **275,** pp. 502-507.

Eggers, K. (1962) Über Die Ermittlung Des Wellenwiderstandes Eines Schiffsmodells Durch Analyse Seines Wellensystems. *Schiffstechnick Bd,* Vol **9**.

Eggers, K., Sharma, S. & Ward, L. (1967) An Assessment of Some Experimental Methods for Determining the Wavemaking Characteristics of a Ship Form. *Transactions of the Institution of Naval Architects and Marine Engineers,* Vol **75,** pp. 112-144.

Eng, K.,Hu, P.N. (1963) *Wave-Resistance Reduction of near-Surface Bodies*. Davidson Laboratory,No. 933.

Euler, L. (1755a) Continuation Des Recherches Sur La Théorie Du Mouvement Des Fluides. *Mémoires de l'académie des sciences de Berlin,* Vol **11,** pp. 1757.

Euler, L. (1755b) Principes Généraux De L'état D'équilibre Des Fluides. *Mémoires de l'académie des sciences de Berlin,* Vol **11,** pp. 1757.

Euler, L. (1755c) Principes Généraux Du Mouvement Des Fluides. *Mémoires de l'académie des sciences de Berlin,* Vol **11,** pp. 274–315.

Euler, L. (1756) Principa Motus Fluidorum. *Novi commentarii academiae swcientiarum Petropolitanae***,** pp. 271-311.

Faltinsen, O.M. (2006) *Hydrodynamics of High-Speed Marine Vehicles,* Cambridge, Cambridge University Press.

Farell, C. (1973) On the Wave Resistance of a Submerged Spheroid. *Journal of Ship Research,* Vol **17,** pp. 1-11.

Farell, C.,Güven, O. (1973) On the Experimental Determination of the Resistance Components of a Submerged Spheroid. *Journal of Ship Research,* Vol **17**.

Froude, W. 1868. *RE: Observations and Suggestions on the Subject of Determining by Experiment the Resistance of Ships.* Type to Correpsondence with the Admirality. Memo. To E.J. Reed, C.C.O.T.N.

Froude, W. (1877) Experiments Upon the Effect Produced on the Wave-Making Resitance of Ships by Length of Parallel Middle Body. *Transactions of the Instituion of Naval Architects,* Vol **18,** pp. 77-97.

Froude, W., Abell, W., Gawn, R.,Duckworth, A. (1955) *The Papers of William Froude, Ma, Ll. D., Frs, 1810-1879,* London, Institution of Naval Architects.

Fürth, M. (2011). *Determining the Pressure Distubution on Submerged 2d Bodies Using Dissipative Potential Flow.* Thesis (M.sc.), Royal Institute of Technology, KTH.

Fürth, M., Tan, M. & Chen, Z.-M. (2013) Determining Wave Resistance Using a Dissipative Potential Flow Model. *Proceedings of The 23rd International Ocean and Polar Engineering Conference.* Anchorage, United States of America: International Society of Offshore and Polar Engineers.

Green, G. (1828) An Essay on the Application of Mathematical Analysis to the Theories of Electricity and Magnetism. *Privately published by T. Wheelhouse*.

Harvald, S.A. (1983) *Resistance and Propulsion of Ships,* New York, John Wiley & Sons Inc.

Havelock, T.H. (1928) Wave Resistance. *Proceedings of the Royal Society of London. Series A,* Vol **118,** pp. 24-33.

Havelock, T.H. (1932) The Theory of Wave Reistance. *Proceedings of the Royal Society of London Series A,* Vol **138,** pp. 339-348.

Havelock, T.H. (1934a) The Calculation of Wave Resistance. *Proceedings of the Royal Society of London. Series A,* Vol **144,** pp. 514-521.

Havelock, T.H. (1934b) Wave Patterns and Wave Resitance. *Transactions of the Instituion of Naval Architects,* Vol **74,** pp. 340.

Havelock, T.H. (1935) Ship Waves: The Relative Efficiency of Bow and Stern. *Proceedings of the Royal Society of London. Series A,* Vol **149,** pp. 417-426.

Hearn, G. (1977) Alternative Methods of Evaluating Green's Function in Three-Dimensional Ship-Wave Problems. *Journal of Ship Research,* Vol **21,** pp. 89-93.

Hess, J. (1990) Panel Methods in Computational Fluid Dynamics. *Annual Review of Fluid Mechanics,* Vol **22,** pp. 255-274.

Hess, J.L. (1975) Review of Integral-Equation Techniques for Solving Potential-Flow Problems with Emphasis on the Surface-Source Method. *Computer Methods in Applied Mechanics and Engineering,* Vol **5,** pp. 145-196.

Hess, J.L.,Smith, A.M.O. (1964) Calculation of Non-Lifting Potential Flow About Arbitrary Three-Dimensional Bodies. *Journal of Ship Research,* Vol **8,** pp. 22-44.

Hoff, J.R. (1990). *Three-Dimensional Green Function of a Vessel with Forward Speed in Waves.* Thesis (Ph.D.), The University of Trondheim.

Hogben, N. (1972) Automated Recording and Analysis of Wave Patterns Behind Towed Models. *Transactions of the Royal Institution of Naval Architects,* Vol **114,** pp. 127-153.

Holtrop, J.,Mennen, G. (1982) An Approximate Power Prediction Method. *International Shipbuilding Progress,* Vol **29,** pp. 166-170.

Huan, J.C.,Huang, T.T. (2007) Surface Ship Total Resistance Prediction Based on a Nonlinear Free Surface Potential Flow Solver and a Reynolds-Averaged Navier-Stokes Viscous Correction. *Journal of Ship Research,* Vol **51,** pp. 47-64.

Hughes, G. (1954) Friction and Form Resistance in Turbulent Flow, and a Proposed Formulation for Use in Model and Ship Correlation. *Transactions of Institution of Naval Architects,* Vol **96**.

Inui, T. (1954) *Japanese Developments on the Theory of Wave-Making and Wave Resistance*. Skipsmodelltankens meddelelse,No. 34.

James, M., Turnock, S.R. & Hudson, D.A. (2013) Flow Past a Sphere at the Free-Surface Using Urans. *Numerical Towing Tank Symposium.* Duisburg, Germany.

Janson, C.-E.,Spinney, D. (2004) A Comparison of Four Wave Cut Analysis Methods for Wave Resistance Prediction. *Ship Technology Research,* Vol **51,** pp. 173-184.

Joseph, D.D. (2006) Potential Flow of Viscous Fluids: Historical Notes. *International Journal of Multiphase Flow,* Vol **32,** pp. 285-310.

Joseph, D.D., Liao, T. & Hu, H. (1993) Drag and Moment in Viscous Potential Flow. *European Journal of Mechanics Series B Fluids,* Vol **12,** pp. 97-97.

Kajitani, H., Miyata, H., Ikehata, M., Tanaka, H., Adachi, H., Namimatsu, M.,Ogiwara, S. (1983) The Summary of the Cooperative Experiment on Wigley Parabolic Model in Japan. *International Towing Tank Conference.* Varma, Bulgaria.

Kelvin (Thomson), W. (1887) On Ship Waves. *Proceedings of the Institution of Mechanical Engineers,* Vol **38,** pp. 409-434.

Kinoshita, M.,Inui, T. (1953) Wave-Making Resistance of a Submerged Spheroid, Ellipsoid and a Ship in a Shallow Sea. *Journal of Zosen Kiokai,* Vol **75,** pp. 119-135.

Kreyszig, E. (2006) *Advanced Engineering Mathematics,* New York, John Wiley & Sons

Kumar, M.S.,Philominathan, P. (2011) Bringing out Fluids Experiments from Laboratory to in Silico–a Journey of Hundred Years. *American Journal of Computational Mathematics,* Vol **1,** pp. 271.

Lagrange, J.L. (1781) Mémoire Sur La Théorie Du Mouvement Des Fluides. *Nouveaux mémoires de l'Académie royale des sciences et belles-lettres de Berlin,* Vol **4,** pp. 695-748.

Lalli, F., Campana, E. & Bulgarelli, U. (1992) Ship Waves Computations. *The Seventh International Workshop on Water Waves and Floating Bodies.* Val de Reuil, France.

Lalli, F., Di Felice, F., Esposito, P.,Moriconi, A. (1999) Some Remarks on the Accuracy of Wave Resistance Determination from Wave Measurements. *Twenty-Second Symposium on Naval Hydrodynamics.* Washington, D.C., United States of America: National Academies Press.

Lamb, H. (1926) On Wave Resistance. *Proceedings of the Royal Society of London. Series A,* Vol **111,** pp. 14-25.

Lamb, H. (1945) *Hydrodynamics,* New York, Dover.

Larsson, L.,Eliasson, R. (2000) *Principles of Yacht Design,* London, Adlard Coles Nautical.

Lauro, L.,Miranda, S. (1987) Anlysis and Comparisons on the Form Factor Determination According to ITTC 78 Method. *International Towing Tank Conference.* Tokyo, Japan.

Lee, S.,Soni, B. (2006) The Derivation and the Computation of Kinematic Boundary Condition. *Mathematics and Computers in Simulation,* Vol **71,** pp. 62-72.

Letcher, J.S., Marshall, J.K., Oliver, J.C.I.,Salvesen, N. (1987) Stars and Stripes. *Scientific American,* Vol **257,** pp. 34-40.

Lunde, J.K. (1951) *On the Linearized Theory of Wave Resistance for Displacement Ships in Steady and Accelerated Motion*, Transactions of The Society of Naval Architects and Marine Engineers.

Marr, G. (1992) Improvments in the Computation of the Wave Function in the Neumann-Kelvin Wave Problem. *11th Australasian Fluid Mechanics Conference.* Hobart, Australia.

Marr, G.,Jackson, P.S. (1999) Some Improvements and Comparisons in the Solution of the Neumann-Kelvin Problem. *Journal of Ship Research,* Vol **43,** pp. 170-179.

Mccarthy, J.H. (1985) *Collected Experimental Resistance Component and Flow Data for Three Surface Ship Model Hulls*. Department of the Navy David Taylor Model Basin,No. DTNSRDC-85/011.

Michell, J.H. (1898) The Wave-Resistance of a Ship. *Philosophical Magazine,* Vol **45,** pp. 106-123.

Milne-Thomson, L.M. (1962) *Theoretical Hydrodynamics,* New York, Dover Publications.

Miyata, H. (1996) Time Marching CFD Simulation for Moving Boundary Problems. *Twenty First Symposium on Naval Hydrodynamics.* Trondheim, Norway.

Molland, A.F., Turnock, S.R. & Hudson, D.A. (2011) *Ship Resistance and Propulsion Prractical Estimation of Ship Propulsive Power,* Cambridge, Cambridge University Press.

Monacella, V. (1966) The Disturbance Due to a Slender Ship Oscillating in Waves in a Fluid of Finite Depth. *Journal of Ship Research,* Vol **10,** pp. 242-252.

Monaghan, J.J. (1988) An Introduction to SPH. *Computer Physics Communications,* Vol **48,** pp. 89-96.

Moore, G.E. (1965) Cramming More Components onto Integrated Circuits. *Electronics Magazine***,** pp. 4.

Nakatake, K. (1966) On the Wave Pattern Created by Singular Points. *Journal of the society of Naval Architects of West Japan,* Vol **31,** pp. 1-19.

Nakos, D.E. (1991) Transverse Wave Cut Analysis by a Rankine Panel Method. *6th International Worskshop on Water Waves and Floating Bodies.* Woods Hole, United States of America.

Nakos, D.E.,Sclavounos, P.D. (1990) On Steady and Unsteady Ship Wave Patterns. *Journal of Fluid Mechanics,* Vol **215,** pp. 263-288.

Nakos, D.E.,Sclavounos, P.D. (1994) Kelvin Wakes and Wave Resistance of Cruiser-and Transom-Stern Ships. *Journal of Ship Research,* Vol **38,** pp. 9-29.

Newman, J. (1970) Applications of Slender-Body Theory in Ship Hydrodynamics. *Annual Review of Fluid Mechanics,* Vol **2,** pp. 67-94.

Newman, J. (1985) The Evaluation of Free-Surface Green Functions. *4th Conference on Numerical Ship Hydrodynamics.* Washington D.C., United States of America.

Newman, J.N. (1987a) Evaluation of the Wave-Resistance Green Function: Part 2: The Single Integral on the Centerplane. *Journal of Ship Research,* Vol **31,** pp. 145-150.

Newman, J.N. (1987b) Evaluation of the Wave-Resitance Green Function. Part 1: The Double Integral. *Journal of Ship Research,* Vol **31,** pp. 79-90.

Nilsson, R.P. (ed.) (2010) *Sjöfartens Bok,* Gothenburg: Svensk Sjöfarts Tidings Förlag AB.

Noblesse, F. (1981) Alternative Integral-Representations for the Green-Function of the Theory of Ship Wave Resistance. *Journal of Engineering Mathematics,* Vol **15,** pp. 241-265.

Noblesse, F., Delhommeau, G., Huang, F.,Yang, C. (2010) Practical Mathematical Representation of the Flow Due to a Distribution of Sources on a Steadily Advancing Ship Hull. *Journal of Engineering Mathematics***,** pp. 1-26.

Noblesse, F., Delhommeau, G., Kim, H.,Yang, C. (2009) Thin-Ship Theory and Influence of Rake and Flare. *Journal of Engineering Mathematics,* Vol **64,** pp. 49-80.

Noblesse, F., Hendrix, D. & Barnell, A. (1989) The Slender-Ship Approximation: Comparison between Experimental Data and Numerical Predictions. *Journees de l'Hydrodynamique***,** pp. 175-187.

Ortigosa, I., López, R. & García, J. (2009) Prediction of Total Resistance Coefficients Using Neural Networks. *Journal of Maritime Research,* Vol **6,** pp. 15-26.

Pegoraro, V.,Slusallek, P. (2011) On the Evaluation of the Complex-Valued Exponential Integral. *Journal of Graphics, GPU, and Game Tools,* Vol **15,** pp. 183-198.

Percival, S., Hendrix, D. & Noblesse, F. (2001) Hydrodynamic Optimization of Ship Hull Forms. *Applied Ocean Research,* Vol **23,** pp. 337-355.

Peters, A.S. (1949) A New Treatment of the Ship Wave Problem. *Communications on Pure and Applied Mathematics,* Vol **2,** pp. 123-148.

Ponizy, B., Guilbaud, M. & Ba, M. (1998) Numerical Computations and Integrations of the Wave Resistance Green's Function. *Theoretical and Computational Fluid Dynamics,* Vol **12,** pp. 179-194.

Price, W.,Tan, M. (1987) A Preliminary Investigation into the Forces Acting on Submerged Body Appendages. *International Conference on Ship Manoeuvrability-Prediction and Achievement.* London, United Kingdom: The Royal Instituion of Naval Architects.

Price, W., Wang, Y. & Baar, J. (1989) Influence of Fluid Density on Steady Ship Wave Characteristics. *Seventeenth Symposium on Naval Hydrodynamics.* The Hague, The Netherlands: The National Academies Press.

Priestley, H.A. (2003) *Introduction to Complex Analysis,* Oxford, Oxford University Press.

Råde, L.,Westergren, B. (2004) *Mathematics Handbook for Science and Engineering,* Lund, Studentlitteratur.

Raven, H.C. (1991) Adequacy of Free Surface Conditions for the Wave Resitance Problem. *Eighteenth Symposium on Naval Hydrodynamics.* Ann Arbor, United States of America: The National Academies Press.

Raven, H.C. (1996). *A Solution Method for the Nonlinear Ship Wave Resistance Problem.* Thesis (Ph.D.), Technische Universiteit Delft.

Raven, H.C.,Prins, H.J. (1998) Wave Pattern Analysis Applied to Nonlinear Ship Wave Calculations. *13th International Workshop on Water Waves and Floating Bodies.* Alphen aan den Rijn, The Netherlands: Maritime Research Institute Netherlands.

Rayleigh (Strutt), J.W. (1877) *Theory of Sound (Two Volumes),* London, Macmillian and Co.

Saad, T. (2008-2011) *"How Euler Derived the Momentum Equations".* [Online]. Available: http://pleasemakeanote.blogspot.com/2010/07/how-euler-derived-momentum-equations.html [Accessed 31/8 2011].

Schenkman, L. (2009) *Computers Faster Only for 75 More Years* [Online]. Live Science. Available: http://www.livescience.com/5756-computers-faster-75-years.html [Accessed 21/03 2012].

Schoenherr, K.E. (1932) On the Resistance of Flat Surfaces Moving through a Fluid. *Transactions of the Society of Naval Architects and Marine Engineering,* Vol **40,** pp. 279-313.

Sharma, S.D. (1963) A Comparison of the Calculated and Measured Free-Wave Spectrum of an Inuid in Steady Motion. *International Seminar on Theoretical Wave-Resistance.* Ann Arbor, United States of America.

Sharma, S.D. (1966) An Attempted Application of Wave Analysis Techniques to Achieve Bow-Wave Reduction. *Sixth Symposium on Naval Hydrodynamics.* Washington D.C., United States of America.

Smith, A.,Pierce, J. (1958) *Exact Solution of the Neumann Problem: Calculation of Non-Circulatory Plane and Axially Symmetric Flows About or within Arbitrary Boundaries*. Douglas Aircraft Company,No. ES-26988.

Stokes, G.G. (1847) On the Theory of Oscillatory Waves. *Trans Cambridge Philos Soc,* Vol **8,** pp. 441-473.

Stokes, G.G. (1851) On the Effect of the Internal Friction of Fluids on the Motion of Pendulums. *Transactions of the Cambridge Philosophical Society,* Vol **9,** pp. 8.

Tuck, E.O. (1989) The Wave Resitance Formula of J.H. Michell (1898) and Its Significance to Recent Research in Ship Hydrodynamics. *The Journal of the Australian Mathematical Society Series B,* Vol **30,** pp. 365-377.

Tuck, E.O.,Scullen, D.C. (2002) A Comparison of Linear and Nonlinear Computations of Waves Made by Slender Submerged Bodies. *Journal of Engineering Mathematics,* Vol **42,** pp. 255-264.

Tuck, E.O., Scullen, D.C. & Lazauskas, L. (1999a) *Sea Wave Pattern Evaluation*. Part 2 Report: Investigation of Accuracy, Applied Mathematics Department,The University of Adelaide,Report.

Tuck, E.O., Scullen, D.C. & Lazauskas, L. (1999b) *Sea Wave Pattern Evaluation*. Part 1 Report: Primary Code and Test Results (Surface Vessels), Applied Mathematics,The University of Adelaide,Report.

Tuck, E.O., Scullen, D.C. & Lazauskas, L. (2002) Wave Patterns and Minimum Wave Resistance for High-Speed Vessels. *24th Symposium on Naval Hydrodynamics.* Fukuoka, Japan.

Tursini, L. (1953) Leonardo Da Vinci and the Problems of Navigation and Naval Design. *Transactions of the institution of naval architects,* Vol **95,** pp. 97-102.

Ursell, F. (1984) Mathematical Note on the Fundamental Solution (Kelvin Source) in Ship Hydrodynamics. *IMA Journal of Applied Mathematics,* Vol **32,** pp. 335-351.

Ursell, F. (1988) On the Theory of the Kelvin Ship-Wave Source: Asymptotic Expansion of an Integral. *Proceedings of the Royal Society of London, Series A,* Vol **418,** pp. 81-93.

Uslu, Y.,Bal, S. (2008) Numerical Prediction of Wave Drag of 2-D and 3-D Bodies under or on a Free Surface. *Turkish Journal of Engineering and Environmental Sciences,* Vol **32**.

Vidal, J. (2007). CO2 Output from Shipping Twice as Much as Airlines. *The Guardian*, 3 March.

Wehausen, J.V.,Laitone, E.V. (1960) Surface Waves. *Encyclopaedia of Physics,* Vol **IX,** pp. 446-778.

Weinblum, G., Amtsberg, H. & Bock, W. (1950) *Tests on Wave Resitance of Immersed Bodies of Revolution*. Department of the Navy David Taylor Model Basin,No. AD827201.

Wigley, W.C.S. (1934) A Comparison of Experiment and Calculated Wave-Profiles and Wave-Resistances for a Form Having Parabolic Waterlines. *Proceedings of the Royal Society of London. Series A,* Vol **144,** pp. 144-159.

Wördenweber, B. (1980) *Volume Triangulation*. CAD Group,University of Cambridge,Report No. 110.

Wright, M.C.M. (2006) Green Function or Green's Function? *Nature Physics,* Vol **2,** pp. 646-646.

Wu, G.X. (1995) Radiation and Diffraction by a Submerged Sphere Advancing in Water Waves of Finite Depth. *Proceedings: Mathematical and Physical Sciences,* Vol **448,** pp. 29-54.

Appendix A

Determining Wave resistance Using a Dissipative Potential Flow model

By Mirjam Fürth, Mingyi Tan and Zhi-Min Chen

Proceedings of the Twenty-third (2013) International Offshore and Polar Engineering Conference, Anchorage, USA, June/July 2013 (Peer reviewed)

Mirjam Fürth is a 2013 recipient of ISOPE Scholarship for Outstanding Students

Proceedings of the Twenty-third (2013) International Offshore and Polar Engineering
Anchorage, Alaska, USA, June 30–July 5, 2013

ISBN 978-1-880653-99–9 (Set); ISSN 1098-6189 (Set)

www.isope.org

Determining Wave Resistance Using a Dissipative Potential Flow Model

Mirjam Fürth, Mingyi Tan and Zhi-Min Chen
Fluid-Structure Interaction Research Group, University of Southampton.
Southampton, Hampshire, United Kingdom

ABSTRACT

The wave resistance of a ship is determined using a dissipative potential flow model and a modified transverse cut techniques. The problem is modelled using Kelvin sources with a translating speed. Rayleigh damping is introduced in the model to represent a damping effect. A dissipative 3D Green function is derived where the Laplace equation, free surface condition and the radiation condition are transformed using a Fourier transform to get the Havelock-Lunde formula of the double integral. Thin ship theory is adopted to determine the wave pattern behind a Wigley hull. To evaluate the method and determine the wave resistance and a new and modified form of the Eggers transverse cut technique is used.

KEY WORDS: Wave resistance; dissipative potential flow; Green function; Rayleigh damping; Egger series; transverse cut.

INTRODUCTION

In shipping; a significant cost both to the ship owners and the environment is the fossil fuels used for propulsion. A tenth of the world consumption of oil is used to power the merchant fleet (Nilsson, 2010). To propel ships, heavy oil is used which, during its manufacturing stages produces as much as three times in total CO_2 emissions compared to conventional oil (Century, 2008). With the rising price of oil and the growing environmental concern, the motivation to reduce oil consumption has never been higher.

In the design phase, in order to determine the propulsion cost it is necessary to estimate the resistance of the ship. To simplify the resistance calculation of a ship, the resistance is traditionally divided into friction resistance and wave resistance; it is commonly assumed that they can be determined independently.

Potential flow is a common method to determine wave resistance of ships. In its conventional form the flow is assumed to be free from damping. Stokes (1851) first suggested to include some viscosity in potential flow to better model dissipation of energy. Havelock (1935) deemed it "fairly certain" that the difference between theoretical and experimental results depends on the neglect of friction in ship waves. When looking at waves due to a moving ship, it is evident that damping has an important physical role and by including more of the actual physical aspect in mathematical model the results will improve. Initial 2D investigations show encouraging results for dissipative potential flow (Fürth, 2011).

The main benefit of potential flow compared to other methods to determine the wave resistance such as Reynolds-Averaged Navier-Stokes (RANS) and Large-Eddy Simulation (LES) based solvers is the speed. Early on in the process simplicity and fastness comes before accuracy, to some degree (Noblesse et al, 2010).

A RANS (or LES) based CFD software is currently too time-consuming to be adopted in the initial design stages. However if the early wave resistance predictions are too inaccurate the design phase becomes longer and therefore more expensive. The cost will also increase if the prediction method used early on is slow. Therefore, a method which is more accurate, but still as fast as existing potential flow methods or experimentally derived wave resistance methods, could improve the design process.

To address this; this paper aims to develop an efficient numerical method for wave resistance prediction based on an improved potential theory which incorporates certain viscous effect in the model. The underlining methodology will be based on a potential flow model and a new Green function for the modified governing equations will be derived.

MATHEMATICAL MODEL

To model the problem a right-handed Cartesian coordinate system *Oxyz* is used. It moves steadily with the ship in the direction of *Ox*. Here *Oxy* is the undisturbed surface, *Ozx* the centre plane and *Oyz* the midship section of the ship. And *Oz* is defined as upwards, against the gravitational acceleration. The ship moves through horizontally and vertically unbounded water. The problem is modelled using Kelvin sources with a translating speed, which eliminates the need to place sources on the surface.

Appendix A

It is in the Navier-Stokes equations that a viscous a Rayleigh damping force can be introduced. It is assumed that the damping depends on the velocity and a constant μ_R , which is similar to the added viscosity by Havelock (1932). The damping does not affect the uniform speed. This gives the non-dimensionlized steady state Bernoulli equation

$$\frac{1}{2}|\nabla\Phi|^2 + {}^{1}\!/_{Fn^2}\, z + \mu_R(\Phi - x) = \frac{1}{2} \tag{1}$$

Where Fn^2 is the Froude number, μ_R the Rayleigh damping and the total potential Φ is

$$\Phi = -x + \phi \tag{2}$$

Here ρ^* is the density of water, L^* the length of the ship and U^* the speed. Non-dimensional variables are defined in terms of $\rho^* L^{3^*}$ for mass, L^* for length and L^*/U^* for time and are seen in Table 1.

Table 1 Definition of non-dimensional flow variables

Variable	Dimensional	Non-dimensional
Density of water	ρ^*	$1 = \rho^*/\rho^*$
Length of ship	L^*	$1 = L^*/L^*$
Free stream velocity	U^*	$1 = U^*/U^*$
Acceleration of gravity	g^*	$g^* L^*/U^{2^*} = 1/F_n^2$
Coordinates	x^*, y^*, z^*	x, y, z= $(x^*, y^*, z^*)/L^*$
Speed of ship	$q^* = (u^*, v^*, w^*)$	q=(u ,v ,w) = q^*/U^*
Rayleigh damping parameter	μ_R^*	$\mu_R = \mu_R{}^* L^*/U^*$
Pressure	p^*	$p = p^*/\rho V^2$
Time	t^*	$t = t^* U^*/L^*$

The dynamic free surface condition is

$$\eta = F_n^2\left(\frac{\partial\phi}{\partial x} - \mu_R\phi\right) \tag{3}$$

Where η is the free surface. The steady state free surface which is consistent with the expression by Havelock (1928, 1932) is

$$\left[\frac{\partial^2}{\partial x^2} - \mu_R\frac{\partial}{\partial x} + {}^{1}\!/_{F_n^2}\frac{\partial}{\partial z}\right]\phi = 0 \tag{4}$$

The Green function that is bounded by the free surface is defined by the Laplace equation, the free surface condition and the radiation condition. This problem can be solved using a double Fourier transform according to Noblesse (1981). By transforming the fundamental solution the PDE in the Laplace equation will reduce to an ODE. A double Fourier transform with respect to x and y is used leaving z untransformed. The solution to the ODE is then transformed back to get the Havelock-Lunde formula of the double integral (Havelock, 1932, Lunde, 1951). The Green function in polar coordinates is:

$$\begin{aligned} &4\pi G(\boldsymbol{x}', \mu_R, F_n) \\ &= -\frac{1}{r} + \frac{1}{r'} \\ &+ \frac{2}{\pi} Re \int_{-\pi/2}^{\pi/2}\int_0^\infty \frac{e^{\rho[z' - i(x'cos\theta + |y\prime|sin\theta)]}}{\rho Fn^2 cos^2\theta - 1 - \mu_R i cos\theta Fn^2}\, d\rho d\theta \end{aligned} \tag{5}$$

Polar coordinates are more suitable to get the Havelock-Lunde formula with damping and it also has the benefit that at least one integration parameter is bounded; the angle θ does not go to infinity. Where

$$x' = x - a \quad y' = y - b \quad z' = z + c \quad r' = \sqrt{x'^2 + y'^2 + z'^2} \tag{6}$$

r' is then the distance from the field point to the image source, where the field point is $\boldsymbol{x} = (x,y,z)$ and the location of the singularity is $\boldsymbol{a} = (a,b,c)$ where c is strictly negative. The double integral in the Green function above has a major benefit compared to conventional methods. The location of the pole is off the real axis because of the damping as seen in Figure 1. This enables a straight forward integration along the real axis.

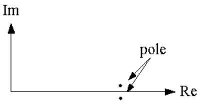

Figure 1 The pole can be placed at either side of the real axis depending on θ

Application with Thin Ship Approximation

Michell (1898) developed thin ship theory to determine the resistance of ships. The theory is powerful since properties such as the wave profile along the hull, pressure on the hull, hydrodynamic lift and pitch moment, sinkage, trim, drag and the wave pattern can be determined with only sources on the centre plane meaning that a 3D problem partly becomes a 2D problem (Noblesse et al, 2009). The local source strength is proportional to the change of geometry in the x direction (Faltinsen, 2006). Michell's theory is exceptionally simple and robust when it comes to evaluating steady flow around a ship and the most widely used theory for determining wave resistance (Noblesse et al, 2009).

The centre plane is divided into panels and it is assumed that the Green function is relatively constant over each panel (the difference between the node point and control point for each panel is very small) so that

$$\phi(\boldsymbol{a}) = G \iint\limits_{panel} Q dx dz \tag{7}$$

Using the principals of Faltinsen (2006) Equation (7) can be written as

$$\phi(\boldsymbol{a}) = GQ \tag{8}$$

Where Q is defined as

$$Q = 2\int_{x_0}^{x_1} dx \int_{z_1}^{z_0} \frac{\partial y_m}{\partial x} dz \tag{9}$$

Where x_0 is the forward edge of each panel, x_1 the aft edge, z_0 the edge closest to the surface and z_1 the deepest edge.

Wigley hull

A Wigley hull is mathematically defined as

$$y_m = \frac{B}{2}\left(1 - \left(\frac{z}{D}\right)^2\right)\left(1 - \left(\frac{x}{0.5L}\right)^2\right) \tag{10}$$

Where y_m is the location of the model in y direction, B the width of the ship, D the draft and L the length. The particulars for the Wigley hull are shown in Table 2.

Table 2 Wigley hull

L	1
B	0.1
D	0.0625

Wave Resistance from Wave pattern

The concept of determining the wave resistance from the wave pattern, without reference to the ship, was originally proposed by Havelock (1934a, b). Eggers (1962) showed that using linear theory the pattern behind a ship can be expressed as a summation of series of discrete wave modes where each mode is described as a sinusoidal wave train with a particular amplitude, phase, wave number and direction. Eggers described how this function can be determined from wave elevation measurements, and from this subsequently get the corresponding resistance (Eggers, 1962, Hogben, 1972). There are three main approaches, either a transverse cut, a longitudinal cut or an "*X-Y*" method ("X-Y" method is a combination of a transverse and longitudinal cut method it also described as a longitudinal cut method with a truncation term) (Eggers et al, 1967). For numerical methods the transverse cut is superior partly due to the fact that the wave profile is finite (Nakos, 1991, Nakos & Sclavounos, 1994, Raven & Prins, 1998). The transverse cut also benefits from the limited extent of the discretisation that is needed downstream of the ship (Nakos & Sclavounos, 1994).

A minimum of two cuts is needed but it has been shown that a larger number of cuts are needed to reduce redundancy and increase accuracy (Janson & Spinney, 2004, Raven & Prins, 1998). The transverse cuts must be far enough aft of the ship, they must extend outside of the Kelvin wedge and the resolution must be high enough to show all components of interest (Raven & Prins, 1998).

A conventional form of the transverse cut technique will give a lower wave resistance estimation for higher Rayleigh damping since higher damping generates lower wave profiles. Where higher damping should imply higher resistance since the modelled water would be more viscous. So a modified and new form of the Eggers series transverse wave cut technique is developed. This method retains many aspects of the conventional transverse wave cut and still has its main benefit; the whole wave pattern does not need to be known, only the profile in the cuts. The cut technique presented here will take damping into account.

Momentum analysis of flow around a hull

The wave resistance can be determined using a control volume analysis around the hull as seen in

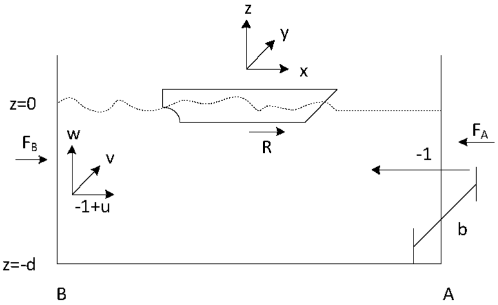

Figure 2 Control volume with ship

A control volume analysis of the momentum inflow and outflow and pressures on the side *A* and *B* of the volume in Figure 2 gives the wave resistance

$$R = \frac{1}{2Fn^2} \int_{-b/2}^{b/2} \eta_B^2 \, dy + \frac{1}{2} \int_{-b/2}^{b/2} \int_{-d}^{\eta_B} [-u^2 + v^2 + w^2] + \mu_R \phi_B dzdy \tag{11}$$

The upper limit of the inner integral will be replaced from the free surface to assumed location of the free surface *z*=0. And it can be noted that after integration the last term $\mu_R \phi_B$ will disappear.

The potential of a freely moving wave

To determine the resistance the potential for a freely moving wave must be known. The potential must satisfy the Laplace equation, the combined free surface condition (which also means it must satisfy the kinematic and dynamic free surface condition) and the seabed condition. This gives the potential and wave profile for a freely moving wave with Rayleigh damping

$$\eta = \sum_{n=0}^{\infty} e^{\mu_R x} [\xi_n cos(k_n x cos\theta_n) - \varpi_n sin(k_n x cos\theta_n)] cos\left(\frac{2\pi n y}{b}\right) \tag{12}$$

$$\Phi = \sum_{n=0}^{\infty} \frac{1}{Fn^2 k_n cos\theta_n} e^{\mu_R x + k_n z} [\varpi_n cos(k_n x cos\theta_n - \mu_R z) + \xi_n sin(k_n x cos\theta_n - \mu_R z)] cos\left(\frac{2\pi n y}{b}\right) \tag{13}$$

Where ϖ_n and ξ_n are the unknown wave parameters. And θ_n the angle of each wave is defined according to Figure 3 (not to be confused with the integration angle θ).

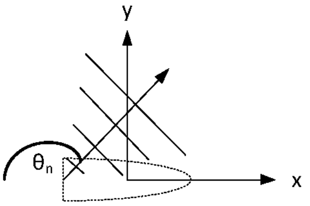

Figure 3 Moving ship with wave pattern

If the potential in equation (13) is used, the resistance will depend on the location of the downstream end of the control volume (B) in Figure 2, this is not reasonable. But if the cut B is taken close to the ship the term $e^{\mu_R x_B}$ will be so small that it can be assumed to be negligible. However the term $\mu_R z$ inside in the argument also gives a resistance that depends on the location of the end of the control volume *B*. It can be argued that the term $\mu_R z$ only gives the phase of the potential and should not affect the wave height so the following simplified potential is used. This gives the simplified potential and wave profile for a freely moving wave

$$\eta = \sum_{n=0}^{\infty} [\xi_n cos(k_n x cos\theta_n) - \varpi_n sin(k_n x cos\theta_n)] cos\left(\frac{2\pi n y}{b}\right) \tag{14}$$

$$\Phi = \sum_{n=0}^{\infty} \frac{e^{k_n z}}{Fn^2 k_n cos\theta_n} [\varpi_n cos(k_n x cos\theta_n) + \xi_n sin(k_n x cos\theta_n)] cos(k_n y sin\theta_n) \tag{15}$$

This gives the wave resistance

$$R = \frac{b}{4Fn^2}(\varpi_0^2 + \xi_0^2) + \sum_{n=1}^{\infty} \frac{b}{4Fn^2}\left[(\varpi_n^2 + \xi_n^2)\left(1 - \frac{1}{2}cos^2\theta_n\right)\right] \tag{16}$$

where the wave angle θ can be determined using

$$k_n sin\theta_n = \frac{2\pi n}{b} \tag{17}$$

where the wave number k_n is

$$k_n^2 = \frac{k_n}{Fn^2} + \left(\frac{2\pi n}{b}\right)^2 \tag{18}$$

To determine the resistance in (16) the wave parameters ϖ_n and ξ_n must be known. To determine them at least two downstream cuts (wave profiles) are needed. Since these cuts can be located far downstream the term $e^{\mu_R x}$ cannot be assumed to be small so the wave profile in (12) must be used. It can be written as

$$\eta = \sum_{n=0}^{\infty} C_n cos\left(\frac{2\pi n y}{b}\right) \tag{19}$$

So that for cut j

$$C_{nj} = [\xi_n cos(x_j k_n cos\theta_n) - \varpi_n sin(x_j k_n cos\theta_n)] e^{\mu_R x_j} \tag{20}$$

C_{nj} can be obtained by matching a Fourier series to the wave profile. From C_{nj} can the wave parameters ξ_n and ϖ_n be determined. This finally gives the resistance in (16). The novelty for this method is last term $e^{\mu_R x_j}$ in (20) which compensates for the damping when determining the wave resistance.

NUMERICAL INVESTIGATIONS

As stated before; two cuts is the minimum but a higher number of cuts are needed to increase accuracy. Janson and Spinney (2004) uses 10 cuts, Raven and Prins (1998) 8 cuts and Sharma (1963, 1966) concludes that at least 5 cuts is need to get the error within 5 %. Janson and Spinney (2004) also mentions that "certain numerical problems" can be avoided by using non-equidistant spacing between the cuts.

Based on this 10 cuts are used with a non-equidistant spacing. Janson and Spinney got their best results by increasing the space between each cut with a multiplication factor f_m. the same spacing and multiplication factor is used here and shown in Table 3 and Figure 4.

Table 3 Cut spacing properties

Initial separation	Multiplication factor
$dx = 0.3$	$f_m = 1.1$

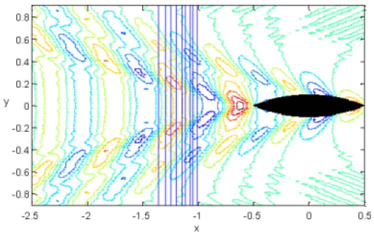

Figure 4 Location of the ten cuts

The whole wave pattern must be included in transverse direction. The Kelvin angle that incorporates the whole wave pattern is seen in Figure 5.

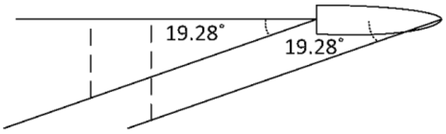

Figure 5 Kelvin angle for bow and stern wave

Based on this the grid spacing in Table 4 is used.

Table 4 Field point spacing

x field spacing	*y* field spacing	Max *x* field point	Spacing field points
$nx = 120$	$ny = 60$	$xmax = 3$	$dx = dy = xmax/(nx\text{-}1)$

The wave pattern behind the ship is determined by inserting the potential (8) in the dynamic free surface condition (3). The Green function G is given by (5) and the source strength Q by (9). A one point Gauss quadrature rule is used to integrate the double integral in equation (5)

$$\int_{-\frac{\pi}{2}}^{\frac{\pi}{2}} \int_0^{\infty} \frac{e^{\rho[z' - i(x' cos\theta + |y'| sin\theta)]}}{\rho Fn^2 cos^2\theta - 1 - \mu_R i cos\theta Fn^2} d\rho d\theta = dr \cdot dt \sum_{\theta=-\pi/2}^{\pi/2} \sum_{\rho=0}^{M} \frac{e^{\rho[z' - i(x' cos\theta + |y'| sin\theta)]}}{\rho Fn^2 cos^2\theta - 1 - \mu_R i cos\theta Fn^2} \tag{21}$$

where

$$dr = M/(nr - 1) \tag{22}$$

$$dt = \pi/(nt - 1) \tag{23}$$

Where M is the upper limit of the integral replacing ∞ and *dr*, *dt*, *nr* and *nt* are defined in Figure 6.

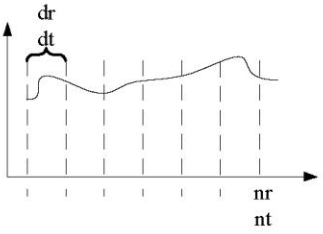

Figure 6 Explanation of integration parameters *dr*, *dt*, *nr* and *nt*

θ and ρ are increased with *dt* and *dr* respectively. The step length parameters *nt* and *nr* are varied and *Cw* determined when the first cut is placed at x=-1 (0.5*L* aft of the stern).

It is seen from (5) that the term $\rho z'$ makes the integral decrease when ρ is increasing, the rest of the exponent only makes the function oscillate. So when $\rho z'$ is sufficiently small the double integral will be close to zero. Therefore *M* is set to be a function of the location of the source. Using one row of sources in the z direction (number of sources in z direction, *nsz* = 1), means that $z'=D/2= -0.0313$. *M* is chosen so that $Mz'=-6$ which means that the double integral is small according to

$$e^{Mz\prime} = e^{-6} = 2.478 \cdot 10^{-3} \tag{24}$$

When investigating the suitable parameters for the double integral and the sources, Rayleigh damping $\mu_R = 0.1$ and Froude number $Fn = 0.3$ are used.

So with a constant upper limit, *nr* will only change the step length in the summation in (21). The number of sources is here 20 in *x* direction (*nsx* =20). It is seen from Table 5 that *Cw* depends on the discretisation of the double integral, however after *nt* = 1500 this dependence is small. The wave profile for the different values of *nt, nr* in Table 5 are shown in Figure 7. It can be seen that the profile is affected and the borders are showing some noise when the step length is increased. However as seen from Table 5 it does not affect the final result other than beyond the fourth significant number.

Table 5 Values of Cw for varying step length in the double integral

nr	nt	Cw
375	75	0.0028175
750	150	0.0025553
1500	300	0.0026440
3000	600	0.0026417
6000	1200	0.0026417
12000	2400	0.0026417

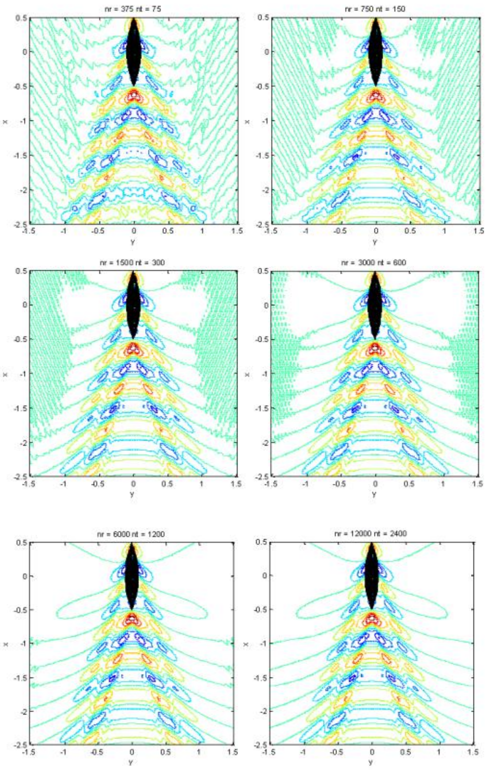

Figure 7 Wave pattern behind Wigley hull for varying *nt* and *nr*

The importance of *M* as the upper limit of the inner integral is determined using the same step length. The results are shown in Figure 8 and Table 6.

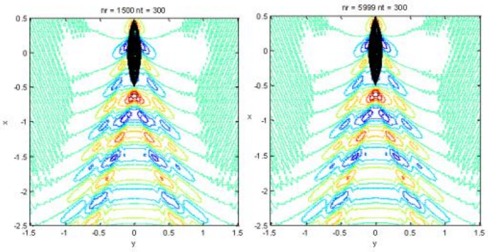

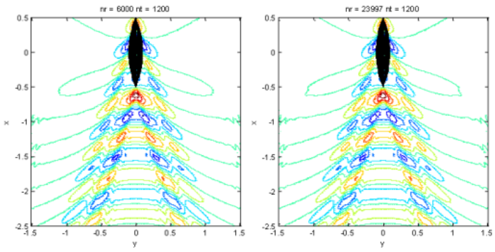

Figure 8 Wave pattern for different upper limit *M* according to Table 7

Table 6 Particulars for Figure 8

Figure 8	Mz'	nr	dr	nt	Cw
Top left	-6	1500	0.1278807	300	0.0026440
Top right	-24	5999	0.1278807	300	0.0026448
Bottom left	-6	6000	0.0320053	1200	0.0026417
Bottom right	-24	23997	0.0320053	1200	0.0026418

Judging from Figure 8 and Table 6 it is assumed that using *nr* = 1500, *nt* =300 and *Mz'* = -6 will give a result which is accurate enough.

Number of Sources

The centre plane is divided into panels in *x* and *z* direction giving each panel one source. The sources are evenly spaced. Table 7 shows the wave resistance coefficient, *Cw* and the number of sources in *x* direction. One row of sources in *z* direction is used.

Table 7 Values of Cw for different number of sources in *x* direction

Number of sources in x direction, *nsx*	Cw
10	0.0029407
20	0.0026440
40	0.0025775
80	0.0025613
160	0.0025573

From Table 7 it is seen that 40 sources in *x* direction is sufficient compared to the prolonged computational time with comes with an increase in the number of sources. The wave pattern for 1 to 3 rows of sources in *z* direction and 40 sources in *x* direction are showed in Figure 9.

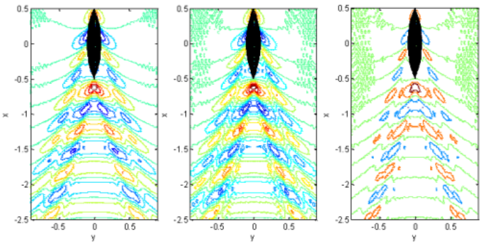

Figure 9 Wave pattern nsx =40, nsz = 1, nsxz =2, nsz = 3 repectivly (left to rigth)

In Figure 9 it is clearly seen that the wave pattern distorts when the number of sources are 3 in z direction, this is also evident for higher number of rows but not shown here. This could be because the top sources come to close to the surface and the double integral does not go towards zero fast enough (as stated before the decay depends on the source location), where *M* is varied so that *Mz'* is constant (*Mz'* = -6), so that *M* is larger when *z'* is closer to the surface. From

Table 8 it is also evident that this method is not suitable for *nsz*>1 since it will give too high wave resistance.

Table 8 Cw for different *nsz*, *nsx* = 40

nsz	Cw
1	0.0025775
2	0.0033247
3	0.0035643

Wave resistance coefficient

The following results were obtained using the parameters in Table 9.

Table 9 Result properties

Number of field points *x* direction	*nx*	120
Number of field points *y* direction	*ny*	60
Location of furthest downstream field point	*xmax*	3
Summation variable θ	*nt*	300
Summation variable ρ	*nr*	1500
Upper limit inner integral	*Mz'*	-6
Number of sources *x* direction	*nsx*	40
Number of sources *y* direction	*nsz*	1

Cw is shown as a function of Froude number in Figure 10 to Figure 13 for different values of μ_R. The reference values are both experimental and numerical. Tarafder and Suzuki (2008) and Bal (2008) uses a Rankine source panel methods with a linearized free surface in their numerical model. Chen and Noblesse (1983) uses slender ship theory and Kelvin sources. Nakatake et al. (1979) uses double body flow and a low speed assumption. None of the numerical methods include any damping.

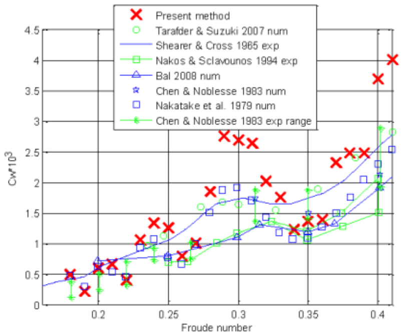

Figure 10 *Cw* as a function of *Fn* with μ_R=0.01

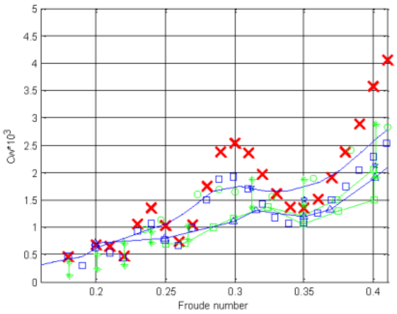

Figure 11 *Cw* as a function of *Fn* with μ_R=0.05

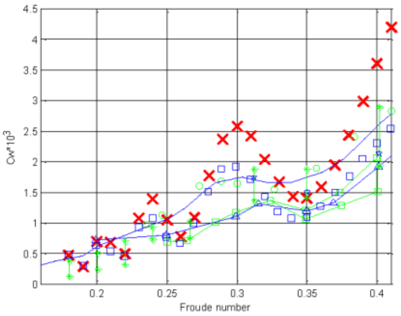

Figure 12 *Cw* as a function of *Fn* with μ_R=0.1

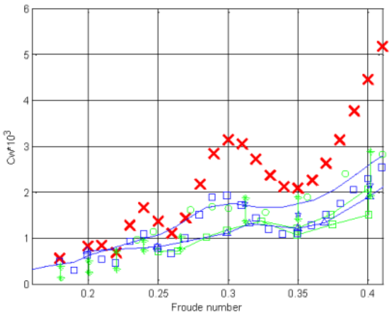

Figure 13 *Cw* as a function of *Fn* with μ_R=0.5

Location of the cuts

The wave resistance will depend on the location of the cut for any method that includes damping, numerical damping is enough to make the resistance change with the location of the cuts (Nakos, 1991). Even traditional potential flow methods have this problem. *Cw* as a function of the location of the cuts is seen in Figure 14 to Figure 17. The Wigley hull is located between 0.5*L* and -0.5*L*, which means that the first location of the cut that will not interfere with the near field stern wave is -*L*. Here 10 cuts are used.

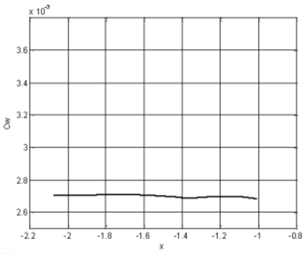

Figure 14 *Cw* as a function of the location of the first cut, *Fn* =0.3 and μ_R=0.01

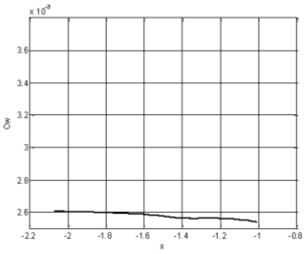

Figure 15 *Cw* as a function of the location of the first cut, *Fn* =0.3 and μ_R=0.05

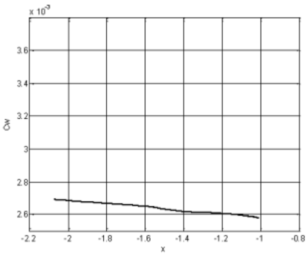

Figure 16 *Cw* as a function of the location of the first cut, *Fn* =0.3 and μ_R=0.1

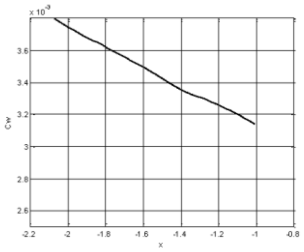

Figure 17 *Cw* as a function of the location of the first cut, *Fn* =0.3 and μ_R=0.5

CONCLUSIONS

Rayleigh damping is introduced into a potential flow model in order to more accurate by model the decay due to friction that waves have over time and distance. A new Green function for potential flow including damping is developed. This function also has a major mathematical benefit since it has no singularity in the double integral which is present in conventional Green functions that does not include damping. This method is evaluated using a modified version of the transverse cut technique (based on the Egger series wave theory) to determine the resistance for a Wigley hull.

The wave resistance coefficient (*Cw*) is compared to numerical and experimental reference values. The profile of *Cw* as a function of Froude number shows the same humps and hollows as the conventional results. However *Cw* for the present method is higher and it is increased with higher damping. It is expected since higher damping would imply more viscous water which would give a higher resistance. The results shows a large deviance form the reference values at *Fn*>0.4 this could imply that the present model has limitations at larger Froude numbers.

The dependence for *Cw* on the location of the cut for $\mu_R \leq 0.1$ is less than the dependence in the method by Janson and Spinney (2004) who's method does not include damping (other than numerical). However, for larger values of μ_R the wave resistance coefficient will depend on the location of the transverse cut, this implies a limitation to the application of the transverse cut technique to a dissipative wave pattern. For better accuracy a panel method would be recommended for flows with high dissipation.

ACKNOWLEDGEMENTS

This project is sponsored by Lloyds Register Educational Trust, their support is greatly appreciated.

REFERENCES

Bal, S. (2008) Prediction of Wave Pattern and Wave Resistance of Surface Piercing Bodies by a Boundary Element Method. *International Journal for numerical methods in fluids,* Vol 56, pp. 305-329.

Century, J.R. (2008) Tar Sands: Key Geologic Risks and Opportunities. *Leading Edge*, pp. 1202-1204.

Chen, C.Y.,Noblesse, F. (1983) Preliminary Numerical Study of a New Slender-Ship Theory of Wave Resistance. *Journal of Ship Research,* Vol 27, pp. 172-186.

Eggers, K. (1962) Über Die Ermittlung Des Wellenwiderstandes Eines Schiffsmodells Durch Analyse Seines Wellensystems. *Schiffstechnick Bd,* Vol 9.

Eggers, K., Sharma, S. & Ward, L. (1967) An Assessment of Some Experimental Methods for Determining the Wavemaking Characteristics of a Ship Form. *Transactions of the institution of naval architects and marine engineers,* Vol 75, pp. 112-144.

Faltinsen, O.M. (2006) *Hydrodynamics of High-Speed Marine Vehicles,* Cambridge, Cambridge University Press.

Fürth, M. (2011). *Determining the Pressure Distubution on Submerged 2d Bodies Using Dissipative Potential Flow.* Master thesis, KTH.

Havelock, T.H. (1928) Wave Resistance. *Proceedings of the Royal Society of London. Series A,* Vol 118, pp. 24-33.

Havelock, T.H. (1932) The Theory of Wave Reistance. *Proceedings of the Royal Society of London Series a-Mathematical and Physical Sciences,* Vol 138, pp. 339-348.

Havelock, T.H. (1934a) The Calculation of Wave Resistance. *Proceedings of the Royal Society of London. Series A, Containing Papers of a Mathematical and Physical Character,* Vol 144, pp. 514-521.

Havelock, T.H. (1934b) Wave Patterns and Wave Resitance. *Transactions of the instituion of naval architects,* Vol 74, pp. 340.

Havelock, T.H. (1935) Ship Waves: The Relative Efficiency of Bow and Stern. *Proceedings of the Royal Society of London. Series A, Mathematical and Physical Sciences,* Vol 149, pp. 417-426.

Hogben, N. (1972) Automated Recording and Analysis of Wave Patterns Behind Towed Models. *Transactions of the royal institutions of naval architects,* Vol 114, pp. 127-153.

Janson, C.-E.,Spinney, D. (2004) A Comparison of Four Wave Cut Analysis Methods for Wave Resistance Prediction. *Ship Technology Research,* Vol 51, pp. 173-184.

Lunde, J.K. (1951) *On the Linearized Theory of Wave Resistance for Displacement Ships in Steady and Accelerated Motion,* The Society of Naval Architects ans Marine Engineers.

Michell, J.H. (1898) The Wave-Resistance of a Ship. *Philosophical Magazine,* Vol 45, pp. 106-123.

Nakatake, K., Toshima, A. & Yamazaki, R. (1979) Wave-Resitance Calculation for Wigley, S-201 and Series 60 Hulls. *In:* Workshop onship Wave-Resitance Camputations, 1979 David W. Taylor Naval Ship Research and Development Center, Bethesda Md., 215-231.

Nakos, D.E. (1991) Transverse Wave Cut Analysis by a Rankine Panel Method. *In:* 6th WWWFB, 1991.

Nakos, D.E.,Sclavounos, P.D. (1994) Kelvin Wakes and Wave Resistance of Cruiser-and Transom-Stern Ships. *Journal of Ship Research,* Vol 38, pp. 9-29.

Nilsson, R.P. (ed.) (2010) *Sjöfartens Bok,* Gothenburg: Svensk Sjöfarts Tidings Förlag AB.

Noblesse, F. (1981) Alternative Integral-Representations for the Green-Function of the Theory of Ship Wave Resistance. *Journal of Engineering Mathematics,* Vol 15, pp. 241-265.

Noblesse, F., et al. (2010) Practical Mathematical Representation of the Flow Due to a Distribution of Sources on a Steadily Advancing Ship Hull. *Journal of Engineering Mathematics*, pp. 1-26.

Noblesse, F., et al. (2009) Thin-Ship Theory and Influence of Rake and Flare. *Journal of Engineering Mathematics,* Vol 64, pp. 49-80.

Raven, H.C.,Prins, H.J. (1998) Wave Pattern Analysis Applied to Nonlinear Ship Wave Calculations. *13th International Workshop on Water Waves and Floating Bodies.* Maritime Research Institute Netherlands.

Sharma, S.D. (1963) A Comparison of the Calculated and Measured Free-Wave Spectrum of an Inuid in Steady Motion. *In,* 1963.

Sharma, S.D. (1966) An Attempted Application of Wave Analysis Techniques to Achieve Bow-Wave Reduction. *In:* Sixth ONR Symposium on Naval Hydrodynamics, 1966. 731-773.

Stokes, G.G. (1851) On the Effect of the Internal Friction of Fluids on the Motion of Pendulums. *Transactions of the Cambridge Philosophical Society,* Vol 9, pp. 8.

Tarafder, S.,Suzuki, K. (2008) Numerical Calculation of Free-Surface Potential Flow around a Ship Using the Modified Rankine Source Panel Method. *Ocean Engineering,* Vol 35, pp. 536-544.